

**Photon-counting single-molecule spectroscopy for studying
conformational dynamics and macromolecular interactions**

by

Ted Alfred Laurence

B.S. (California Institute of Technology) 1997

A dissertation submitted in partial satisfaction of the

requirements for the degree of

Doctor of Philosophy
in

Physics

in the

GRADUATE DIVISION

of the

UNIVERSITY OF CALIFORNIA, BERKELEY

Committee in charge:

Professor Daniel S. Chemla, Chair

Professor Yuen Ron Shen

Professor Ehud Y. Isacoff

Fall 2002

The dissertation of Ted Alfred Laurence is approved:

Chair

Date

Date

Date

University of California, Berkeley

Fall 2002

Abstract

Photon-counting single-molecule spectroscopy for studying
conformational dynamics and macromolecular interactions

by

Ted Alfred Laurence

Doctor of Philosophy in Physics

University of California, Berkeley

Professor Daniel S. Chemla, Chair

Abstract

Single-molecule methods have the potential to provide information about conformational dynamics and molecular interactions that cannot be obtained by other methods. Removal of ensemble averaging provides several benefits, including the ability to detect heterogeneous populations and the ability to observe asynchronous reactions.

Single-molecule diffusion methodologies using fluorescence resonance energy transfer (FRET) are developed to monitor conformational dynamics while minimizing perturbations introduced by interactions between molecules and surfaces. These methods are used to perform studies of the folding of Chymotrypsin Inhibitor 2, a small, single-domain protein, and of single-stranded DNA (ssDNA) homopolymers. Confocal microscopy is used in combination with sensitive detectors to detect bursts of photons from fluorescently labeled biomolecules as they diffuse through the focal volume. These bursts are analyzed to extract fluorescence resonance energy transfer (FRET) efficiency. Advances in data acquisition and analysis techniques that are providing a more complete picture of the accessible molecular information are discussed.

Photon Arrival-time Interval Distribution (PAID) analysis is a new method for monitoring macromolecular interactions by fluorescence detection with simultaneous determination of coincidence, brightness, diffusion time, and occupancy (proportional to concentration) of fluorescently-labeled molecules undergoing diffusion in a confocal detection volume. This method is based on recording the time of arrival of all detected photons, and then plotting the two-dimensional histogram of photon pairs, where one axis is the time interval between each pair of photons 1 and 2, and the second axis is the number of other photons detected in the time interval between photons 1 and 2. PAID is

related to Fluorescence Correlation Spectroscopy (FCS) by a collapse of this histogram onto the time interval axis. PAID extends auto- and cross-correlation FCS by measuring the brightness of fluorescent species. A data-fitting model is developed, which is used to simultaneously determine coincidence, brightness, diffusion time, and occupancy from experiments performed on fluorophore-labeled dsDNA test samples. Using simulations, the performance of PAID is compared with existing methods. The statistical accuracy of the parameters extracted using PAID exceeds or matches the accuracy of the other methods, while providing additional information.

Acknowledgments

I am extremely grateful to all those who helped me during my dissertation work. Shimon Weiss, my research supervisor, has guided and encouraged me continually throughout these five years. He has helped me capture the vision of what single-molecule methods can do for biology. Daniel Chemla, my advisor, encouraged me to enter the single-molecule biophysics group, and provided an excellent research environment. Ashok Deniz is a great colleague with whom I always perform useful work and have productive discussion. He initiated our efforts in protein folding, synthesizing the protein and performing the ratiometric single-pair Fluorescence Resonance Energy Transfer (spFRET) experiments. Achillefs Kapanidis gave me insight into ways Photon Arrival-time Interval Distribution (PAID) analysis could be useful for molecular interactions. He prepared the dsDNA fragments used in section 3 of the dissertation, and performed several of the experiments. I thank those colleagues with whom I have had many useful discussions about the writing of this dissertation: Xavier Michalet, Sören Doose, Emmanuel Margeat, Ashok Deniz, and Achillefs Kapanidis. I thank the members of my qualifying exam and dissertation committees, Professors Daniel Chemla, Y. Ron Shen, Ehud Isacoff, and Daniel Rokhsar. I also thank those who helped train me when I first entered the group: Taekjip Ha, Jennifer Glass, Thilo Lacoste, and Maxime Dahan. I especially thank my wife, Jennifer, for her encouragement and understanding during my graduate studies.

Table of Contents

Acknowledgments.....	i
Table of Contents.....	iii
1. Introduction.....	1
2. Single-molecule spectroscopy for conformational dynamics.....	6
2.1. Single-molecule observables for conformational dynamics.....	6
2.1.1. Fluorescence Resonance Energy Transfer.....	7
2.1.2. Polarization anisotropy.....	11
2.2. Data acquisition.....	15
2.3. Single-molecule data analysis for diffusing species.....	18
2.3.1. Single-molecule ratiometric data analysis for diffusing species.....	19
2.3.2. Moments of peaks in the measured histograms.....	22
2.3.3. Burst and fluctuation analysis methods.....	25
2.3.4. Time-correlated single-photon counting.....	27
2.4. Protein folding of Chymotrypsin Inhibitor 2 (CI2).....	31
2.4.1. Materials and methods for CI2.....	33
2.4.2. Results and discussion using ratiometric analysis only.....	35
2.4.2.1. Protein system.....	35
2.4.2.2. Subpopulations of Pseudo wild-type and mutant CI2.....	37
2.4.2.3. Inter-dye distances for the native and denatured states.....	40
2.4.2.4. Shifts in average FRET efficiency of the denatured state.....	42
2.4.2.5. Distance distributions, widths, and potential functions.....	45
2.4.2.6. Denaturation curves extracted from FRET distributions.....	47
2.4.2.7. Conclusions – single-molecule ratiometric studies of CI2.....	49
2.4.3. Current work - CI2 using lifetime, Burst and fluctuation analysis methods.....	50
2.4.3.1. Development of single-molecule methods for observation of fast events in protein folding.....	52
2.5. Single-stranded DNA as a polymer.....	57
2.A. Simulation of rotational diffusion.....	61
3. Monitoring macromolecular interactions using Photon Arrival-time Interval Distribution (PAID) analysis.....	64
3.1. Introduction.....	64
3.1.1. Historical overview.....	64
3.1.2. Single-channel data reduction and analysis.....	67
3.1.3. Multiple-channel data reduction and analysis.....	70
3.2. Theory.....	75
3.2.1. Development and description of PAID.....	75
3.2.2. Application of PAID to fluorescent species diffusing in solution.....	84
3.2.3. Application of PAID to the determination of stoichiometry.....	91
3.2.4. Application of PAID to binding.....	92
3.2.5. Model for PAID.....	98
3.3. Materials and methods.....	101

3.3.1.	Simulation of translational diffusion of molecules, and photon emission and detection	101
3.3.2.	Fitting routine.....	103
3.3.3.	Preparation of dsDNA.....	103
3.3.4.	Experimental setup.....	104
3.4.	Results.....	105
3.4.1.	Simulations – extracting stoichiometry in a single channel.....	105
3.4.2.	Simulations – monitoring binding with two channels	112
3.4.3.	One-channel experiments.....	115
3.4.4.	Two-channel experiments.....	117
3.5.	Conclusion	129
3.A.	Bin specification and normalization for PAID histogram	131
3.B.	Algorithms for constructing PAID histograms	134
3.C.	Development of model for PAID.....	137
3.C.1.	Spatial distribution of molecules upon detection of start photon	140
3.C.2.	Calculation of the cross-correlation.....	141
3.C.3.	Photon count probability distribution for a single path of a single molecule	144
3.C.4.	Photon count probability distribution for all paths of a single molecule	147
3.C.5.	Photon count probability distribution for all molecules in solution	149
3.C.6.	Photon count distribution of stop channel intensity for a single molecule in solution	151
3.C.7.	PAID function for all molecules in solution.....	153
3.D.	Implementation of the model.....	157
3.D.1.	Evaluation of kernels for model.....	157
3.D.2.	Implementation of the model and fitting routine	159
3.E.	Combination of sources for probability distribution.....	164
3.F.	Equivalence of convolutions in \mathbf{n} -space and Λ -space	165
3.G.	Combination of sources for the monitor photon count distribution of stop channel intensity	167
3.H.	Efficient calculation of convolutions in a quasi-logarithmic scale.....	171

1. Introduction

Although we most often think about and model molecular systems in terms of individuals, experimental science has been dominated by measurements that result in ensemble averages. This has traditionally hidden much of the rich variety present at microscopic and mesoscopic scales. However, over the last decade, single-molecule methods have rapidly become an important tool in the repertoire of the experimentalist, with implications in a host of scientific disciplines.[1-7] Single-molecule measurements are especially useful for the study of complex systems, which are ubiquitous in biology. For systems involving static or dynamic heterogeneity, single molecule methods provide the unique ability to directly probe distributions of static properties and dynamics of interconversion between different states of the system, without the need to synchronize or trigger the interconversion. This ability is crucial in many biological contexts, where triggering is not possible, or where ensembles of molecules moving stochastically on complex reaction landscapes quickly lose their coherence, resulting in averaged behavior. Examples range from enzyme reactions with proposed multiple conformational substates, [8, 9] and protein folding with multiple unfolded states, pathways, intermediates and transition regions, [10-14] to interactions between cell-surface receptors or more downstream components of signal transduction pathways[15, 16]. Other examples include interactions between proteins, DNA and RNA during cellular functions such as recombination, transcription and translation, and aggregation processes that lead to diseases such as Alzheimer's and Creutzfeldt-Jakob diseases [17-20]. Single molecule methods also permit the observation of processes at extremely low molecular

concentrations; for example, conformational properties of individual prion proteins under aggregation conditions may be studied. A very intriguing application of single molecule detection is the simultaneous observation of transitions occurring in different parts of a system, allowing the direct evaluation of synergistic effects during biopolymer structural transitions, assembly or enzyme catalysis. Finally, these methods may lead to significant technical advances in areas such as high-throughput screening and DNA sequencing [4, 21-23]. Applications in the field of biological single molecule fluorescence spectroscopy have been elaborated in several excellent reviews [2, 7, 24-26].

The sensitivity to detect single molecules is useful even in situations where more than one molecule is detected at a time. Fluorescence Correlation Spectroscopy (FCS) [21, 27-29], two-color cross-correlation spectroscopy [29-31], and related methods are sensitive to single molecules diffusing in and out of the detection volume. One- and two-channel FCS have been used to analyze, sort, and detect conformational states of a few or single molecules in the excitation volume. FCS and related methods are especially useful for detecting and characterizing macromolecular interactions (see section 3).

There are two basic requirements for detection of single molecules. The signal of a particular molecule must be discriminated from other sources. Background sources and contributions from other molecules must be minimized or eliminated. For room-temperature applications, this means that a detection volume needs to be defined such that only one molecule is present at a time (at cryogenic temperatures, use of the narrow zero-phonon absorption line has been used to select single molecules). The size of the detection volume is limited by the diffraction of light (at visible wavelengths, this limit is

a few hundred nanometers). The detection volume is most commonly defined by using confocal microscopy, where a tightly focused laser excitation and a detection pinhole define a detection volume on the order of a femtoliter. Another common method is total internal reflection microscopy in combination with a high-sensitivity CCD camera (not discussed here). After defining a suitable detection volume, the concentration of the fluorescent species is adjusted so that on average less than one molecule of that species is present at a time.

The detection of fluorescence from single molecules involves repeated cycling of the molecule between ground and singlet excited states, and detection of the series of emitted photons; non-radiative relaxation of the excited state results in a reduction of the maximum photon flux. The signal from the molecule itself must be large enough that the intrinsic noise in photon counting measurements is overcome. The fluorophores, fluorescence collection optics, and photon detectors are all critical in maximizing photon flux and detection efficiency, and thus the signal strength.

Site-specific labeling of biomolecules with appropriate dyes is a prerequisite for single-molecule experiments [2]. Fluorescently labeled single biomolecules can be detected in two configurations, either immobilized (in a matrix or by surface attachment), or freely diffusing in solution. These two detection formats provide different and complementary kinds of information.

With immobilized molecules, a particular molecule can be observed over an extended period of time, and a time-trace of its properties continuously recorded. This can result in the observation of its stochastic fluctuations under equilibrium or non-equilibrium conditions, and represents the most complete characterization of the

molecule. However, care must be taken to ensure minimal perturbation due to the immobilization process.

In the other format, when diffusing or flowing single molecules in a liquid traverse the laser excitation volume, fluorescence photon-bursts are generated. Such bursts can be analyzed for their duration, brightness, spectrum, and fluorescence lifetime, thereby providing molecular information on identity, size, diffusion coefficient, and concentration [4, 21]. These bursts are short (typically millisecond timescale) and provide little information on slower fluctuations. However, they can provide invaluable information about the distributions of molecular properties of interest undisturbed by surface effects, and changes in these distributions under non-equilibrium conditions. Since a large number of events (photon bursts) can be collected in a relatively short time, statistical analyses of these data are possible and histograms can be constructed. Most notably, sub-populations of molecules in heterogeneous ensembles can be identified [32-34], and the properties of these subpopulations individually interrogated. For example, two-color burst analysis [30], and multiple-lifetime [32] approaches for identification and separation were suggested and implemented.

This dissertation will focus on the development of single-molecule methods aimed at studying conformational dynamics of and interactions between freely diffusing fluorescent biological systems, minimally perturbed by surfaces. Single-molecule methods for studying conformational dynamics are developed in section 2. These methods are applied to the folding of Chymotrypsin Inhibitor 2 (CI2) and to the dynamics of single-stranded DNA (ssDNA). A new method for studying macromolecular interactions, Photon Arrival-time Interval Distribution (PAID) analysis, is developed in

section 3. This new method extends FCS and cross-correlation FCS by adding new photon counting dimensions, taking advantage of more of the information in the photon data streams.

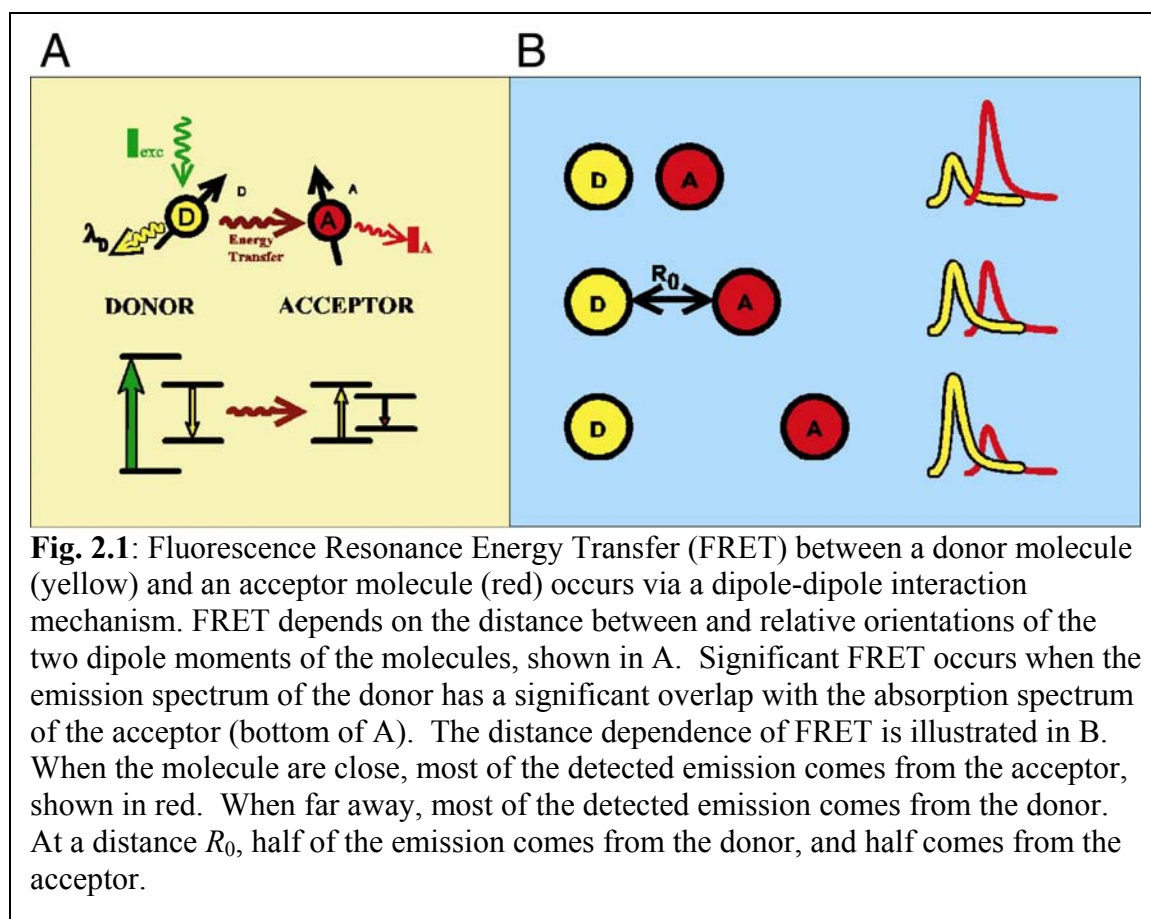
2. Single-molecule spectroscopy for conformational dynamics

Conformational dynamics of biological molecules often play an important role in their function. For example, motor proteins use chemical energy to drive conformational transitions that perform mechanical work. F1F0 Atp synthase uses a proton gradient across the mitochondrial membrane to synthesize ATP from phosphate and ADP [35]. The F0 portion is the ion “turbine” which exchanges ions for a rotary “shaft” motion. This shaft in turn drives conformational changes in the f1 portion that provide the energy to produce ATP. Extensive conformational dynamics are also a general feature of the polymeric properties of disordered biomolecules. The dynamics can have positive or negative effects. The conformational dynamics of disordered polypeptide chain combined with specific interactions between residues drives protein folding [36, 37]. The dynamics of the long DNA molecules in eukaryotes are reined in by wrapping them on histones [38]. Without these restraints, entanglement and breakage would often occur. The ability to monitor such conformational dynamics on individual molecules is one of the most promising applications of single-molecule spectroscopy.

2.1. Single-molecule observables for conformational dynamics

The two primary tools used in single-molecule fluorescence spectroscopy to measure conformational dynamics are Fluorescence Resonance Energy Transfer (FRET) and Fluorescence Polarization Anisotropy (FPA). FRET is used to monitor changes in distance between two fluorophores attached to two points in the same molecule, while

FPA is used to monitor changes in the orientation of the molecules or in the freedom of rotational motion of the fluorophore. Both can be monitored with ratiometric and lifetime measurements: in single-molecule measurements, ratiometric measurements are performed by comparing the numbers of photons counted in distinct detection channels, and lifetime measurements are performed using Time-Correlated Single Photon Counting (TCSPC; described later).



2.1.1. Fluorescence Resonance Energy Transfer

FRET is the non-radiative transfer of electronic excitation energy from donor to acceptor fluorescent molecules via a weak dipole-dipole coupling mechanism. Fig. 2.1

illustrates the important parameters that affect FRET. FRET requires a resonance between the emission of a donor molecule and the absorption of an acceptor molecule, and depends critically on the relative orientations of the dipole moments of the donor and acceptor molecules (Fig. 2.1A). Most importantly, FRET has a strong dependence on the distance between the two fluorophores (Fig. 2.1B). The rate of FRET between a donor fluorophore and an acceptor fluorophore at a distance R is given by

$$k_{\text{FRET}} = \frac{1}{\tau_D} \left(\frac{R_0}{R} \right)^6 \quad (2.1)$$

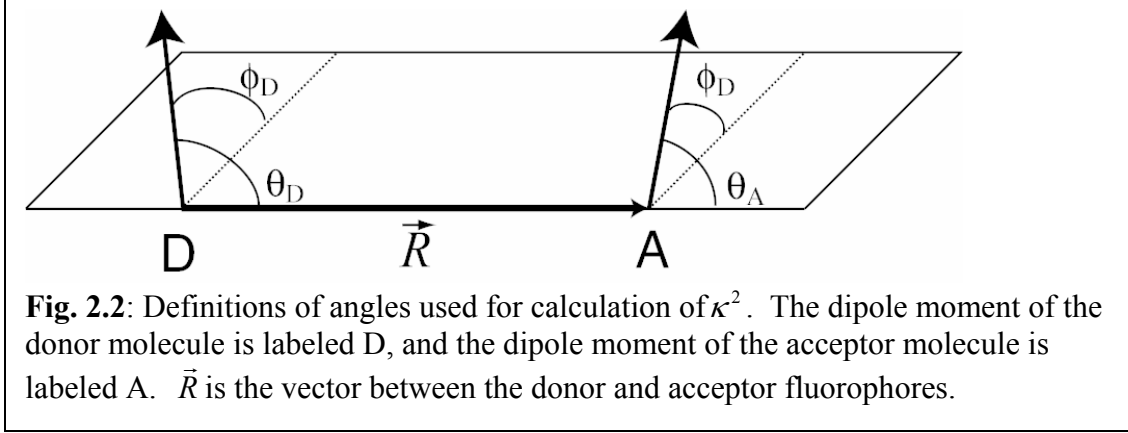
where $\tau_d = 1/k_d$ is the fluorescence lifetime of the donor in the absence of the acceptor and R_0 is the distance at which the fraction of excitations transferred to the acceptor is 50%. R_0 is given by,

$$(R_0)^6 = \frac{9000(\ln 10)\kappa^2 Q_d}{128\pi^5 N n^4} \int_0^\infty F_d(\lambda) \varepsilon_a(\lambda) \lambda^4 d\lambda \quad (2.2)$$

where Q_d is the quantum efficiency of the donor, N is Avogadro's number, n is the index of refraction of the medium between the fluorophores, F_d is the normalized emission spectrum of the donor, $\varepsilon_a(\lambda)$ is the extinction coefficient of the acceptor at the wavelength λ , and κ^2 is the orientation factor for the interaction between the donor and acceptor. The two most problematic factors are n and κ^2 . The index of refraction n depends on the solution and the organic matter (protein or DNA) that lies between the two fluorophores. The second problematic factor is the orientation factor κ^2 , given by the following equation:

$$\kappa^2 = \left[\sin \theta_d \sin \theta_a \cos(\phi_d - \phi_a) - 2 \cos \theta_a \cos \theta_d \right]^2 \quad (2.3)$$

The definitions of these angles for the donor and acceptor fluorophores are shown in Fig. 2.2. If rotational diffusion is very fast compared to the fluorescence lifetime, it is



possible to substitute the value $\kappa^2 = 2/3$ in (2.2). If not, then the range of possible values for κ^2 must be accounted for in calculations of distance [39].

The energy transfer efficiency E (or quantum yield for energy transfer) is calculated by comparing the rate of FRET k_{FRET} to the rate of de-excitation of the donor singlet excited state ($k_d = 1/\tau_d$),

$$E = \frac{k_{\text{FRET}}}{k_{\text{FRET}} + k_d} \quad (2.4)$$

E decreases with R , the distance between the two dyes, $E = 1/\left[1 + (R/R_0)^6\right]$ [40]. Stryer and Haugland's work demonstrated this distance dependence in 1967, [41] and since then, FRET has been used as a spectroscopic ruler in ensemble experiments [40, 42]. It allows distance measurements on the 20-80Å scale and is a tool well suited to studying conformations of biological macromolecules. FRET was first observed at the single molecule level in 1996 by Ha et al, who used near field optical microscopy to observe energy transfer between two dyes on a dry surface [43]. More recently, Deniz et al used

the diffusion FRET methodology to inspect the distance dependence of FRET at single molecule resolution [33]. During the past few years, spFRET has been used in a variety of biological applications including DNA [33], RNA [44, 45], and protein folding [46-48], enzyme reactions [49], peptide-calcium binding in solution [50] and receptor-ligand binding on cell surfaces [51], and signal transduction [52]. spFRET measurements can be used to probe not only average distances as in an ensemble experiment, but also to directly observe distributions and the time-evolution of conformational (distance) properties.

Two expressions for the FRET efficiency E are important for single-molecule FRET measurements. The first expression will be used to obtain E from fluorescence lifetime measurements. The lifetime of the donor in the presence of FRET is $\tau'_d = (k_d + k_{\text{FRET}})^{-1}$. Using this with Eq. (2.4), we obtain the following expression for the FRET efficiency E in terms of measured fluorescence lifetimes.

$$E = 1 - \frac{\tau'_d}{\tau_d} \quad (2.5)$$

The second expression for E is developed for fluorescence intensity measurements. Ignoring saturation effects, the measured fluorescence intensity in the donor channel D is

$$I_D = \sigma_d I_{\text{exc}} \varphi_d (1 - E) d_{d \rightarrow D} + \sigma_d I_{\text{exc}} \varphi_a E d_{a \rightarrow D} + \sigma_a I_{\text{exc}} \varphi_a d_{a \rightarrow D} \quad (2.6)$$

The measured fluorescence intensity in the acceptor channel A is

$$I_A = \sigma_d I_{\text{exc}} \varphi_d (1 - E) d_{d \rightarrow A} + \sigma_d I_{\text{exc}} \varphi_a E d_{a \rightarrow A} + \sigma_a I_{\text{exc}} \varphi_a d_{a \rightarrow A} \quad (2.7)$$

σ_d and σ_a are the absorption cross-sections of the donor and acceptor, respectively, at the excitation wavelength, and I_{exc} is the laser intensity. φ_d and φ_a are the quantum

efficiencies of the donor and acceptor, respectively. $d_{d \rightarrow D}$ and $d_{d \rightarrow A}$ are the detection efficiencies for donor fluorescence in the donor and acceptor channels, respectively. $d_{a \rightarrow D}$ and $d_{a \rightarrow A}$ are the detection efficiencies for acceptor fluorescence in the donor and acceptor channels, respectively. On the right hand side of Eqs. (2.6) and (2.7), the first term is the contribution from the donor, the second term is from the FRET sensitized emission of the acceptor, and the third term is from direct excitation of the acceptor. The emission spectra of most organic fluorophores are asymmetric, with a long tail toward the red, but not toward the blue. Because of this, the detection efficiency of the acceptor in a suitably chosen donor channel is typically negligible ($d_{a \rightarrow D} \approx 0$), whereas the detection efficiency of the donor in the acceptor channel ($d_{d \rightarrow A}$) is not. In the discussion of the next sections, the direct excitation of the acceptor is neglected ($\sigma_a = 0$) since the absorption of the acceptor used (Cy5) is small compared to that of the donor molecule (TMR). Using these assumptions, Eqs. (2.6) and (2.7) can be rewritten,

$$E = \frac{1}{1 + \gamma \left[I_D / (I_A - I_D d_{d \rightarrow A} / d_{d \rightarrow D}) \right]} \quad (2.8)$$

where $\gamma = \frac{\varphi_a d_{a \rightarrow A}}{\varphi_d d_{d \rightarrow D}}$ is a correction factor that contains components from detection efficiencies, and fluorescence quantum yields. Hence, measurement of the ratio (I_d / I_a) allows ratiometric determination of E in single-molecule experiments.

2.1.2. Polarization anisotropy

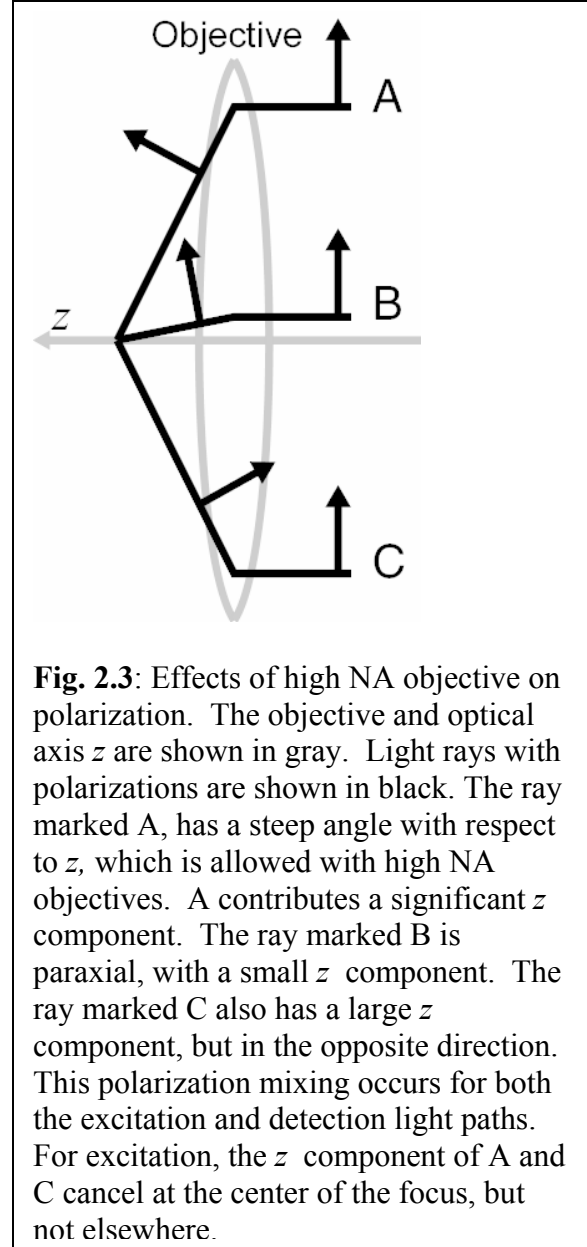
Polarization properties of the emitted fluorescence provide information about the reorientational properties of the fluorophore on the timescale of the fluorescence lifetime

[40]. For polarization anisotropy measurements, a laser polarized along the z axis excites the fluorophore. The distribution over (θ, ϕ) ($\theta = 0$ is the z axis) of dipole orientations excited by the laser is equal to $P(\cos \theta, \phi) d \cos \theta = 3/2 \cos^2 \theta d \cos \theta$. After the excitation, the dipole orientations diffuse, and this distribution relaxes eventually to a uniform distribution, $P(\cos \theta, \phi) d \cos \theta = 1/2 d \cos \theta$. Until the dipole orientation relaxes to the uniform distribution, the emission is on average polarized in the direction of the excitation polarization. The anisotropy r is a measure of how much of the emitted light is parallel to the excitation and how much is perpendicular: $r = \frac{I_{\parallel} - I_{\perp}}{I_{\parallel} + 2I_{\perp}}$. There is a competition between the rate of fluorescence (given by the inverse of the fluorescence lifetime τ) and rotational diffusion. r can have values in the range 0 to 0.4 for a random initial distribution (0 for very fast diffusion and 0.4 for very slow diffusion compared to the lifetime). Immobilized single molecules can have values from -0.5 to 1.0 . The Perrin equation gives the value of anisotropy as a function of these variables: $\frac{r_0}{r} = 1 + 6D_{\text{rot}}\tau$. r_0 is the “fundamental anisotropy”, which accounts for depolarization effects if the excitation and emission dipoles do not overlap. If they overlap, then $r_0 = 0.4$. Time-resolved anisotropy measurements track the time scale of rotational diffusion for the molecules by measuring $r(t)$, where t is the time since an exciting laser pulse.

For single-molecule measurements, the polarization anisotropy signal is obtained using a high numerical aperture (NA) microscope objective. Polarization mixing occurs when using high NA objectives. The cause of this effect can be seen in Fig. 2.3: high NA

objectives refract optical rays at high angles, causing significant z components for the polarization in the region near the focus. Expressions for r have been developed that take into account this polarization mixing [53, 54]. These are not discussed here, since this work focuses primarily on FRET experiments. We point out however, that polarization anisotropy measurements performed on the donor and acceptor allow limits to be placed on the values for κ^2 , improving confidence in distances extracted using FRET.

Polarization anisotropy has been used extensively in both steady state and time-resolved formats in biological applications such as protein folding and drug-protein interactions [40]. At the single-molecule level [54] polarization properties have been used to distinguish components of mixtures [34], to measure changes in myosin light-chain orientation

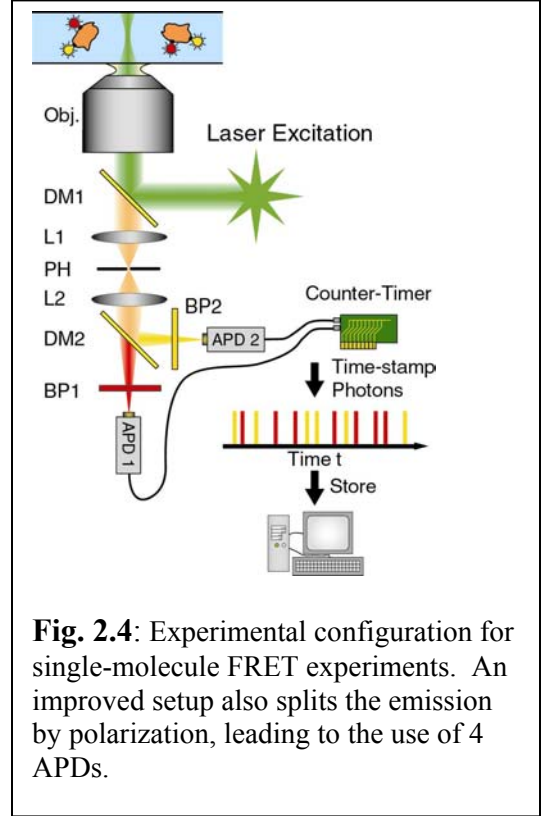


[55] and to observe the rotation of single F1-ATPase molecules [56]. A striking example is the F1-ATPase work by Adachi et. al.[57], where the 120° rotation steps of the central γ -subunit during the hydrolysis of ATP were directly monitored in real-time. They

achieved this by monitoring the fluorescence polarization properties of single dye molecules attached to the γ -subunit, and were able to demonstrate that the rotation rate was load independent. Polarization methods might find their most powerful applications in monitoring the activity of single motor proteins as they move along DNA. From a synthesis and data collection perspective, polarization measurements are advantageous over FRET, as they often require labeling with only a single dye, and suffer less from interpretation ambiguities. However they do not provide distance information, and are best used when angular conformational changes are expected, such as in F1-ATPase.

2.2. Data acquisition

Briefly, our experimental setup for the single-molecule experiments [33, 58] consists of laser excitation, and detection via an inverted confocal microscope (Zeiss Axiovert S100 TV) coupled to a high-sensitivity detection setup (see Fig. 2.4). An air-cooled argon ion laser is used for the experiments in sections 2.3.3 and 2.4.2, while a mode-locked Titanium-Sapphire laser tuned to 1 μm , and doubled to 500 nm, is used for the demonstration experiments with time-correlated single photon counting in section



2.3.5 (laser excitation is shown in green in Fig. 2.4). Later, a 532 nm pulsed diode laser is used for excitation for the CI2 experiments in section 2.4.3. Upon introducing the laser into the microscope with a dichroic mirror (DM1), a tight focus is created by focusing the laser excitation through a high numerical aperture (NA 1.3) oil immersion objective (labeled “obj.” in Fig. 2.4). In order to detect freely diffusing single molecules, the focal point is placed within the low concentration (<100pM) sample solution, and fluorescence emission is collected through the same objective and focused by a lens (L1) onto a pinhole (PH) to reject out-of-focus light. The effective confocal volume is on the order

of 1 fl, which for a 100 pM solution corresponds to an occupancy of 0.06 molecules per detection volume. The fluorescence is then split into two parts, via a dichroic mirror for FRET (DM2) and/or a polarizing beam splitter cube for polarization anisotropy, which are separately focused onto two avalanche photodiodes detectors (APDs, SPCM-AQR-14, PerkinElmer), used for single photon counting. The output pulses of the APDs are timed using a counter-timer board (PCI-6602, National Instruments). The overall detection efficiency is estimated to be on the order of a few percent [58], and with typical dyes, peak count rates of 10KHz –1MHz are observed. For FRET measurements, the dye pair is typically composed of TMR (donor, peak emission at 575 nm) and Cy5 (acceptor, peak emission at 670 nm); the large extinction coefficient of Cy5 (250,000) allows a good spectral separation while maintaining a large R_0 of about 65Å.

For TCSPC, a pulsed laser is used to excite a sample, and the time between a photon's arrival and the next laser pulse is measured with sub-nanosecond accuracy. Histograms formed from binning the photons by this “microscopic” arrival time are fitted to obtain fluorescence lifetime of the fluorophore under investigation. For ensemble measurements, one accumulates photons until the histogram is sufficiently accurate for the needed analysis. In single-molecule measurements, the arrival time of the photon is also measured with respect to a global clock (100ns accuracy). This is called the “macroscopic” arrival time. The raw data is thus a list of photons, each tagged with the detector channel, the microscopic arrival time and the macroscopic arrival time. The relative timing of the photons is then known, allowing photon bursts from single molecules to be sifted from the data, which is the first step in solution-based single-molecule data analysis.

For the TCSPC measurements described here, the APD signals are routed through a Time-to-Amplitude converter (TAC, EG&G Ortec 567) to an Analog-to-Digital converter board (PCI-6111E, National Instruments) to measure the time between the laser pulse and the photon arrival time. A single commercial board can be used for the entire process (PicoQuant TimeHarp 100) or (Becker and Hickl SPC-630), which simultaneously measures the macroscopic timing of the photon (100ns time scale or 50ns time scale) and the microscopic arrival time with respect to the laser pulse (100ps time scale). A different gating delay for each APD channel allows multiple channel detection with a single TAC or TimeHarp board. A special signal router (HRT-82, Becker and Hickl) is used with the Becker and Hickl SPC-630.

Four APDs are used for the experiments in section 2.4.3. A linearly polarized excitation source is introduced, and the emission is split by polarization as well as by spectrum. Therefore, there are channels for vertically and horizontally polarized TMR emission, as well as vertically and horizontally polarized Cy5 emission.

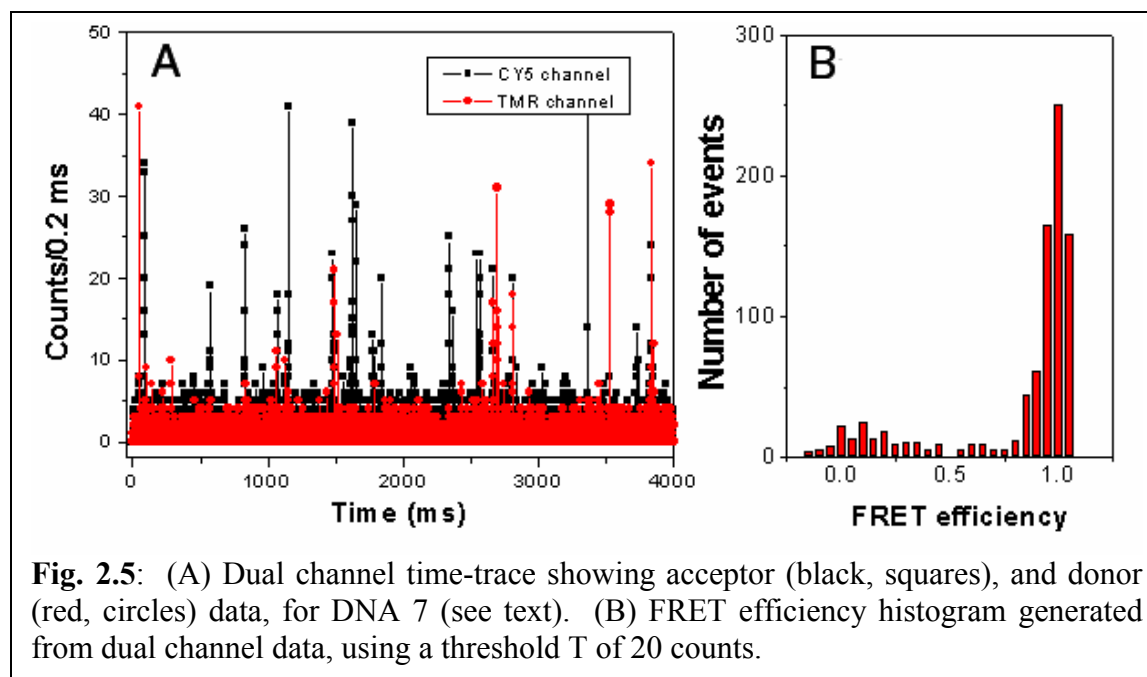
The setup described so far measures the time intervals between photons to 10-100 ns accuracy (depending on the computer card used). When calculating the correlation function estimate, $G(\tau) = \langle I(t)I(t+\tau) \rangle / \langle I(t) \rangle^2$, used in FCS, this means that dynamics that are on a faster time scale cannot be measured. To probe dynamics using correlation function estimates on a faster time scale, we use the Time-to-Amplitude Converter (TAC, EG&G Ortec 567) to measure the difference in photon arrival times to subnanosecond accuracy over time ranges of 100 ns – 1 μ s. Because the probability for receiving two photon within these time scales is small, the time interval statistics acquired in this manner are equivalent to correlation function estimates [59].

2.3. Single-molecule data analysis for diffusing species

Every photon emitted by a fluorophore contains several types of information. Because of this, single-photon counting data generated in single-molecule experiments can be used to extract several physical parameters of the emitting system. Each emitted photon can be characterized with respect to excited-state duration, polarization and spectral position, and the time delay from the previous emitted photon. Integration over several such single-photon values can result in fluorescence intensity, lifetime, and related information. The photon information can be used to generate ratiometric histograms, lifetime curves, correlation estimations and distributions from burst analysis, such as diffusion and intensity distributions. A key point here is the ability to draw correlations between the results from these different kinds of analyses. The groups of Keller and Seidel have pioneered such multi-dimensional analyses methods, mainly in order to minimize the error rates in identification of subpopulations during single-molecule DNA sequencing and other proposed applications [34, 60]. In the current context, the methods discussed here offer the ability to separately monitor and carry out the above analyses on photons emitted by individual subpopulations in a mixture. The following sections discuss a few illustrative examples of such analysis methods. The focus of our work is on FRET, but these methods can be applied to polarization experiments as well.

2.3.1. Single-molecule ratiometric data analysis for diffusing species

In 1999, two groups demonstrated the ability to make ratiometric measurements on freely diffusing molecules; our group used single pair fluorescence (or Förster) resonance energy transfer (spFRET) to identify and record changes in subpopulations in a mixture [33, 58], while the Seidel group used polarization anisotropy to increase the classification confidence for components in a mixture [34]. The ability to distinguish subpopulations and to classify collected photons or photon bursts according to these subpopulations, is a key feature of the single-molecule methodology for diffusing species. Due to their low intensities, single-molecule signals suffer from intrinsic fluctuations. Such fluctuations are amplified in diffusion measurements due to the variation in the excitation intensity experienced by the molecule as it diffuses through various regions of the focal volume. The ratiometric method, in effect, provides a way to normalize the data with respect to many of these fluctuations. This simplifies the data interpretation, and makes it possible to extract several parameters of interest with a minimum of complex modeling and data analysis. Hence, ratiometric diffusion methodologies have been developed to study unperturbed biological molecules in the solution environment. Using their ability to quickly resolve static structural distributions and subpopulations in mixtures, it is possible to measure submillisecond structural dynamics of individual subpopulations, measure slower changes in properties of subpopulations, and perform appropriate controls during the development of immobilization methods. In the following sections, we describe the development of ratiometric diffusion single-molecule methods, with a focus on spFRET and its application to protein folding and polymer physics problems.



For ratiometric FRET experiments, the donor (TMR) is excited, and the donor and acceptor (Cy5) emission are separately and simultaneously detected. Pairs of data points corresponding to the number of detected photons in the two channels, I_d and I_a , are recorded with integration times ranging from 0.2 – 1ms; this data can be used to plot FRET histograms (this is referred to as “point-wise analysis”) [33]. A better method is to record the time lag between successive photons with submicrosecond time-resolution, for each channel. This permits the construction of FRET histograms, and also analysis by burst and correlation methods (see below). Fig. 2.5A shows a time trace of dual detector (0.2 ms integration time) data for donor-acceptor labeled DNA molecules. Due to the low concentration, most of the points consist of background signal, resulting predominantly from Raman and Rayleigh scattering, while the occasional peaks correspond to single donor-acceptor labeled DNA molecules diffusing through the focal volume and emitting bursts of photons. The durations of these bursts (mean of about 200 μ s) are determined by

the molecular diffusion rate, while their amplitudes depend on several factors, such as the diffusion path of the molecule through the focal volume and the photophysical properties of the dyes.

The time trace shows fluorescence bursts on both the donor and acceptor channels. Since direct excitation of the acceptor is negligible, and leakage of the donor emission into the acceptor channel is small, large bursts on the acceptor channel result from Cy5 emission due to energy transfer. A simple approach is used to extract FRET information from these photon bursts. First, a threshold is used to discriminate dye signal from the background noise. That is, pairs of data points from a time bin are accepted only when the sum of the signals ($I_a + I_d$) is above a given threshold T . The threshold value is chosen to effectively reject background while retaining as many points as possible. We term this the “SUM” rejection criterion. For the accepted events, the FRET efficiencies are calculated according to Eq. (2.8), and collected in a histogram (Fig. 2.5B). The correction factor γ is estimated to be about 1 from surface-immobilized molecules [49], and is used for the data presented here.

The above background rejection procedure is chosen to allow quick and simple processing of data while minimizing the bias of the thresholding criterion. Defining a corrected acceptor intensity, $I'_A = I_A - I_D d_{d \rightarrow A} / d_{d \rightarrow D}$, Eq. (2.8) can be rewritten as:

$$I'_A + \gamma I_D = I'_A / E \quad (2.9)$$

Substituting $I'_a = E \sigma_d I_{\text{exc}} \varphi_a d_{a \rightarrow A}$, we can write:

$$I'_A + \gamma I_D = I'_A / E = \sigma_d I_{\text{exc}} \varphi_a d_{a \rightarrow A} \quad (2.10)$$

showing that the sum $I'_A + \gamma I_D$ is independent of the FRET efficiency. Our intention is to identify and study the properties of subpopulations or distributions of molecules based on

their FRET efficiencies. Hence, using the “SUM” criterion is the simplest procedure for background rejection that provides representative data sampling without a bias with respect to E .

Fig. 2.5B shows a representative FRET efficiency histogram from data for a double stranded DNA 7 molecule, where the donor and acceptor dyes were separated by 7 base pairs. Two peaks are observed, one at efficiency greater than 0.95, and the other close to zero. The high efficiency peak is consistent with expectations based on the calculated distance between the dyes. The “zero peak” implies fluorescence bursts with emission from donor only. It has contributions from several sources, including solvent impurities, molecules with donor dyes only, accelerated photobleaching of the acceptor during the single-molecule experiment and cis-isomers of the acceptor dye [61]. Although the “zero peak” is problematic for analysis of histograms with low FRET peaks ($E < 0.3$), it is less relevant for the $E > 0.4$ portion of the histogram, where FRET peaks (distributions) may be analyzed to reveal their various moments, mean E , area and widths. Although gaussian functions are often used for fitting the histograms, these are only appropriate between about 0.2 and 0.8 E , especially for the extraction of mean E , and width [58]. Outside this range, the non-symmetric shape of the distributions is fit better using beta functions. Finally, these histograms may be used to identify and individually follow subpopulations of molecules based on differences in E .

2.3.2. Moments of peaks in the measured histograms

While the moments extracted from the E histograms give approximate measures of populations, distance means and distributions, they are skewed due to contributions from other factors. Next, we discuss the γ factor, shot-noise, orientational distributions

and fast distance-fluctuations, and some methods that may be used to quantify and separate out their contributions. Given the uncertainties in the estimated E values, some authors refer to them as proximity ratios [44, 45, 62].

The scaling factor γ can influence both the mean and width of E distributions. While this factor is hard to pin down accurately, lifetime based methods to measure E independently will prove very useful for this purpose. Another major contributor to the widths is shot-noise. The emissions of both fluorophores (I_a and I_d) exhibit approximately Poisson distributions, with mean values that depend on the excitation intensity and the photophysical characteristics of the dyes [58]. For the observed low signals, relative variations play a significant role. This results in distributions in the computed E , which in turn results in lower limits for the widths of the E histogram peaks.

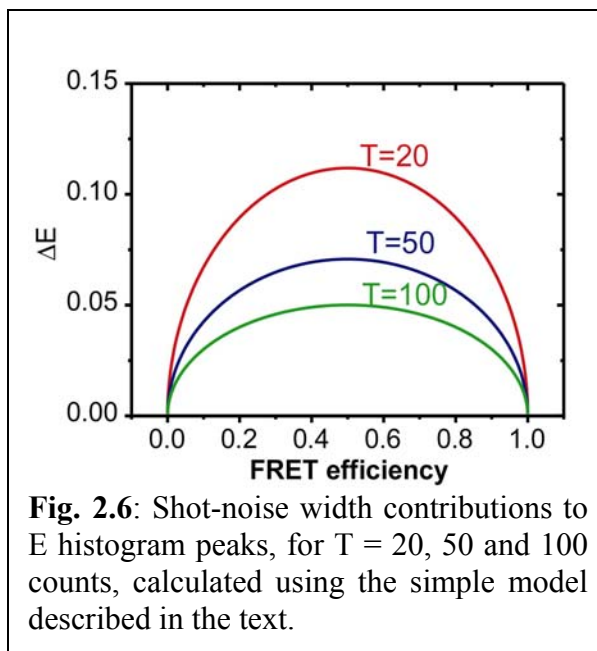
To estimate this limit, a simple model was first used in which both emission channels I_a and I_d are described by Poisson variables [58]. Their mean values are $\mu_a = E_m \cdot T$ and $\mu_d = (1 - E_m) \cdot T$ respectively, where E_m is the mean transfer efficiency and T is the “SUM” threshold used in the analysis. Since only signals above this threshold are processed, they have a smaller relative shot noise and hence, this calculation places an upper bound on the calculated values. The formula reads [63]:

$$(\Delta d)^2 \approx \left(\frac{\partial d}{\partial I_A} (I_A = \mu_A, I_D = \mu_D) \right)^2 \Delta I_A^2 + \left(\frac{\partial d}{\partial I_D} (I_A = \mu_A, I_D = \mu_D) \right)^2 \Delta I_D^2 \quad (2.11)$$

where d is the ratiometric observable, and for FRET efficiency, $d = E = I_a / (I_a + I_d)$. Using this formula, the FRET width (standard deviation) is given by $\Delta E = \sqrt{E_m (1 - E_m) / T}$. The solid lines in Fig. 2.6 display the upper bound estimates for $T = 20, 50$ and 100 . The shot-noise induced fluctuations strongly depend on the FRET mean value with a

maximum at $E = 0.5$, and clearly show the expected decrease with increase in signal intensity.

More accurate models will include the effects of distributions of photon counts, and diffusion of the molecules in the focal volume [58]. In addition to shot-noise, distributions in E depend on distributions in the Förster radius R_0 and, more



interestingly, in the distance between the two dyes. The dominant factor in R_0 fluctuations is κ^2 , the orientational factor, which depends on the relative orientation of the two dipoles. A common assumption is that the two dyes are freely rotating on a time scale comparable to or faster than the fluorescence lifetime, and that κ^2 can be dynamically averaged to a fixed value of $2/3$ [40]. However, a combination of results from steady state polarization measurements and simulations shows that the presence of hindered rotation can cause both peak broadening and small shifts in mean E [46].

Fluctuations or distributions of distances between the two dyes can give rise to shifts and distributions in E . From a structural biology point of view, this is the most interesting case, as distance measurements are of interest in conformational fluctuations in proteins, in end-to-end fluctuations of polymers, and in protein folding. Haas and co-workers first developed ensemble time-resolved FRET techniques, data analysis, and modeling to extract such distributions from ensemble data [64]. Single molecule

methods might shed new insights in this context [65]. It is noted that fast fluctuations are averaged out within the measurement period and will not contribute to the observed widths, though they will shift the mean E to a higher value. However, slower distance fluctuations from conformational or dye-biomolecule interactions can contribute significantly.

Relative areas of subpopulations are particularly useful as they provide a measure for the occupation probabilities of a particular state by the molecular system; this ability is used to calculate protein denaturation curves in section 2.4 [46]. Relative areas can potentially be influenced by biased background rejection algorithms, and also by different photophysics, photochemistry or diffusion time between the different subpopulations.

In summary, many contributions affect the parameters that are extracted from the E histograms. While this can be problematic for accurate measurements, the studies we describe in the following sections demonstrate that it is nevertheless possible to extract new and meaningful information from these histograms. These issues need to be investigated in greater detail using improved spacer constructs and more advanced data collection and analysis methods, where some of the above contributions can be ruled out or corrected for.

2.3.3. Burst and fluctuation analysis methods

Bursts of fluorescence photons in diffusion experiments may be identified and further analyzed either at the point-wise or the full burst levels. For the point-wise analysis, the signal is merely integrated over a specified sampling interval. Alternately, for the burst analysis, the data is first processed to identify groups of photons emitted by a specific molecule as it traverses the focal volume. While the point-wise analysis is

simpler, and provides the possibility to control the averaging timescale, burst analysis can offer larger signal and consequently lower relative shot noise. However, burst analysis can have the disadvantage of greater averaging over interconverting subpopulations during a burst, and these two analysis methods should be considered complementary. Identification of bursts, followed by analysis of subdivisions of these bursts is even more powerful, as it incorporates the advantages of both methods. Fries et al have described the burst integrated fluorescence lifetime (BIFL) method, where they analyze distributions of bursts with respect to size, duration and lifetime, allowing them to resolve mixtures of dyes [34].

Fluorescence autocorrelation analysis was introduced by Magde, Elson and Webb nearly three decades ago [66], and more recently received renewed attention by Eigen and Rigler as a method with broad implications for the modern biotechnology industry [21]. Although the autocorrelation function itself disregards a considerable amount of temporal information, FCS is a very powerful method that can provide information on fluorescence fluctuation timescales and amplitudes at equilibrium, over a wide timescale range [28]. Recently, two-color cross-correlation analysis has been used to study DNA cleavage [29], binding of DNA duplexes to transcription activator protein complexes [31], and detection of pathological prion protein aggregates [19, 20].

A drawback of cross-correlation FCS, as conventionally practiced, is that it results in information averaged over individual subpopulations, making it hard to deconvolute out contributions from individual subpopulations of molecules. The ratiometric single molecule approach allows us to add the capability to separate subpopulations to such correlation analyses. By storing the arrival times of photons in a FRET experiment, a

cross correlation between donor and acceptor channels affords the ability to measure kinetics of processes that result in changes in E. In contrast to the earlier two-color cross correlation, such fluctuations result in negative correlations, which allows them to be distinguished simply from other fluctuation processes that result in a positive correlation [50]. Furthermore, the same arrival time data may be used to plot a FRET histogram, followed by a correlation analysis of signals that correspond to subsets of this histogram. In this manner, fluctuations in distances shorter than the diffusion time can be monitored (see section 2.5).

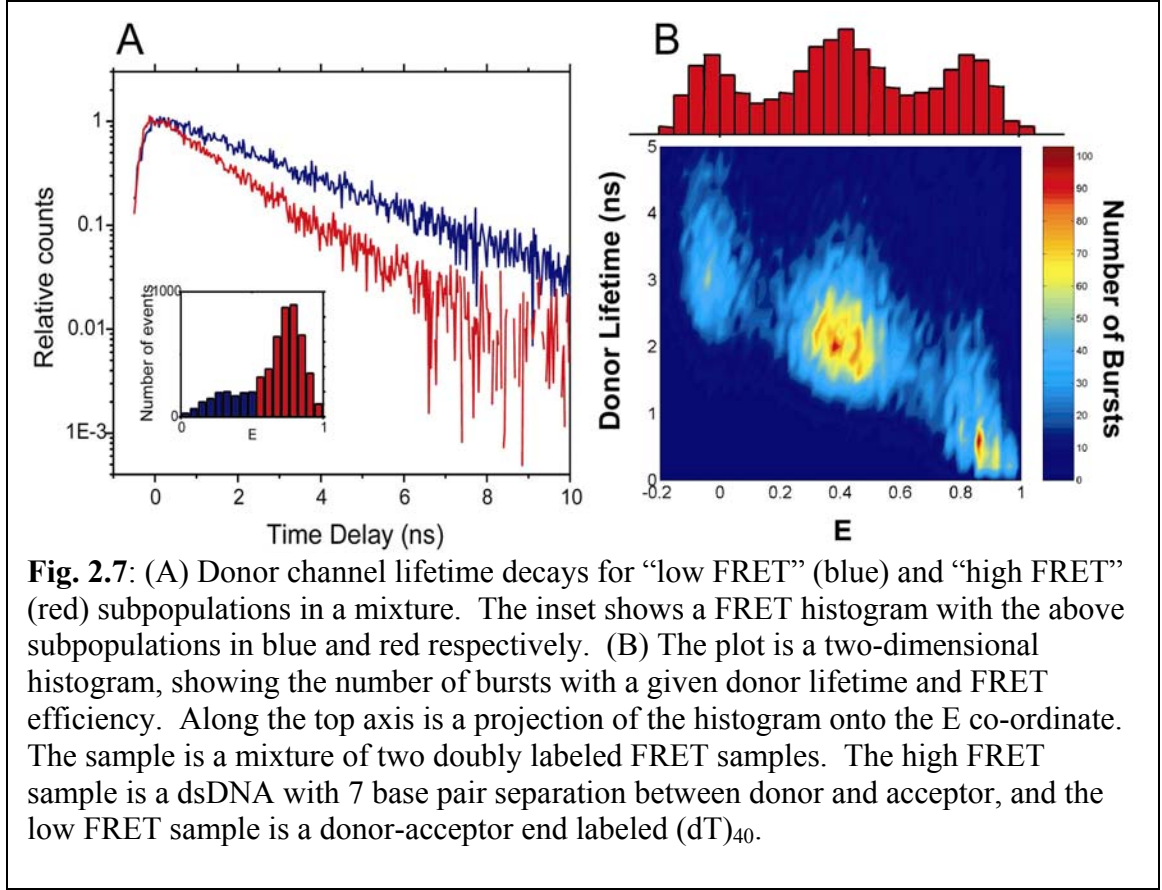
In addition to first order correlations such as the above, higher order correlations may be employed. These afford the ability to investigate the contributions of non-Markovian dynamics, as recently discussed in the analysis of data for flavoenzyme [67, 68] and horseradish peroxidase catalysis [69, 70]. These authors interpret their observations as evidence for the presence of multiple conformational substates indistinguishable by their fluorescence. Finally, burst and correlation analysis methods, in conjunction with ratiometric separation of subpopulations, might prove useful for detection of aggregation processes, such as between cell-surface receptors during signaling, between misfolded proteins resulting in disease, or proteins with DNA during cellular processes, where differences in molecular brightness and/or diffusion rates are expected.

2.3.4. Time-correlated single-photon counting

Even more information can be extracted by collecting data in a time-correlated manner as described in section 2.2. Single-molecule detection and analysis by this method has been used by several groups in a single channel detection mode [32, 60].

This method can be used to classify photon bursts according to lifetime, allowing the identification and quantification of components in a mixture with different lifetimes. This approach has specifically been developed as a tool for single-molecule DNA sequencing applications using a single excitation source and single detector. Van Orden et al have shown that simultaneously measuring burst size and intraburst fluorescence lifetime increases the accuracy of identification of subpopulations in a mixture [60]. Lamb et al have used the arrival time information in conjunction with FCS experiments to study heterogeneity of solutions [71]. The group of Seidel first used two-channel lifetime detection in combination with ratiometric polarization anisotropy measurements, in an approach termed the multidimensional BIFL technique [34]. Here, the authors recorded each photon using both the time-lag and time-correlated data collection approaches, and then analyzed the photons emitted during single bursts to classify molecules based on steady-state anisotropy, burst size, and time-resolved anisotropy decay.

Using this lifetime capability, an interesting analysis may be carried out with ratiometric data collection. Ratiometric diffusion histograms are first plotted to identify subpopulations, then the arrival-time histogram is plotted for all the photons corresponding to a particular subpopulation of molecules. A simple example of such a separation is illustrated in Fig 2.7A, where a donor-acceptor DNA molecule is studied. Here, a FRET histogram is plotted in the inset, showing the separation of subpopulations corresponding to the “zero peak” (blue), and doubly labeled DNA molecules (red); the figure shows donor lifetime for these two subpopulations. The high FRET component (red) clearly shows the accelerated decay due to energy transfer. The acceptor lifetime



decay also showed a similar change. While lifetime analysis may be carried out on individual bursts, the advantage of the current method is that it provides a larger number of photons and can be used for identifying multiple or distributed exponential decays.

This is particularly interesting for the use of FRET measurements to look at subpopulations interconverting on the sub microsecond timescale, and fluctuations of proteins, DNA and other polymers, as first demonstrated by the pioneering ensemble work of Haas et.al [64]. End-to-end distance distributions or fluctuations in donor-acceptor labeled polymers results in non-exponential decays of donor and acceptor fluorescence lifetime. Several groups have used analyses of such non-exponential donor decays to identify peptide, protein, DNA and RNA conformational distributions [40]. Since the analysis of such decays relies on complex models, it is of great utility to be able

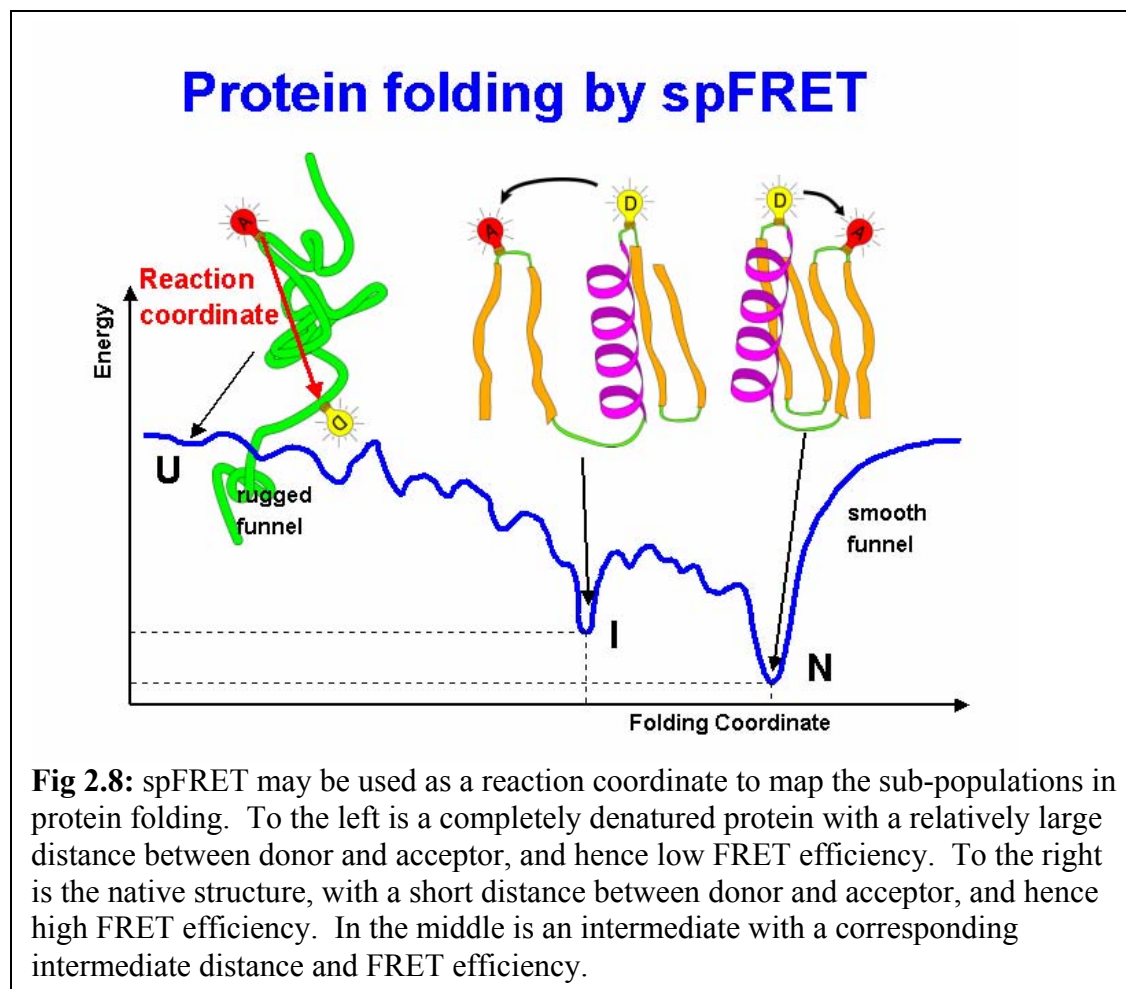
to first directly separate out lifetime components of subpopulations using the ratiometric single-molecule approach, followed by further analyses of these separate decays. In particular, this approach is being pursued to investigate the unfolded state of CI2 in the region showing possible changes in the protein dimensions, and for the study of fluctuations in ss-DNA.

Fig 2.7B demonstrates how lifetime information can be used in conjunction with ratiometric observables to facilitate separation of fluorescence bursts into subpopulations. The data are taken from a mixture of DNA molecules consisting of high FRET and lower FRET subpopulations. The plot is a two-dimensional histogram, showing the number of fluorescence bursts with a given donor lifetime and FRET efficiency, E . The projection along the top axis is the one-dimensional histogram of E . For both graphs, the peak corresponding to the high FRET subpopulation is on the right. The peak of the lower FRET subpopulation is in the middle, and the “zero FRET” peak is on the left. Because the donor lifetime decreases as E increases, the separation between subpopulations is improved when using the additional information from lifetime. An extension of these lifetime methods, is to have four detection channels, each recording both time-lag and lifetime information. This setup, which can monitor polarization properties of each FRET channel, is used in section 2.4.4.

2.4. Protein folding of Chymotrypsin Inhibitor 2 (CI2)

We now discuss the application of single-molecule FRET methods to the protein folding of Chymotrypsin Inhibitor 2 (CI2) [46]. The folding mechanisms of proteins have been intensely studied using both experimental and theoretical methods. However, since protein folding is extremely complex, no single observable or technique is sufficient to fully describe it. Hence, new technologies have constantly been applied to the folding problem, providing new experimental observables and deeper insights into the problem. Technical developments have recently facilitated crossing the fundamental threshold from ensemble to single-molecule studies, providing access to information unavailable from bulk studies. Several important aspects of protein folding and dynamics are difficult or impossible to study using ensemble methods, due to the complexity of protein structures and the stochastic nature of these processes. Key examples of this complexity include (1) the ensemble of unfolded protein molecules, consisting of a large number of nearly degenerate and rapidly inter-converting protein conformations [36, 37], (2) multiple local minima on a rugged energy landscape which can give rise to fluctuations and several conformational substates even for the native protein, and (3) ensembles of folding pathways and “transition states” for the folding reaction. Hence, the dynamics of folding reactions are expected to be highly stochastic; such stochastic aspects are clearly best studied at single-molecule resolution. Single-molecule methods are also useful to directly monitor static or dynamic distributions in the properties of individual sub-populations, at equilibrium in a mixture of species, and under non-

equilibrium conditions. Finally, from a theoretical standpoint, most calculations are carried out at the single-molecule level. Hence, single-molecule experiments provide the most direct experimental benchmarks and tests for theory. In particular, the dramatic increase during recent years of theoretical methods applied to the folding problem makes such single-molecule studies very attractive [72-77].



We use spFRET as a reaction coordinate to map the number of sub-populations in protein folding. The idea is illustrated in Fig. 2.8. An unfolded protein, shown to the left in Fig. 2.8, has a larger average distance between the donor and acceptor (and hence lower FRET efficiency) than a folded protein, shown to the right. An intermediate would

typically have a distance and FRET efficiency somewhere in between the folded and unfolded proteins.

2.4.1. Materials and methods for CI2

2.4.1.1. Protein molecules

The protein was synthesized using conformationally assisted ligation of two peptide fragments of CI2 [78]. Peptides corresponding to CI2(1-39) and CI2(40-64) were synthesized separately using manual solid phase peptide synthesis [79, 80]; the C-terminal (1-39) fragment was synthesized on TAMPAL resin to afford a C-terminal thioester [81]. For donor-acceptor labeled protein, the N-terminal amine of the (1-39) piece was coupled with TAMRA-succinimide ester before cleavage from the resin. The peptides were deprotected and cleaved from the resin using anhydrous HF, precipitated, dissolved in aqueous acetonitrile and lyophilized. They were purified using reverse phase (C-18) HPLC and analyzed using Electrospray MS. The above self-associating peptides of CI2 were ligated under folding conditions at room temperature, for 30 mins. The product CI2(1-64)T39D/M40C was purified using RP-C18 HPLC and analyzed by ESMS. Both unlabeled and TMR-only labeled proteins were synthesized as described. Cy5 modified with a thiopyridyl-activated disulfide was used to label the protein by disulfide exchange with the cysteine thiol group at position 40. A 5-fold excess of Cy5-activated disulfide was used and the reaction allowed to proceed for 15 - 20 hours. The labeled protein was purified using RP-C18 HPLC. It was analyzed using ESMS, showing a single species (8383.2 ± 0.5 a.m.u.), consistent with a site-specific 1:1

dye:protein reaction. Both Cy5-only labeled and TMR-Cy5 labeled protein were synthesized in this manner.

2.4.1.2. Protein denaturation studies

One way to study protein folding is to add chemical denaturants that stabilize the denatured state and/or destabilize the native state. As a function of denaturant concentration, the fraction of molecules in the native and denatured states can be monitored. In low denaturant, the folded state has a lower free energy than the denatured state, and thus is more populated. In high denaturant, the unfolded state has lower free energy, and is thus more populated. In between these two extremes, there is a concentration where both states have the same free energy and both states are equally populated. In this way, the stability and number of populated states of a protein can be extracted.

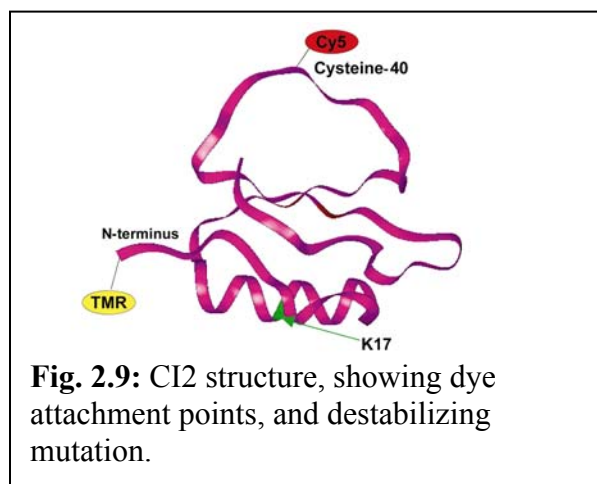
All denaturation experiments were carried out under solution conditions similar to those used by Fersht and coworkers, except that a phosphate buffer (50mM, pH 6.3) was used instead of MES buffer, due to fluorescence background considerations. Pierce guanidinium chloride (Sequal grade) was found to be sufficiently background free for these experiments. Tween-20 was used to passivate the glass surface of the sample cell, in order to minimize protein adsorption. Single-molecule experiments were carried out at a series of denaturant concentrations. Data were usually acquired for 5 minutes, and histograms were calculated and analyzed. Generally, two or three data sets were acquired and analyzed at each denaturant concentration. Ensemble fluorescence denaturation experiments were carried out using a SPEX Fluoromax-2 fluorescence spectrometer (JY/Horiba, NJ). Here, FRET or tryptophan fluorescence data were acquired as a

function of denaturant concentration, and a two-state model was used to calculate the fraction of the folded state as a function of denaturant; plots of these data are shown in Fig. 2.12. Sigmoidal fits to the denaturation curves (single-molecule and ensemble) resulted in the reported midpoints; errors include estimates from multiple experiments.

2.4.2. Results and discussion using ratiometric analysis only

2.4.2.1. Protein system

FRET has been used as a tool to study biomolecule conformations and dynamics at the ensemble level for the last three decades. The strong distance dependence ($1/R^6$) of the FRET rate constant allows the measurement of distances on the 20-



80Å scale, between donor and acceptor labels on a biomolecule. In the case of protein folding, FRET can provide distance information for pairs of points on the amino-acid chain as a function of folding, i.e., it can provide a reaction coordinate that affords a global view of the conformational distributions and dynamics of the protein as it folds. Recently, single-molecule FRET has been used to examine the folding and fluctuations of the surface immobilized peptide, GCN4 [47]. It is clear that surface interactions could have modified and broadened the distributions observed under these immobilized conditions, making the interpretation of the results and comparison to existing ensemble measurements more problematic. RNA folding and protein fluctuations under surface

immobilized conditions, and DNA hairpin folding in diffusion have also been recently reported [33, 44, 49]. In this work, we use diffusion single-pair FRET (sp-FRET) to examine the guanidinium chloride denaturation of freely diffusing chymotrypsin inhibitor 2 (CI2, shown in Fig. 2.9), a well established model for protein folding studies.

The protein CI2 was chosen for several reasons. It has been extensively examined by Fersht and coworkers [82, 83], who provide a large amount of ensemble information with which to compare single-molecule results. This protein has also been the subject of numerous theoretical studies [74-76, 84, 85]. The tertiary structure of CI2 contains the three basic units of protein structure: α -helix, β -sheet and loop elements (Fig. 2.9). Wild-type CI2 is very stable, showing a denaturing transition at about 4M guanidinium chloride, based on changes in tryptophan fluorescence. Kinetic and equilibrium arguments have been used to support a two-state folding mechanism for the protein [86]. The structure of the transition-state and the mechanism of folding have been probed using the protein engineering method [82]. Furthermore, the truncated form of CI2, used by the Fersht group and in this work, is small (64 amino acids), which makes it amenable to total- or semi-synthetic methodologies.

Recently developed conformationally assisted “peptide ligation methodology” using C- α -thioester peptides [78, 87] is a very promising approach for making relatively small proteins, with multiple site-specific mutations, labels or reactive handles, and was used here. Two fragments, CI2(1-39) and CI2(40-64) were synthesized separately by standard solid-phase peptide synthesis; TMR was site-specifically coupled to the N-terminal amine of CI2(1-39), followed by cleavage, deprotection, and purification. The two fragments were then ligated under folding conditions, allowing a clean and rapid

ligation reaction, resulting in wt CI2(1-64) with T39D/M40C and N-terminal TMR substitutions. We refer to this amino-acid sequence as pseudo wild-type CI2. The second dye, Cy5, was coupled to the unique cysteine at position 40, affording site-specifically donor-acceptor labeled protein, with a minimum of purification/separation steps. The product was characterized using HPLC and mass-spectral analysis.

2.4.2.2. Subpopulations of Pseudo wild-type and mutant CI2

A denaturation curve is a plot of the fraction of a given state (e.g. the folded state) as a function of condition (denaturant concentration, temperature, pressure, etc.). For a two-state system, the curve has a sigmoidal shape, and its midpoint corresponds to conditions under which the two states are equally populated; for pseudo wild-type CI2 (versus guanidinium chloride concentration), this midpoint was found to be at 4M by ensemble methods [82, 86]. Using diffusion sp-FRET, we generated histograms of FRET efficiencies (E) for CI2 as a function of guanidinium chloride concentration. Since they report on the inter-dye distance, such histograms represent the distribution of conformational states during folding which can serve as a reaction coordinate for the folding reaction. Fig. 2.10A shows representative histograms for 3, 4 and 6M denaturant; these values were all chosen to be close to the ensemble denaturation midpoint. Based on the ensemble data, most CI2 molecules should be folded, an equal fraction folded and unfolded, and most molecules unfolded respectively under these conditions. Large changes are indeed observed between these three histograms. All histograms showed a peak at around zero FRET efficiency, previously shown to arise in part from molecules containing fluorescent donor and photobleached acceptor [33]. Since these molecules do

not provide relevant FRET (distance) information, only the region above 0.4E is displayed, and the following discussion refers to peaks in this region.

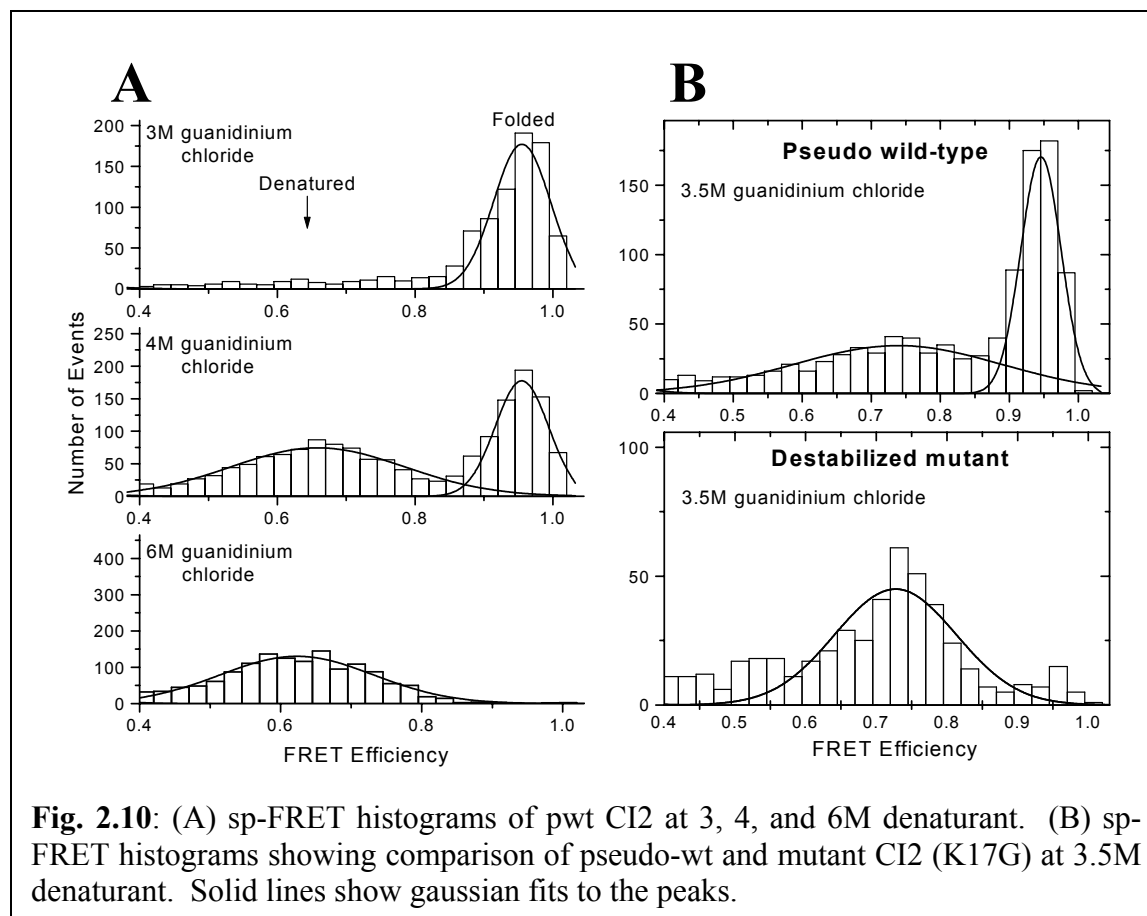


Fig. 2.10: (A) sp-FRET histograms of pwt CI2 at 3, 4, and 6M denaturant. (B) sp-FRET histograms showing comparison of pseudo-wt and mutant CI2 (K17G) at 3.5M denaturant. Solid lines show gaussian fits to the peaks.

CI2 is believed to fold via a two-state mechanism based on ensemble measurements [86]. The sp-FRET histograms directly support such a mechanism. At or below 3M guanidinium chloride, a peak at around 0.95 E is observed. At high denaturant concentration (6M), only a peak at around 0.65 E is detected. As intermediate denaturant concentrations are scanned, varying ratios of the two peaks are observed. The properties of the lower efficiency peak change with denaturant concentration (*vide infra*). The 0.95E and the 0.65E peaks are respectively assigned to the folded and denatured states of the protein. Note that single molecule studies confer the ability to examine particular

sub-populations of interest. This advantage can be appreciated by comparing mean FRET efficiencies obtained from sp-FRET with the ensemble FRET measurements; the ensemble values are found to be significantly lower (by up to 0.2 E). This observation derives, at least in part, from molecules with non-fluorescent or photobleached acceptor. Since the steady-state ensemble numbers include a contribution from the “zero peak”, they are shifted towards lower FRET efficiency, skewing the true values.

The histograms directly confirm the “two-state” nature of the CI2 folding transition. The upper limit for the observation time per molecule in this experiment is about 1 ms due to the diffusion process and the data is acquired with a 0.2 ms integration-time. The observation of two sub-populations indicates that the interconversion of the two forms of the protein must occur on a time scale that is significantly slower than the integration-time. This is consistent with the folding/unfolding kinetics slower than 100ms observed in the transition region by ensemble measurements [86].

A mutant (pwt sequence with K17G substitution) with a significantly lower stability was also synthesized, and its single molecule folding properties were compared to those of the pseudo wild-type. This helix destabilizing mutation (Fig. 2.9) has been shown to shift the guanidinium chloride denaturation midpoint to 2.8M denaturant [82]. Hence, it is expected that at 3.5M denaturant, the observed fraction of the 0.95E subpopulation should be significantly reduced for the mutant relative to wild-type CI2. The sp-FRET histograms (Fig. 2.10B) show that the fraction of the folded form drops from about 0.5 for the wild-type to almost zero for the mutant. Since the solution conditions are identical, this dramatic change must come from protein stability/structure related changes. This observation strongly supports the assignment of the observed sub-

populations to the native and denatured states of CI2. The properties of these sub-populations (mean, width and area of the FRET peaks) contain information about the protein folding reaction, as discussed in the following sections.

2.4.2.3. Inter-dye distances for the native and denatured states

Average inter-dye distances in the folded and denatured forms of the protein can be extracted from the mean FRET efficiencies, assuming freely rotating dyes ($\kappa^2=2/3$) and a Förster radius of $R_0 = 53\text{\AA}$. Since the single-molecule E values exclude non-FRET contributions (*vide infra*), they are used in the discussion below. A value for the mean distance between the two dyes of 31\AA is calculated for the folded form, consistent with a number of about 32\AA estimated from the known crystal structure of the protein [88], and allowing a reasonable additional 7\AA due the size of the dye/tethers, assuming a right-angled geometry on average. For the unfolded form, the mean calculated distance (from mean E , using the same assumptions for κ^2 and R_0) is 48\AA . However, changes in the orientation factor κ^2 could result in significant changes in R_0 and hence skew the calculated value of R (see equation (1)). A discussion is presented below describing estimation of such changes.

In order to compute the effects of κ^2 , it is assumed that the orientations of the donor and acceptor fluorophores are random on the time scale of the measurement ($100\text{ }\mu\text{s}$ to 1ms). This is a reasonable assumption for the denatured sub-population, since it is rapidly interconverting between conformations and the donor and acceptor are separated by a relatively long distance of 40 amino acids [89]. A second assumption is that the large fluctuations of the peptide chain occur on a longer time scale than the fluorescence

lifetime (few ns), allowing the inter-dye distance to be held constant while analyzing the effects of κ^2 .

Ensemble polarization anisotropy (r) measurements were performed on separate proteins labeled with TMR only (N-terminus) and Cy5 only (cysteine 40). It was found that r decreased for TMR (donor) from about 0.09 to 0.07 over a limited range of 3M to 4.5M denaturant, with a much smaller increase by 0.005 to 0.0075 from 4.5M to 6M denaturant. For Cy5 (acceptor), r stayed constant at about 0.2 over this range. The relatively high anisotropy values indicate that either one or both of the following are true: (1) the fluorophores did not have isotropic freedom of motion, or (2) the fluorophores' rotational diffusion was on the same time scale as the fluorescence lifetime.

The first possibility was investigated by extending the work of Dale and Eisinger [39]. An analytical model was developed to describe the fluorophores as rapidly rotating dipoles within an axi-symmetric distribution (a cone), and the cones slowly (compared to donor fluorescence lifetime) and randomly reorienting themselves.

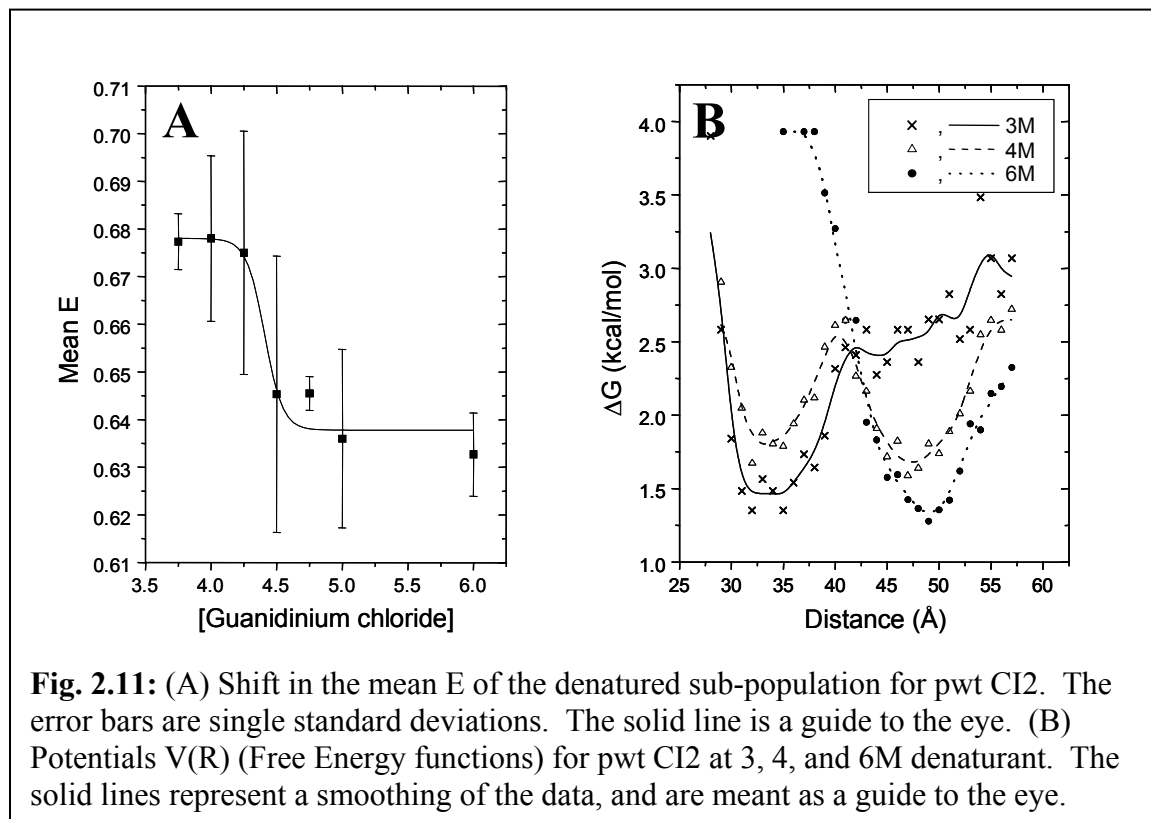
For the second possibility, it was necessary to simulate the rotational diffusion directly. It was assumed that the fluorophores had isotropic freedom, but that the rotational diffusion was slow enough to obtain the observed anisotropy. The simulations were performed by a random walk on a sphere, and were calibrated using the Perrin equation (see appendix 2.A) [40]. In both cases, a decrease in the mean E of 0.03 to 0.05 was found on going from a situation with freely rotating dyes to one with the experimental polarization anisotropy values. Recalculation of the inter-dye distance for the denatured sub-population which included this correction gave $R = 45\text{\AA}$.

The calculated distances for the denatured state compare reasonably with theoretical predictions of Miller and Goebel, who determined an r.m.s. distance of about 50Å for the end-to-end distance of a 40 amino-acid random coil, based on Rotational Isomeric State model calculations [90]. However, fast distance fluctuations between the donor and acceptor (on the time-scale of the donor fluorescence lifetime) will result in a higher average observed transfer efficiency (for the same instantaneous distance distribution) and a corresponding lower average distance [65]. Furthermore, other factors such as the particular sequence, dye-protein interactions, the detection efficiency, photobleaching, excluded volume and solvent interactions could also alter the observed FRET efficiencies; some of these factors are discussed in more detail in the following section.

2.4.2.4. Shifts in average FRET efficiency of the denatured state

It is found that the mean FRET efficiency of the denatured sub-population for the pseudo wild-type protein shifts as a function of denaturant concentration, while the corresponding values for the folded sub-population are fairly constant. Fig. 2.11A shows that the denatured *E* peak shifts from 0.68 ± 0.02 in 4M denaturant to 0.63 ± 0.01 in 6M denaturant. Error bars are standard deviations from multiple measurements. Although the precision of the data is poor and an attempt to fit it to a model will be at best questionable, we might be observing a sigmoidal transition in mean *E*. This transition is centered at about 4.4M denaturant, and could indicate an increase in protein dimensions with increase in denaturant concentration. Such a ‘swelling’ of the denatured protein can occur due to a reduction in persistent specific structure or an increase in the “solubility” of the protein random-coil [36, 91-93]. It is noted that this shift occurs over a limited

range of denaturant concentration (4M to 5M), close to the major unfolding transition



region at 4M denaturant (see the denaturation curves in Fig. 2.12 below) and would be at least partly hidden (or convoluted) in any ensemble experiment.

However, it is emphasized that several other factors can contribute to this shift and must be taken into account. Although most of the observed E shift seems to occur within a narrow range of 0.5M in denaturant concentration, an upper bound on changes due to other factors is calculated by comparing results at 4M and 6M denaturant, given the poor precision of the data in Fig. 2.11. Changes in observed E , (going from 4M to 6M denaturant) can be related to non-distance related changes (i.e., R remains constant) as follows:

$$\left[\frac{(1/E_{6M}) - 1}{(1/E_{4M}) - 1} \right] = \frac{(Jn^{-4}\kappa^2\Phi_a)_{4M}}{(Jn^{-4}\kappa^2\Phi_a)_{6M}} \quad (2.12)$$

where J is the overlap integral, n is the refractive index, κ^2 is the orientation factor, and Φ_a is the acceptor fluorescence quantum yield. The photophysical properties of the dyes (donor and acceptor absorption and emission) were measured in ensemble at 4 and 6M denaturant in order to quantify changes in κ^2 , J and ϕ_a , and the refractive index change was obtained from the literature [94]. The small observed increase in r was translated into a change in κ^2 using the approaches discussed in the previous section, resulting in a decrease of 0.003 E units. Combining these numbers, we estimate that the average E should be reduced due to non-distance effects from 0.68 to 0.65 ± 0.04 . It is therefore concluded that together with the relatively large error bars, the non-distance effects could explain the observed shifts and cannot be ruled out.

In addition to photophysical effects, an increase in solvent viscosity with increasing denaturant concentration will lead to an increase in time-scales of the dipoles' rotational diffusion and the structural fluctuations of the denatured, random coil, amino-acid chain. The slowing-down of these fluctuations will result in a decrease in the average E . However, we estimate that the contribution of increased viscosity to the observed changes in E is small. Viscosity changes with denaturant concentration will continue above 5M, while the observed E change occurs over a very narrow (4M to 5M) concentration range (the E change going from 4M to 5M is 0.06 while it is <0.01 going from 5M to 6M).

2.4.2.5. Distance distributions, widths, and potential functions

sp-FRET histograms give direct access to the E distribution width, thereby providing information on distributions of inter-dye distances. Distance-related broadening of the FRET peaks could occur due to relatively slow (compared to the binning time-scale) interconversion between conformers in the denatured state, especially at lower concentrations of denaturant, and proline isomerization might also play a significant role. However, the distributions are contaminated by several other factors, most significantly shot-noise, and one must exercise great caution in interpreting the width of the FRET distribution.

For the sake of the following discussion, we ignore these complications and assume contributions from distance only (admittedly, a gross assumption). Under such an assumption, the E histograms can be directly translated into potential functions versus inter-dye distance. This is done by firstly converting E distributions into distance distributions assuming $\kappa^2=2/3$ ($R_0 = 53\text{\AA}$). The distance distribution is then converted into a potential energy (free energy) function (Fig. 2.11B) using the Boltzmann weight $P_i=\exp(-\Delta G/RT)$, [47] where P_i is the probability of populating bin i at distance R_i , obtained from the distance histogram. The main features to be noted are changes in the position and number of minima as a function of guanidinium chloride; the appearance of the double well at 4M guanidinium chloride reflects the two-state folding of this protein. Since non-distance factors cause broadening in the histograms, the depicted potential functions show upper limits for the widths and lower limits for the depths of the wells. This is consistent with the measured activation barrier of about 19.5 kcal/mol for folding/unfolding of wt CI2 at 4M denaturant [95]. Note that the minimum for the

denatured state represents a significant entropic contribution. Furthermore, the limited time resolution (200 μ s) prohibits the observation of transiently populated states such as rapidly interconverting conformations of the denatured state, under these conditions.

Shot-noise dominates the distribution width and therefore the obtainable sub-population resolving power [33, 58]. A limited number of photon counts (up to about 100) are obtained from each molecule as it passes through the detection volume. These counts are usually distributed among 3 – 5 time bins (in this paper, all photon counting data were binned to 200 μ s, with a rejection threshold of 30 counts per bin). For a sample with static heterogeneity (disorder), a reduction in shot-noise broadening could be achieved by respective binning of all donor and acceptor photons collected from each molecule (burst integrated analysis) [96]. However, using a detailed comparison between point-wise (200 μ s bins) time analysis and burst integrated analysis for various threshold values, we find that 200 μ s time bins provided the best peak separation. Burst integrated analysis was able to match this performance, but did not exceed it, due to photobleaching considerations. Furthermore, shot-noise broadening places a limit of 10-50 μ s on the time-resolution achievable for identifying interconverting conformations by sp-FRET histograms, using the current dye-pair.

It is relevant to consider here the implications of the ergodic hypothesis, which equates the long-time average behavior of a single molecule with that of the instantaneous average over an ensemble. This is true only if the population of molecules is homogeneous on the single-molecule averaging time-scale, which has important consequences for measurements with limited sampling, as is typical for single-molecule measurements. If a molecule does not adequately sample all of its conformational space

within the measurement time (for example, due to photobleaching), it will be more representative to rapidly acquire small amounts of data on many single molecules (diffusion or flow methods) rather than to collect a larger amount of data on a small number of molecules. In this respect, the diffusion sp-FRET method offers important information complementary to that obtained from FRET time trajectories acquired on single immobilized molecules.

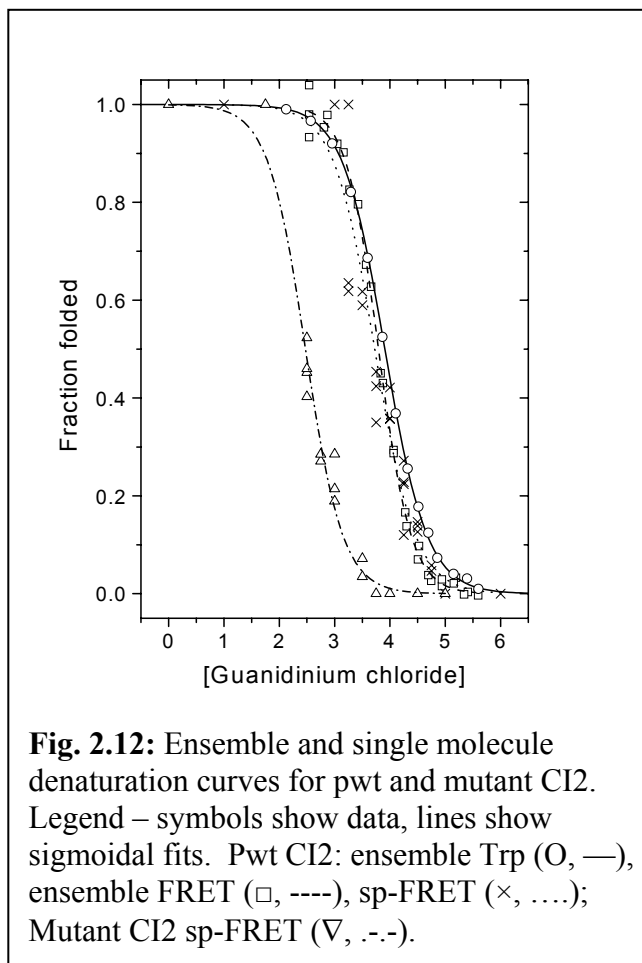
2.4.2.6. Denaturation curves extracted from FRET distributions

Fig. 2.12 shows a comparison of denaturation curves from ensemble and single-molecule experiments for pseudo wild-type CI2, showing the cooperative, two-state folding/unfolding transitions. The single-molecule denaturation curves were directly extracted from the sp-FRET histograms. Here, in marked contrast to the procedure used in ensemble measurements, the fraction of the protein in the folded form was directly calculated as the ratio of the area of the 0.95 *E* peak to the sum of the areas of the 0.95 and the 0.65 *E* peaks; a transition midpoint of 3.7 ± 0.1 M denaturant is observed for the pseudo wild-type protein. This is in good agreement with our ensemble FRET measurements on the donor-acceptor labeled protein (midpoint = 3.8 ± 0.2 M denaturant) and ensemble denaturation using tryptophan (Trp) fluorescence for the unlabeled protein (midpoint = 3.9 ± 0.2 M denaturant). The ensemble midpoint from the tryptophan fluorescence experiments of Fersht for wild-type CI2 is 4.0 M denaturant [82].

Although, the midpoints for the dye labeled and unlabeled protein are within experimental error of each other, there might be a small decrease in protein stability due to attachment of the dyes. Several other factors could affect the position of the single-molecule midpoint, such as different photophysics, photochemistry or diffusion time

between the two forms of the protein. However, the present analysis results in numbers that are in good agreement with ensemble data, showing that the single-molecule method is reliable, and that dye attachment has not seriously compromised protein stability. Fig. 2.12 shows a comparison of the single-molecule denaturation curve for the pseudo wild-type and K17G mutant protein, clearly showing the destabilizing effect of the mutation. The mutant yields a midpoint of 2.5M denaturant, again comparing reasonably well with the ensemble FRET value of 2.65M and ensemble Trp value (2.95M, unlabeled) measured here, and the literature Trp value of 2.8M for CI2 K17G [82].

In equilibrium ensemble experiments, direct information on the fraction of the protein in a particular state is not available since only average properties are measured. Instead, a model and extrapolation dependent analysis must be used to calculate such fractions. This analysis can sometimes be problematic. For example, changes in the value of the observable for a given state as a function of condition (e.g., the shifts in *E* peak position v/s denaturant



observed in this work) are often corrected for by extrapolating from conditions where

only ‘one state’ exists. Non-trivial changes in the observable, especially in the transition region, can produce significant question marks in interpretation, as pointed out by Dill and Shortle [36]. Since single-molecule methods can directly follow changes in sub-populations (individual states or ensembles), a more accurate representation of the process is obtained. Evidently, the effects discussed here will be much more pronounced in situations where a large non-linear change in a property is observed, or when the folding mechanism is complex, involving additional steps.

2.4.2.7. Conclusions – single-molecule ratiometric studies of CI2

We have described the use of diffusion ratiometric sp-FRET methodology to the study of protein unfolding at single molecule resolution. Analysis of the folded and unfolded sub-populations of CI2 during guanidinium chloride denaturation provides the first single-molecule denaturation curves for a single-domain protein, and changes in protein stability due to mutation are observed using this methodology. Comparison of the single-molecule denaturation curves with those from bulk measurements shows that the sp-FRET method is reliable for studying protein folding. In short, this work validates the diffusion sp-FRET methodology as a valuable tool in such studies. Such a validation opens up possibilities for future studies on novel and more complex systems, paving the way for exploration and discovery of new folding phenomena by single molecule spectroscopy.

Improvements in dye-pairs, single-molecule data acquisition, data analysis and surface/gel immobilization methods will be crucial to fully exploit this technique. Issues such as the influence of dyes on the folding reaction and the contribution of dye photophysics to the observed FRET changes must also be addressed in detail.

Immobilization of molecules can afford long time-trajectories and more detailed information, especially under non-equilibrium conditions. However, such immobilization will generally change the static and dynamic distributions of molecular conformations due to variations in the protein energy landscape induced by the local environment. The diffusion methodology presented here can be used to generate benchmark single-molecule data and characterize the unperturbed folding potentials, which will be crucial for comparison during the optimization of surface chemistries and immobilization methods.

Since multiple factors (protein structure, solvent viscosity, dye solvation, etc.) contribute to changes in dye and FRET properties, it is important to deconvolute the variations in these properties for a particular sub-population (denatured state in this work) of protein molecules. Control experiments should ideally be carried out at single molecule resolution, on individual sub-populations of molecules. Further, simultaneous intensity, lifetime and polarization anisotropy measurements will help to identify, quantify and separate-out contributions from κ^2 and from dynamic distance fluctuations. Here, the development of a detection system with four time-correlated single-photon counting Avalanche photodiodes, auto- and cross-correlation methods, and the observation of long time-trajectories of single immobilized molecules will be essential in future work to further clarify these complicated issues.

2.4.3. Current work - CI2 using lifetime, Burst and fluctuation analysis methods

After validating the single molecule FRET method for use in protein folding, more interesting questions can be asked using single molecule methods. Some of these questions are posed in this section. The two universal features of all protein folding

reactions are (i) the collapse of the polypeptide chain from its expanded denatured structure to a more compact structure, and (ii) the formation of the specific native (secondary or tertiary) structure. These features are referred to respectively as “polypeptide collapse” and “specific structure formation”. The polypeptide collapse is an example of a general feature of polymer chains in solvents that favor phase separation of the polymer from the solvent over polymer solvation (“poor” solvents), and is expected to be in the sub-millisecond time scale. Tertiary structure formation typically occurs at longer time scales, but secondary structure can form at similar time scales to the polypeptide collapse. In this context, we are addressing several key questions concerning the folding mechanism of simple folding units or “foldons”:

- (i) what are the general protein structural features, (amino acid sequence, topology) that govern the kinetics of a fast polypeptide collapse?
- (ii) how do solvent friction and nanosecond timescale fluctuations affect these kinetics?
- (iii) do the collapse and secondary native structure formation occur sequentially, or are they coupled to each other?
- (iv) what structural and environmental features contribute to this coupling?

We have been pursuing the question of whether the fast collapse intermediate detected in several proteins is a general feature in protein folding. There has not been an intermediate detected in Chymotrypsin Inhibitor 2, but we had previously measured a possible contraction of the unfolded state upon lowering the denaturant concentration, which may be related to a collapse of the polypeptide chain.

2.4.3.1. Development of single-molecule methods for observation of fast events in protein folding

Fast events in protein folding are attributed to the non-specific collapse of the polypeptide chain or to the formation of secondary structure. Any such changes into more compact unfolded or partially folded states should be found both in kinetic experiments (through intermediates formed at short time scales) and in equilibrium experiments (through detection of additional subpopulations or changes in the unfolded state). To facilitate the detection of fast events in protein folding, we have extended our single-pair Fluorescence Resonance Energy Transfer (spFRET) method for equilibrium diffusion studies to include fluorescence lifetime and polarization information. Four detection channels are used, with the fluorescence emission split into donor and acceptor spectral regions as well as parallel and perpendicular polarizations. We use time-correlated single photon counting (TCSPC) to obtain fluorescence lifetime information, which provides a second, robust measurement of FRET efficiency (which is related to the distance between the donor and the acceptor), improving our ability to separate, identify, and investigate subpopulations. As mentioned previously, TCSPC also permits the observation of dynamic disorder of an individual subpopulation, manifested as a multi-exponential donor lifetime. The multi-exponential lifetime of the donor can be used to extract distance distributions that change on the 1ns-100 μ s time-scales. Measurement of the emission polarization allows us to provide limits on κ^2 for each subpopulation in solution, giving a more robust estimate of distances using FRET.

Upon sifting photon bursts from the data, the next task is to calculate the various quantities of interest from these bursts. Simple statistics include the number of photons

in each detector channel and the duration of the burst. E can be calculated from the intensity of the donor channel I_D and acceptor channel I_A , the background levels, and the factor γ (which corrects for differences in quantum yield and detection efficiency): $E = 1/(1 + \gamma I_D/I_A)$. TCSPC allows an independent estimation of E from the change in donor lifetime. In the absence of the acceptor, the donor has an intrinsic lifetime τ_D . When present, the acceptor quenches the fluorescence of the donor, thus reducing the lifetime to τ'_D . The FRET efficiency E can be calculated from Eq. (2.5), $E = 1 - \tau'_D/\tau_D$. The fluorescence-lifetime method of calculating E is advantageous because it does not suffer from uncertainty in the factor γ used in the expression for intensity

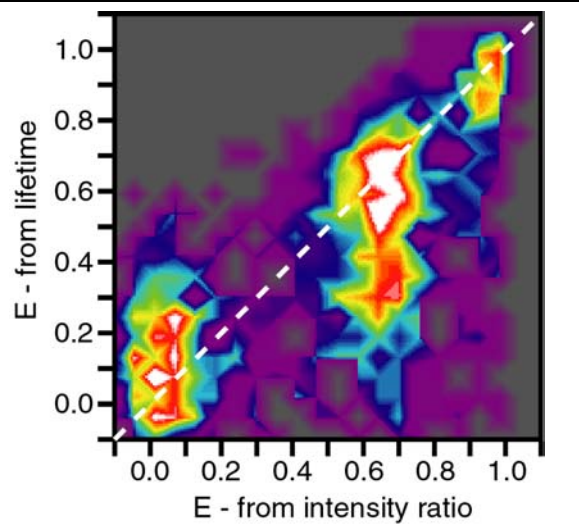
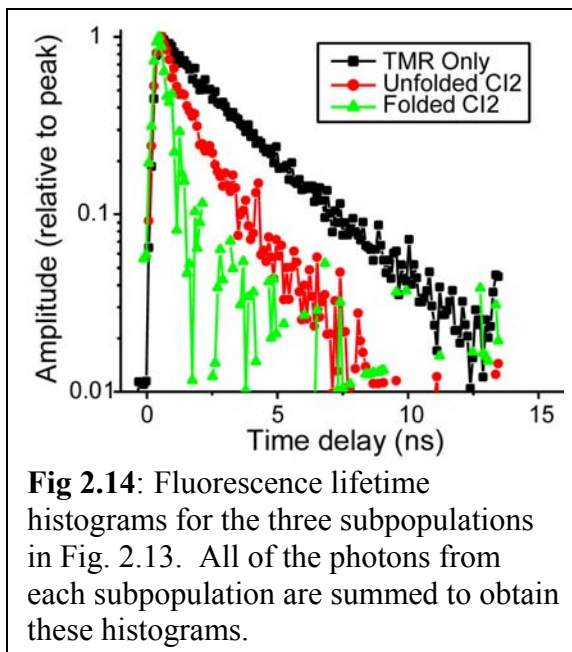


Fig. 2.13: Two-dimensional histogram of photon bursts detected from single molecules of the protein CI2 in 4M GuHCl (near the midpoint of the denaturation curve).

measurements. Fig. 2.13 shows a two-dimensional histogram showing the determination of E using both calculations simultaneously in a single sample of TMR- and Cy5-labeled CI2 near the midpoint of GuHCl denaturation (4M). Three species are present: the folded molecules are on the upper right, the unfolded molecules are in the middle, and the molecules with photobleached Cy5 are on the lower left. In order to have the E values from both methods match, the factor γ was set to 1.2 (This is different from the value used in earlier studies due to changes in the bandpass filters used). Such a histogram has a better resolving power compared with the 1D histogram.

If a fast initial collapse exists for CI2 or any other protein, then most likely there is a change in the distance distribution of the unfolded proteins when going from high denaturant to low denaturant. This makes another benefit of using TCSPC perhaps even more interesting than the increased subpopulation resolution. As described in section 2.3.4, fluorescence lifetime data on FRET systems can be analyzed to investigate distance distributions as manifested by multi-exponential decays; if the distance between donor and acceptor changes on a time scale longer than the intrinsic lifetime of the donor τ_D , then many different values for the donor lifetime in the presence of the acceptor τ'_D are found, producing multi-exponential fluorescence decays. If these distance changes occur on a time scale longer than the diffusion time across the detection volume, then these subpopulations can be separated by looking at the FRET efficiency E of the photon bursts (see for example Fig. 2.13, which separates the folded and unfolded subpopulations of CI2).

At shorter time scales, this is not possible, but the presence of distance distributions can be inferred through detection of multi-exponential fluorescence decays. The number of photons obtained from a single molecule is not sufficient to provide the detection of multi-exponential decays. However, upon separating the fluorescence bursts into subpopulations (for example the



folded and unfolded states of CI2), the photons that come from different subpopulations are also separated. All of the photons of a particular subpopulation can be summed and plotted in a fluorescence lifetime histogram. This capability is demonstrated for CI2 in Fig. 2.14, which shows the fluorescence lifetime histograms obtained for each of the subpopulations found in Fig. 2.13. The lifetime of TMR for the folded molecules (green) is extremely short, indicating high FRET efficiency E . The lifetime of the unfolded molecules (red) is longer, and the lifetime of the TMR only molecules (black) is the known lifetime (3.2 ns).

Fig. 2.15 compares the lifetime histograms for the unfolded subpopulation of CI2 in 4M GuHCl for the emission polarizations parallel and perpendicular to the excitation polarization. Note that the emission is higher at short lifetimes for the parallel polarization, clearly indicating rotational diffusion of TMR on the subnanosecond time scale (multiple exponentials due to distance changes would be the same for both polarizations).

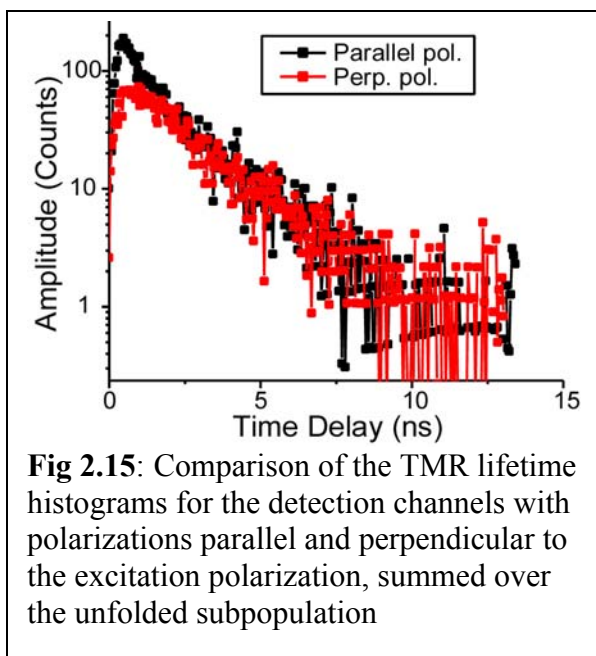
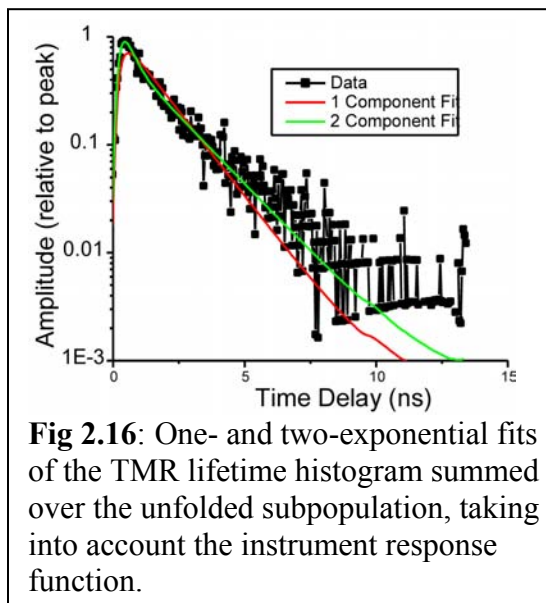


Fig. 2.16 shows a single- and two-exponential fit to the fluorescence lifetime histogram of the unfolded subpopulations in 4 M GuHCl, taking into account the instrument response function. This histogram is clearly not mono-exponential. However, the short component detected is primarily due to rotational diffusion of TMR. Other

exponents due to distance fluctuations are also likely present, but they produce more subtle changes, and need to be verified carefully. A further complication is that the separation into photons from different subpopulations is not perfect. Photons from different sub-populations and background contribute to the signal.

Improved characterization of these contributions can be achieved through an ongoing development of theoretical descriptions. A theoretical description of the spFRET experiment that includes



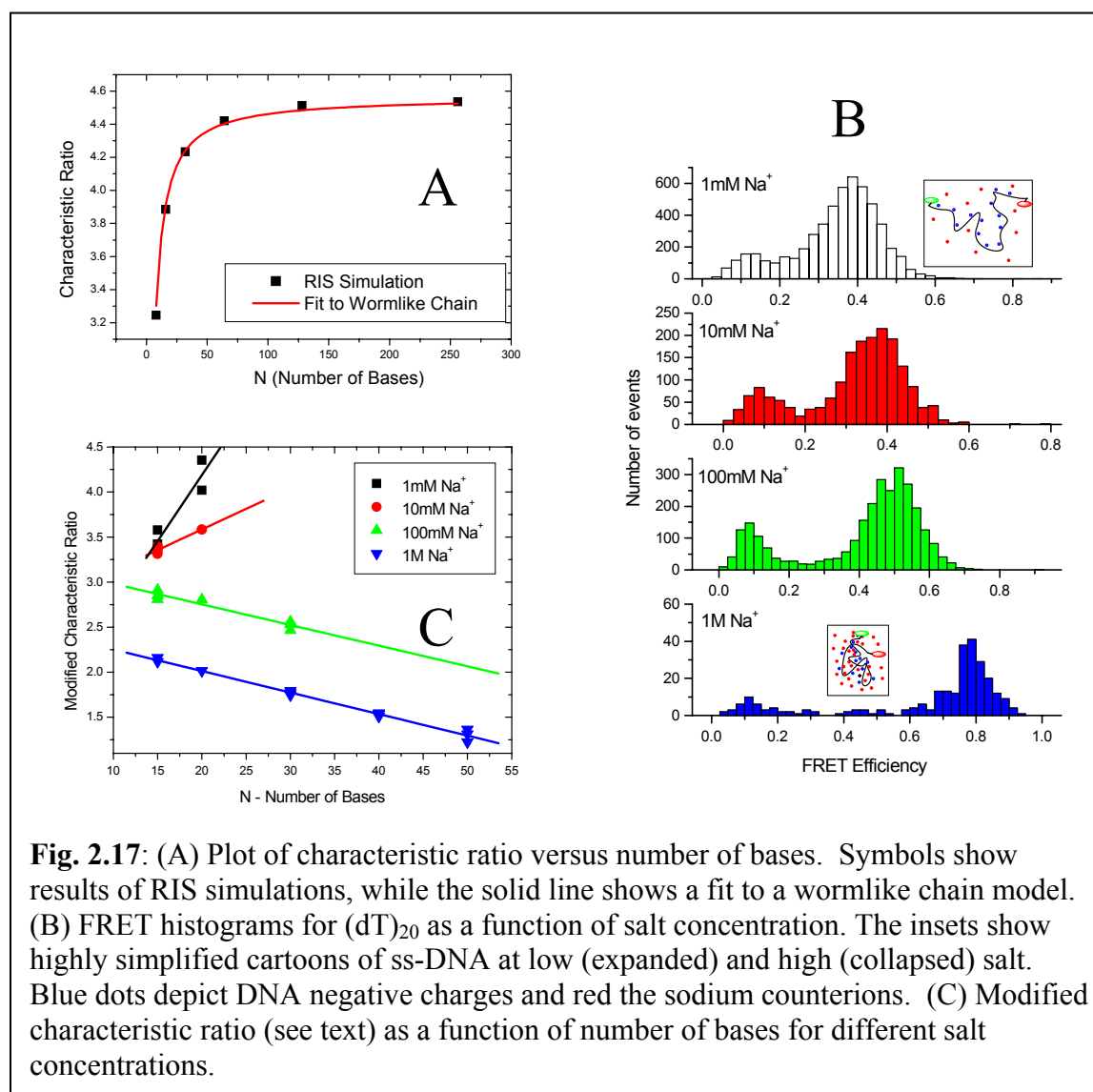
fluorophore photophysics, translational diffusion of molecules in the confocal detection volume, and internal dynamics of the protein is necessary to adequately understand the data resulting from the experiments discussed in the previous section. We are combining photophysical simulations of FRET with Brownian dynamics simulations of translational diffusion and protein chain dynamics. Photophysical simulations of FRET and simulations including translational diffusion have been completed separately. By combining the different components, we will create a tool that will allow us to answer several outstanding questions about the application of spFRET to the protein folding problem.

2.5. Single-stranded DNA as a polymer

Using single-stranded DNA (ssDNA) as a model polymer system, spFRET was used to study polyelectrolyte chain distributions, dynamics, and scaling properties in the short chain regime. There are several outstanding fundamental questions regarding polyelectrolytes in solution, especially due to the complexity resulting from Coulomb interactions [97, 98]. Single-molecule studies on relatively isolated polyelectrolytes could help answer these questions. In order to study scaling issues in this length regime, a series of short poly-dT oligonucleotides ((dT)₁₅, (dT)₂₀, (dT)₃₀, (dT)₄₀, and (dT)₅₀), end labeled with donor and acceptor dyes were synthesized. Poly-dT sequences were chosen to minimize specific interactions between residues in the chain for this first set of experiments, and lengths were chosen by considering isomeric state simulations (RIS) based on the model of Yevich and Olson [99].

Fig 2.17A shows the characteristic ratio for ssDNA as a function of length in bases. The characteristic ratio provides a measure of the polymer stiffness. The points are averages from simulations based on the rotational isomeric model, while the line is a fit of this simulation data to the wormlike chain model. This model assumes a continuum form for the polymer chain, with a certain amount of rigidity. The fit gives a persistence length of 15Å for these idealized conditions, which is within the range of recent experimental estimates [100, 101]. An important point to note here is that although C_n eventually levels out for ssDNA with $N > 100$, it has a strong, non-linear dependence for shorter lengths.

Fig. 2.17B shows E histograms for $(dT)_{20}$ as a function of salt concentration, showing the collapse of the DNA molecule at higher concentrations where electrostatic screening between the DNA backbone negative charges becomes more effective. Fits to the histograms allow the calculation of modified characteristic ratios $\langle R^2 \rangle / N$, which are shown in Fig. 2.17C as a function of length, for several salt concentrations. The downward slope in 100mM and 1M salt means that the size of the ssDNAs increase more slowly than one would expect for a gaussian chain. This could indicate poor solvent



conditions and a collapsed structure for high salt. Several corrections must be included to improve the accuracy of the above results - these issues are under current investigation. Thus, the spFRET method allows measurement of polymer end-to-end distances at low concentrations, which minimizes any intermolecular interaction between strands. Furthermore, it provides a simple test for heterogeneity in the sample due to such aggregation effects. Most interestingly, the lifetime methods described earlier are currently being used to investigate the distance distributions and fluctuations timescales as a function of length scaling and solution conditions in this short-length chain regime. These experiments will be extended to study sequence dependence of these distance and interaction properties, which are of interest in several biological systems [100, 102].

Fluctuations in distance between two sites of a molecule can occur over many time scales. Random polymer chain fluctuations can occur at fast time scales, on the order of 10-100ns (see for example the Rouse and Zimm models in Doi and Edwards [103]). Measurement of these time scales is possible using FRET [65]. By using the Time to

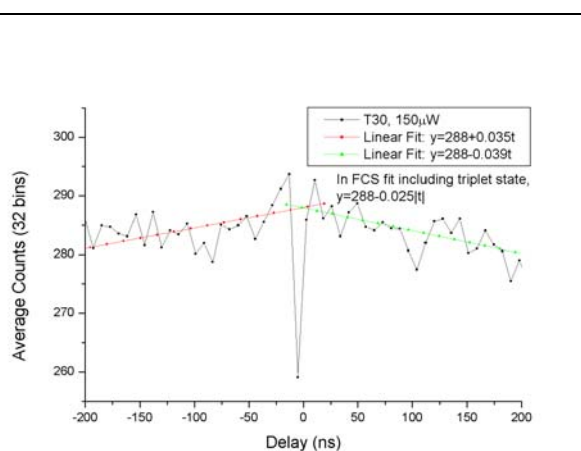


Fig. 2.18: Distribution of time intervals between successive Cy5 photons or TMR- and Cy5- labeled ssDNA, (dT)₃₀. The red and green lines are linear fits to the data, starting a 0 time delay.

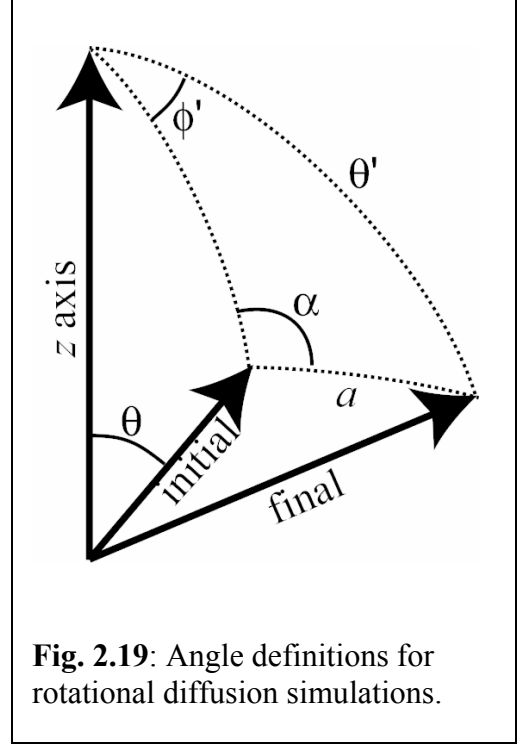
Amplitude Converter described at the end of section 2.2, we measured the time intervals between successive photons from Cy5 in the TMR- and Cy5-labeled ssDNA, (dT)₃₀. Fig. 2.18 shows the resulting autocorrelation function with 5 ns time resolution. The sharp

dip in the center is due to antibunching of the Cy5 photons. Triplet state-induced fluctuations on the μs time scale produce a downward slope on both sides of the peak. The slope depends on the time scale of the triplet states and the fraction of fluorophores that are in the triplet state. Linear fits for each side of time delay 0 ns are performed in order to subtract out this component. From previous fits using FCS over larger time intervals, the measured slope should be 0.025. The measured slopes are slightly higher, 0.035 ± 0.008 and 0.039 ± 0.010 . Fluctuations of the chain may be visible as overshoots of the linear fit on both sides of the antibunching dip, that disappear on the 10 ns time scale. The data are noisy, and verification of this result is needed, but the possibility of monitoring the fluctuation time scales along with the distance distributions using TCSPC (described in previous section) promises to provide valuable information to the protein folding and polymer physics fields.

Appendices

2.A. Simulation of rotational diffusion

In order to simulate rotational diffusion, we use a fixed angular step size a at each time step Δt . Assuming the dipole has an initial orientation $(\theta, \phi = 0)$ with respect to the z axis. For each time step Δt , we assume that the dipole orientation changes by an angle a , with a random direction, specified by the angle α (α is a random number with a uniform distribution from 0 to 2π). These angles are illustrated in Fig. 2.19. Given θ, α , and a , we determine the



new (θ', ϕ') using the law of cosines and sines for spherical angles:

$$\cos \theta' = \cos \theta \cos a + \sin \theta \sin a \cos \alpha, \quad (2.14)$$

$$\cos a = \cos \theta' \cos \theta + \sin \theta' \sin \theta \cos \phi', \quad (2.15)$$

and

$$\frac{\sin \alpha}{\sin \theta'} = \frac{\sin \phi'}{\sin a} \quad (2.16)$$

Rearranging, we get

$$\cos \theta' = \cos \theta \cos a + \sin \theta \sin a \cos \alpha, \quad (2.17)$$

$$\cos \phi' = \frac{\cos a - \cos \theta \cos \theta'}{\sin \theta \sin \theta'} \quad (2.18)$$

and

$$\sin \phi' = \sin \alpha \frac{\sin a}{\sin \theta'} \quad (2.19)$$

There are a few pathological cases. For these cases, we do the following:

$$\text{if } \theta = 0, \text{ set } \theta' = a, \phi' = \alpha \quad (2.20)$$

$$\text{if } \theta = \pi, \text{ set } \theta' = \pi - a, \phi' = -\alpha \quad (2.21)$$

$$\text{if } \theta' = 0, \text{ set } \phi' = 0 \quad (2.22)$$

$$\text{if } \theta' = \pi, \text{ set } \phi' = 0 \quad (2.23)$$

In order to use this rotational diffusion simulation, we need to calibrate it with calculations using the rotational diffusion equation,

$$\frac{\partial P}{\partial t} = -D_{\text{rot}} \nabla_{\text{T}}^2 P \quad (2.24)$$

where D_{rot} is the rotational diffusion constant (units: rad^2/s) and

$\nabla_{\text{T}}^2 = \frac{\partial^2}{\partial \theta^2} + \frac{1}{\tan \theta} \frac{\partial}{\partial \theta} + \frac{1}{\sin^2 \theta} \frac{\partial^2}{\partial \phi^2}$ is the transverse Laplacian operator. This equation

can be solved if we have complete spherical symmetry (a cone is more difficult – the eigenfunctions are harder to compute).

To calibrate the simulation with fixed step size a with respect to the diffusion equation, a functional relationship $D_{\text{rot}} \tau = ka^2$ is assumed. The first term is taken from

the Perrin equation, and is proportional to the rotational correlation time. k is a constant of proportionality to be determined.

Simulations were used to determine k using a fixed angle size $a = 0.57^\circ$, assuming $\tau = 1$ and adjusting the time step to give different values for D_{rot} . At the beginning of each simulation, the initial distribution of the dipole orientations was taken from the distribution $\frac{3}{2}\cos^2\theta$. The anisotropy for each simulation was calculated, and fit to the Perrin equation. The value extracted was $k = 0.29 \pm 0.02$

For FRET, if rotational diffusion is very fast compared to the fluorescence lifetime, $\kappa^2 = 2/3$. When this is not the case, simulations are used to calculate the effects of κ^2 . R'_0 is defined to be the value of R_0 if $\kappa^2 = 2/3$. Then, Eq. (2.1) is written

$$k_{\text{FRET}} = \frac{1}{\tau_D} \frac{\kappa^2}{2/3} \left(\frac{R'_0}{R} \right)^6 \quad (2.25)$$

Then at each time step, the change in orientation is calculated using the simulation described above, and Eq. (2.25) is used to calculate the FRET rate.

3. Monitoring macromolecular interactions using Photon

Arrival-time Interval Distribution (PAID) analysis

3.1. Introduction

3.1.1. Historical overview

With the availability of the complete sequences of genomes of several organisms, it is critical to determine the biological function of the proteins coded by those genomes. Analysis of protein-protein interactions is important for this process since it can produce protein-protein interaction maps that place each protein in its cellular context, from which it is hoped to infer the protein's function. [104, 105]. Several existing methods that monitor protein-protein interactions are: conventional and modified yeast two-hybrid systems along with reconstitution systems, phage display, fluorescence resonance energy transfer (FRET) methods, mass spectrometry, protein chips, and evanescent wave methods [104-108].

Fluorescence correlation spectroscopy (FCS) and related single-molecule methods are important tools for the *in vitro* analysis of macromolecular interactions, and are showing promise for *in vivo* analysis [109, 110]. FCS-related methods can detect these interactions in a distance-independent fashion, unlike FRET. [111]. FCS-related methods detect macromolecular interactions by monitoring fluorescence fluctuations that result when fluorescent molecules diffuse or flow across a tightly focused laser excitation volume (femtoliter confocal detection volume). At concentrations less than 1 nM, the average molecular occupancy of the detection volume is smaller than one, allowing the

detection of photon-bursts generated by single molecules. We call this the “low occupancy” regime. A “photon burst” is the set of all photons detected from a single molecule during its transit through the confocal detection volume. Analysis of these photon-bursts has been used to measure the distribution of molecular properties, such as fluorescence lifetime, polarization anisotropy, and fluorescence resonance energy transfer (FRET) [33, 34, 58, 112]. At concentrations between 1 nM-100 nM, the molecular occupancy is still low enough to be sensitive to the addition or subtraction of one molecule within that volume. We call this the “intermediate occupancy” regime. Although it is not possible to separate the photons into bursts from single molecules, the resulting fluctuating fluorescence signal contains dynamic information about several processes such as translational diffusion [113], rotational diffusion [114], intersystem crossing to triplet states [115], and photobleaching [116]. At concentrations greater than 100 nM, many molecules occupy the detection volume and the fluctuations are averaged out. We call this the “high occupancy” regime. The primary drawback of using FCS-related methods for monitoring macromolecular interactions is the dynamic range over which binding can be detected. These methods are most sensitive in the nM concentration regime, whereas binding constants of protein-protein interactions often correspond to higher concentrations (this limitation is partially offset by the ability of FCS-related methods to detect small subpopulations).

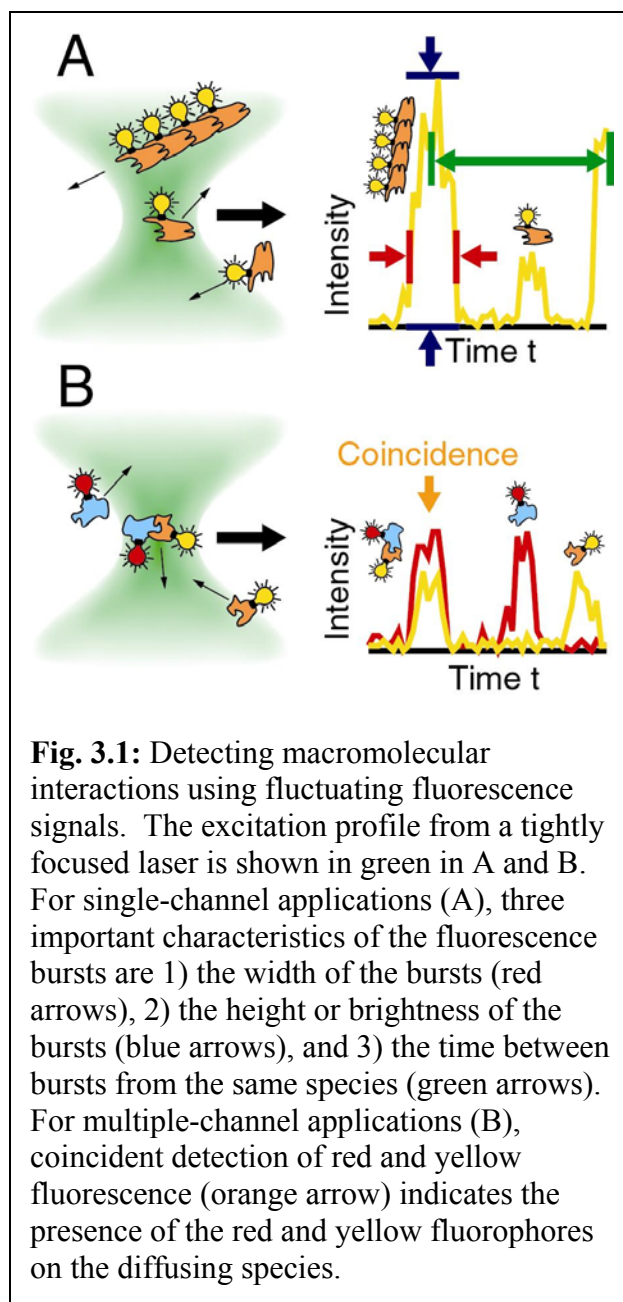
Fluorescence bursts or fluctuations are ideally suited to the study of macromolecular interactions. Fig. 3.1 shows how the properties of the sample translate into features of the fluorescence signal for a detection volume with low occupancy. Macromolecular interactions such as homo-dimerization and aggregation can be

measured using single-channel methods. Fig. 3.1A depicts a single-channel measurement on a sample containing a mixture of monomers carrying one yellow fluorescent label and tetramers carrying four yellow fluorescent labels in solution. The laser excitation profile (*shown in green*) and the detection pinhole define the effective detection volume. As these molecules diffuse in and out of the laser excitation profile, bursts of fluorescence photons are detected, shown as an intensity time trace to the right. The three basic characteristics of a single-channel photon burst are: (1) the brightness of the bursts (*blue arrows*), which is proportional to the number of fluorescence labels detected, (2) the duration of the burst (*red arrows*), which is related to the diffusion time of the molecule across the laser beam, and (3) the time between bursts of the same species (*green arrows*) which is inversely proportional to the concentration of that species. The same characteristics apply for the fluctuation analysis used at higher concentrations (intermediate occupancy). In general, the fluorescence signal from an interacting pair of molecules or an aggregate has different characteristics than that from a free single molecule. The complex or aggregate has a larger hydrodynamic radius, which results in a longer diffusion time. It also has more labels than free molecules, which results in increased brightness of the bursts (fluorescence quenching and incomplete labeling are ignored at this stage). To most effectively detect binding or aggregation, a data analysis scheme that measures all these properties at the same needs to be developed.

For interactions between macromolecules of different types (for example heterodimerization of two proteins), extending the analysis to two channels improves the sensitivity over one channel analysis [111]. The molecules of one type are labeled with one color (eg. yellow), and the molecules of the other type are labeled with another color

(eg. red.) A complex of the two types of molecules has both labels. This is the situation shown to the left of Fig. 3.1B. Signal from the two fluorophores is separated spectrally onto two detector channels, yellow and red. In addition to the ways described for the single-channel case, the binding of two molecules labeled with the yellow and red fluorophores can be indicated by the detection of simultaneous photon bursts on both channels (*orange arrow* in Fig. 3.1B). This coincident detection indicates that both fluorescence labels are present, and thus the two molecules are bound.

3.1.2. Single-channel data reduction and analysis



The task of the data analysis performed on these fluorescence signals is to extract these parameters using all of the information possible, and to present an interpretable graphical representation of the data that summarizes the relevant information in the data set. Several methods summarized below have been developed to perform this task. All of these methods are able to handle vast amounts of data by “reducing” the data to a one-

or multi-dimensional histogram, from which the information on the diffusing species is extracted. The trick is to reduce the data, but not too much. As much information as practically possible should be retained to characterize the sample.

Fluorescence Correlation Spectroscopy (FCS): FCS analyzes fluorescence fluctuations through the use of the correlation function [66, 113, 117]. Correlation functions calculated from the intensity signal reveal the time scale and amplitude of various molecular processes, but do not reveal the brightness of each source. In single-channel applications, macromolecular interactions can be detected by monitoring the change in diffusion time resulting from the interaction of two molecules. However, binding often does not produce a large change in diffusion time: for a sphere, doubling the hydrodynamic volume (for instance by binding two equally sized subunits) produces only a 26% increase in diffusion time (since the diffusion time scales with the hydrodynamic radius, which roughly scales as $[\text{molecular weight}]^{1/3}$). Therefore, a large change in size is required to measure binding using diffusion constants. A further complication is that the shape of the bound molecules is also important; there is no general relationship between diffusion time and the number of subunits. For example, a short, rod-like dsDNA fragment will diffuse more slowly than a globular protein with the same volume (compare the diffusion constant calculations for a sphere with those for a rod in [103]).

Brightness is a reporter of binding events (ignored by FCS) that can in fact be more sensitive than the diffusion time. If two interacting macromolecules are both labeled, the brightness of the interacting complex is double the brightness of the individual subunits, provided that the quantum yield does not change (which is not

always the case.) Brightness has the advantage that the shape of the molecule does not affect it, unlike the diffusion time. Several methods have been developed to use this information.

Moment Analysis of Fluorescence Intensity Distribution (MAFID) and higher order correlation amplitudes: Moments of the photon counting histogram can be used to monitor occupancy and brightness of labeled macromolecules [118, 119]. By comparing the values of the mean (first order moment), the variance (second order moment), and the third order moment, values for the occupancy and brightness of two species can be extracted. In this way, macromolecular interactions can be monitored by taking advantage of the change in molecular brightness when labeled molecules interact. Another method discussed in [120] uses the amplitudes of higher order correlations to extract the occupancy and brightness, but turns out to be equivalent.

Photon Counting Histogram (PCH) and Fluorescence Intensity Distribution Analysis (FIDA): Rather than calculating the moments of the photon counting histogram as described above, it is possible to fit the histogram directly, thereby using more information to extract brightness and occupancy [121, 122]. In this way, sub-populations with different brightness can be separated [123]. The PCH and FIDA methods differ mainly in their treatment of the shape of the detection volume. PCH has been used to monitor ligand-protein binding equilibria [124], to probe the stoichiometry of protein complexes [125], and to study oligonucleotide-polymer interactions [126]. FIDA has been used to probe receptor-ligand interactions in a format compatible with ultra-high throughput screening [127, 128].

The PCH and FIDA methods contain information about the brightness and occupancy of fluorescent species, but lack the information on dynamics contained in the correlation function. For a sample with a single species, it is possible to perform FCS and PCH or FIDA on the same data set to extract both the brightness and diffusion time [129]. However, if there are multiple species, each with a different diffusion time and brightness, there is no direct way to relate each diffusion time found to its corresponding brightness. A method that simultaneously tracks diffusion time and brightness is necessary to address such heterogeneous samples.

Fluorescence Intensity Multiple Distribution Analysis (FIMDA): By using a series of photon count histograms with multiple time bin widths, it is possible to obtain the same temporal information as FCS while gaining the information on brightness [130]. This is because the shape of the photon count histogram is affected by the fluctuations that occur on the time scale of the time bin width. This method is termed Fluorescence Intensity Multiple Distribution Analysis (FIMDA). Macromolecular interactions can be tracked using FIMDA by monitoring brightness and diffusion time simultaneously.

We now review what type of information is available from each method. FCS extracts concentration and diffusion time (and other temporal dynamics), but not brightness. MAFID, PCH, and FIDA extract concentration and brightness, but not diffusion time. FIMDA extracts concentration, brightness, and diffusion time (and other temporal dynamics).

3.1.3. Multiple-channel data reduction and analysis

Coincident detection of two fluorophores of different colors is a more sensitive indicator of binding events than brightness or diffusion time used in single-channel

studies [111]. This is because: (1) coincident bursts are only detected when two molecules are associated, (2) it is less sensitive to quenching of fluorescence, and (3) coincident detection in two channels benefits from the properties of ratiometric measurement. If two interacting molecules are labeled with the same fluorophore, it is necessary to detect distinct subpopulations with a factor of 2 difference in brightness. If they are instead labeled with different-color fluorophores, the experiment is reduced to a simple “yes or no” question. A signal in each channel indicates the presence of the corresponding species. A simultaneous signal in both channels indicates a complex (1:1 ratio between channels), and a signal on only one channel indicates a free molecule (1:0 or 0:1 ratio between channels; random coincidence of signals also needs to be taken into account). The benefit of ratiometric measurement is described in the following. If a fluorescent molecule traverses the *same* path through the detection volume many times (ignoring triplet-state-induced fluctuations), the number of photons detected from the molecule during those traversals would follow a Poisson distribution (appendix 3.C.3), characterized by a mean number of photons (this noise, which is inherent in photon counting experiments, is referred to as “shot noise”). This mean number of photons depends on the path the molecule takes through the detection volume. Taking into account all possible paths through the detection volume, the distribution in photon counts is considerably widened in comparison to shot noise. In contrast, the ratio between the intensity of two channels for an isolated burst is less affected since the mean value of this ratio does not depend on the path taken through the detection volume (the width of the distribution in ratios, however, does depend on the path of the molecule). Measurements using the ratio between two channels (or that consider joint distributions for the two

channels) reduce the noise due to differing paths through the detection volume, and are thus more sensitive [58].

Dual-color cross-correlation FCS: In dual-color cross-correlation FCS, interactions between molecules labeled with two different colors are monitored using the cross-correlation amplitude [30, 111, 131, 132]. Significant correlation amplitudes result only when a diffusing species contributes to both channels. By choosing different-color fluorophores that can be separated into different channels with minimal leakage and characterizing the background, it is possible to read the occupancy of bound molecules directly as the amplitude of the cross-correlation. As with single-channel FCS, the diffusion time of the complex can be extracted. The occupancy and diffusion times of the free components can also be extracted by analyzing the autocorrelation of each channel. However, it is necessary to measure using a different method or to assume values for the relative brightness of the different species in order to extract the occupancies and diffusion times.

Ratiometric single-molecule methods [multi-parameter fluorescence detection (MFD), two-dimensional fluorescence intensity distribution analysis (2D-FIDA), single-pair Fluorescence Resonance Energy Transfer (spFRET)]: Photon burst analysis based on ratiometric methods has been developed for monitoring FRET, polarization anisotropy, and spectral fluctuations [58, 63]. If the distance between two labeled molecules is in the 2-8 nm range, FRET can be used to monitor the interaction. For example, single-pair FRET has been used to monitor the cleavage of DNA by a restriction enzyme in solution [33]. The same ratiometric data analysis can also be applied to macromolecular interactions where the separation between fluorophores is

greater than the 20-80 Å nm range for FRET, although this has not been done. In this case, it is necessary to excite both fluorophores individually and perform coincidence detection.

Multi-parameter fluorescence detection (MFD) and 2D-FIDA perform tasks similar to the ratiometric single-molecule methods, with additional capabilities. MFD has the additional ability to measure fluorescence lifetime [112, 133, 134], and can also be used to obtain the brightness information available with PCH and FIDA [34]. Originally, the single-molecule measurements with fluorescence lifetime were performed with a single detector, although now they have been extended to multiple channels. 2D-FIDA is the extension of the single-channel FIDA method described above to two channels. In extracting the occupancy and brightness in each channel, it takes advantage of both the ratiometric and brightness information. It can be used for samples in the low and intermediate occupancy regimes [135].

We now review what type of information is available from each multiple-channel method. Cross-correlation FCS extracts coincidence, concentration and diffusion time (and other temporal dynamics), but not brightness. MFD can detect coincidence and extract brightness and ratiometric information for multiple channels, and diffusion time. However, it can only work with low occupancy samples. 2D-FIDA can detect coincidence, and extract brightness and ratiometric information for multiple channels. It can work with low and intermediate occupancy samples, but does not extract diffusion time (or other temporal dynamics).

What is lacking in the existing methods is a way to combine the dynamic information available using cross-correlation FCS with the ratiometric and brightness

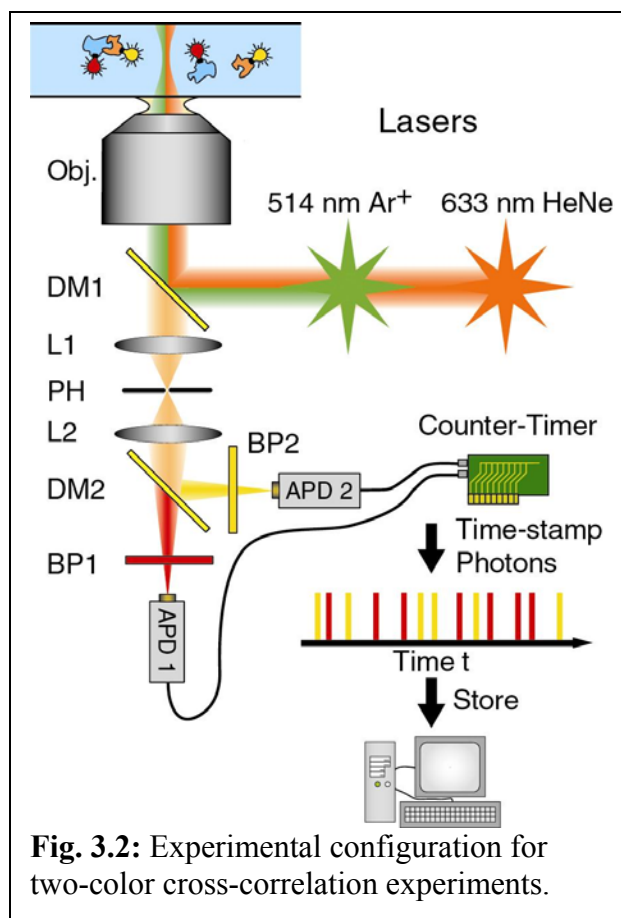
information available with MFD, 2D-FIDA, and ratiometric single-molecule methods, while allowing analysis to be performed at concentrations corresponding to low and intermediate occupancies. Here we introduce a new multi-dimensional data analysis method termed PAID that allows the extraction of information about temporal fluctuations (diffusion), brightness, and coincidence between multiple channels in a unified manner, so that all of the characteristics of each species can be used for identification and for separation from other species. PAID also presents a convenient visual representation of the data useful to the experimenter by focusing on photon-rich regions. We will first describe and develop the Photon Arrival-time Interval Distribution (PAID), which can be used in a single-channel format and a multiple-channel format. Then, we describe the application of PAID to fluorescent species diffusing in solution, detailing how changes in parameters of the species affect PAID. The application of PAID to macromolecular interactions, first in single-channel applications such as aggregation or oligomerization, then in multiple-channel applications such as binding, are described. We give an overview of our model for PAID, which is described more extensively in the appendices. We describe the method used for simulating fluorescent species diffusing through a confocal detection volume, the fitting procedure used for our model, the experimental sample and setup. Finally, we present results of fitting single-channel and two-channel simulations and experiments, demonstrating the potential of PAID for analyzing macromolecular interactions.

3.2. Theory

3.2.1. Development and description of PAID

The data analysis method presented below is motivated by and optimized for the discrete format of the single photon-timing data as acquired by the setup and electronics shown in Fig. 3.2. It depends on treating the signal as a stream of photons rather than an analog signal.

In Fig. 3.2, two laser sources, the 514 nm line from an Ar^+ laser and the 633 nm line from a HeNe laser are introduced into the microscope through a single-mode



optical fiber. The laser lines are reflected using a multiple band dichroic mirror, DM1 (390-510-630 TBDR, Omega optical), and focused into the sample by a high numerical aperture oil immersion objective (NA 1.3 100X Neofluar, Zeiss, Thornwood, New York). The fluorescence from the sample is collected through the same objective, and passes through DM1. The microscope tube lens, L1, then focuses the light onto a 100 μm pinhole, PH. After passing through a second lens, L2, the fluorescence is split by a

second dichroic mirror, DM2 (630DMLP, Omega Optical, Brattleboro, Vermont), into red and yellow channels. The red fluorescence passes through a bandpass filter, BP1 (650LP, Omega Optical, Brattleboro, Vermont), and is detected using the first silicon avalanche photodiode, APD1 (SPCM-AQR-14, PerkinElmer, Vaudreuil, Quebec, Canada). The yellow fluorescence passes through a second bandpass filter, BP2 (580DF60, Omega Optical, Brattleboro, Vermont), and is detected using the second silicon avalanche photodiode, APD2. The APD's emit an electronic pulse for every photon detected. These pulses are timed using a counter-timer board (PCI-6602, National Instruments, Austin, Texas), and stored in the PC.

The single-photon-counting APD detectors shown in Fig. 3.2 emit electronic pulses for every photon detected (dark counts and afterpulses also contribute to the measured signal.) To retain the maximum information about detected photons, electronics are used to time and store the arrival time of each electronic pulse from the photodetectors. This view of the photon stream, where we focus on the arrival times of individual photons rather than counting the number of photon counts within an arbitrary time interval, helps motivate new data analysis schemes, such as PAID, that go beyond those developed for analog signals. The resulting data set is a stream of photon arrival times: t_{Ai} is defined as the arrival time of the i^{th} photon from the detector channel A . The detected photon stream is represented as a sum of Dirac delta functions,

$$I_A(t) = \sum_{i=1}^{N_A} \delta(t - t_{Ai}). \quad (3.1)$$

where N_A is the total number of photons detected in channel A . The use of delta functions allows discrete events to be represented over the continuous variable t . Using

this representation for the photon stream, the number of photons that arrive between times t_{\min} and t_{\max} is written $\mathbf{n} = \int_{t_{\min}}^{t_{\max}} dt I_A(t)$ (this comes from the properties of the Dirac delta function). There are three sources of uncertainty in specifying arrival times of these photons. The first, fundamental uncertainty is from the Heisenberg uncertainty principle, which gives an uncertainty of order $\lambda/c \sim 2$ fs. Because this time scale is much shorter than any other time scale considered, the use of the Dirac delta function to represent the arrival of a photon is justified. The second source of uncertainty is the response time of the photodetectors (300-500 ps). This uncertainty is also negligible here, since it is much shorter than the ~ 100 μ s time scale of the diffusion of molecules across the confocal detection volume and the ~ 1 μ s time scale of triplet state induced fluctuations of fluorophores. For studying dynamics in the 1 – 10 ns time scale (such as fluorescence lifetime and photon antibunching), the APD response time needs to be accounted for. We will extend PAID to include fluorescence lifetime information using time-correlated single photon counting (TCSPC), and the response time of the APDs will then be taken into account. The third source of uncertainty is the resolution of the digital clock ($\Delta t = 12.5$ ns) used to time electronic pulses output by the APDs (shorter than the 1 - 100 μ s time scale). The long term stability of the digital clock used is not critical. We only require that the clock keep a fractional stability of $<1\%$ at all times scales.

The time of arrival t_{Ai} of each photon is recorded as an integer \mathbf{t}_{Ai} with a value $\mathbf{t}_{Ai} = \left\lfloor \frac{t_{Ai}}{\Delta t} \right\rfloor$, where the brackets indicate the greatest integer function (or floor function), which gives the greatest integer less than the quantity inside (eg[3.14]=3).

The arrival time can be recovered to within accuracy Δt by multiplication with the recorded integer $t_{Ai} \approx \mathbf{t}_{Ai} \Delta t$. For an experiment of duration \mathcal{T} , \mathbf{t}_{Ai} will be in the range $0, 1, \dots, \mathcal{T}$, where $\mathcal{T} = \left\lceil \frac{\mathcal{T}}{\Delta t} \right\rceil$. We now convert the expression with the continuous

time variable t in Eq. (3.1) into an expression with discrete time variable $\mathbf{t} = \left\lceil \frac{t}{\Delta t} \right\rceil$. If

N_A photons are detected in channel A , this is written,

$$I_A(\mathbf{t}) = \sum_{i=1}^{N_A} \delta(\mathbf{t}, \mathbf{t}_{Ai}). \quad (3.2)$$

δ is the Kronecker delta function: $\delta(\mathbf{t}, \mathbf{t}_{Ai}) = 1$ if $\mathbf{t} = \mathbf{t}_{Ai}$, and $\delta(\mathbf{t}, \mathbf{t}_{Ai}) = 0$ if $\mathbf{t} \neq \mathbf{t}_{Ai}$.

In FCS, the statistical relationship between a photon stream at one time $I_S(t)$ and another photon stream at a later time $I_T(t + \tau)$ as a function of the time interval τ is measured using the cross-correlation,

$$C_{ST}(\tau) = \frac{\langle I_S(t) I_T(t + \tau) \rangle}{\langle I_S(t) \rangle \langle I_T(t) \rangle} \quad (3.3)$$

If, on average, the photon streams $I_S(t)$ and $I_T(t + \tau)$ increase and decrease together, then $C(\tau) > 1$, and the two streams are “correlated”. If they tend to move in opposite directions, then $0 \leq C(\tau) < 1$, and the two streams are “anti-correlated”. If there is neither relationship between the two streams, then $C(\tau) = 1$, and the two streams are “uncorrelated”. That FCS is insensitive to brightness is most easily seen from the definition of the correlation function in Eq. (3.3); it is scale invariant, so that multiplying the intensity by a factor λ does not change the resulting correlation. If one assumes a stationary stochastic process, the ensemble averages denoted by the angle brackets can be

evaluated as time averages, which are approximated by averages over the discrete time variable \mathbf{t} :

$$\langle \cdots \rangle \rightarrow \lim_{T \rightarrow \infty} \frac{1}{T} \int_0^T dt (\cdots) \approx \lim_{\mathcal{T} \rightarrow \infty} \frac{1}{\mathcal{T}} \sum_{\mathbf{t}=0}^{\mathcal{T}} (\cdots) \quad (3.4)$$

When using the cross-correlation definition in Eq. (3.3) with the discrete expressions for the photon streams in Eq. (3.2), it is necessary to define a discrete time interval $\boldsymbol{\tau} = \left\lfloor \frac{\tau}{\Delta t} \right\rfloor$, analogous to the discrete time variable \mathbf{t} . For the finite experiment of duration \mathcal{T} , the digital estimator for the cross-correlation in Eq. (3.3) is

$$\begin{aligned} \hat{C}_{ST}(\boldsymbol{\tau}) &= \frac{\frac{1}{\mathcal{T}} \sum_{\mathbf{t}=0}^{\mathcal{T}} \sum_{i=1}^{N_S} \delta(\mathbf{t}, \mathbf{t}_{Si}) \sum_{j=1}^{N_T} \delta(\mathbf{t} + \boldsymbol{\tau}, \mathbf{t}_{Tj})}{(N_S/\mathcal{T})(N_T/\mathcal{T})} \\ &= \frac{\mathcal{T} \sum_{i=1}^{N_S} \sum_{j=1}^{N_T} \delta(\boldsymbol{\tau}, \mathbf{t}_{Tj} - \mathbf{t}_{Si})}{N_S N_T} \end{aligned} \quad (3.5)$$

The sum over the discrete time variable \mathbf{t} in the first term is performed to obtain the second term (the caret indicates that $\hat{C}_{ST}(\boldsymbol{\tau})$ is an estimator.) As $\mathcal{T} \rightarrow \infty$ for a stationary process, the estimator converges to the cross-correlation function $\lim_{\mathcal{T} \rightarrow \infty} \hat{C}_{ST}(\boldsymbol{\tau}) = C_{ST}(\boldsymbol{\tau}) \approx C_{ST}(\tau)$. In the above expression, it can be seen that the cross-correlation estimator is formed by comparing the arrival times of each pair of photons \mathbf{t}_{Si} and \mathbf{t}_{Tj} , and adding 1 to a histogram at the bin corresponding to the time interval $\boldsymbol{\tau} = \mathbf{t}_{Tj} - \mathbf{t}_{Si}$. So, the cross-correlation estimator can be viewed as a distribution of *time intervals* between photon arrivals (since swapping the roles of I_S and I_T is

equivalent to changing the sign of the time interval τ , we can, without loss of generality, define this time interval to be non-negative: $\tau \geq 0$). For later convenience, we define I_S to be the “start” photon stream, where all other quantities associated with the start photon stream, such as the start photon arrival times \mathbf{t}_{Si} , we label with a subscript S . We also define I_T to be the “stop” photon stream, where all other quantities associated with the stop photon stream, such as the stop photon arrival times \mathbf{t}_{Tj} , we label with a subscript T . While we keep $I_S(\mathbf{t})$ and $I_T(\mathbf{t})$ formally distinct, we may choose to assign the same photon stream to both so that $I_S(\mathbf{t}) = I_T(\mathbf{t})$. In this case, Eq. (3.5) becomes an autocorrelation.

In order to include the brightness information lacking in the cross-correlation, PAID adds a new photon-counting dimension \mathbf{n} to the cross-correlation estimator of FCS. We count the number of photons \mathbf{n}_{Mij} that arrive between times \mathbf{t}_{Si} and \mathbf{t}_{Tj} in another formally distinct photon stream $I_M(\mathbf{t})$, called the monitor photon stream, with monitor photon arrival times \mathbf{t}_{Mk} (Note: The monitor photon stream is formally distinct from the start and stop photon streams, but depending on the application may be identical to one or both). We obtain the number of photon counts in the time interval delimited by the time of each start photon \mathbf{t}_{Si} and each subsequent stop photon \mathbf{t}_{Tj} for every pair of photons indicated in the summations of Eq. (3.5). By counting photons in each time interval as well as measuring its duration, we spread the cross-correlation estimate over the photon counting dimension \mathbf{n} , providing an additional history of what happens

between the detection of the start and stop photons. The quantity \mathbf{n}_{Mij} is calculated using the following expression,

$$\mathbf{n}_{Mij} = \int_{t_{Si}}^{t_{Tj}} dt I_M(t) \approx \sum_{\mathbf{t}=\mathbf{t}_{Si}+1}^{\mathbf{t}_{Tj}-1} I_M(\mathbf{t}) \quad (3.6)$$

This expression counts the number of photons in $I_M(\mathbf{t})$ that lie between \mathbf{t}_{Si} and \mathbf{t}_{Tj} . Because $I_M(\mathbf{t})$ is a sum of delta functions, \mathbf{n}_{Mij} is strictly an integer. In terms of continuous variables, the PAID function is

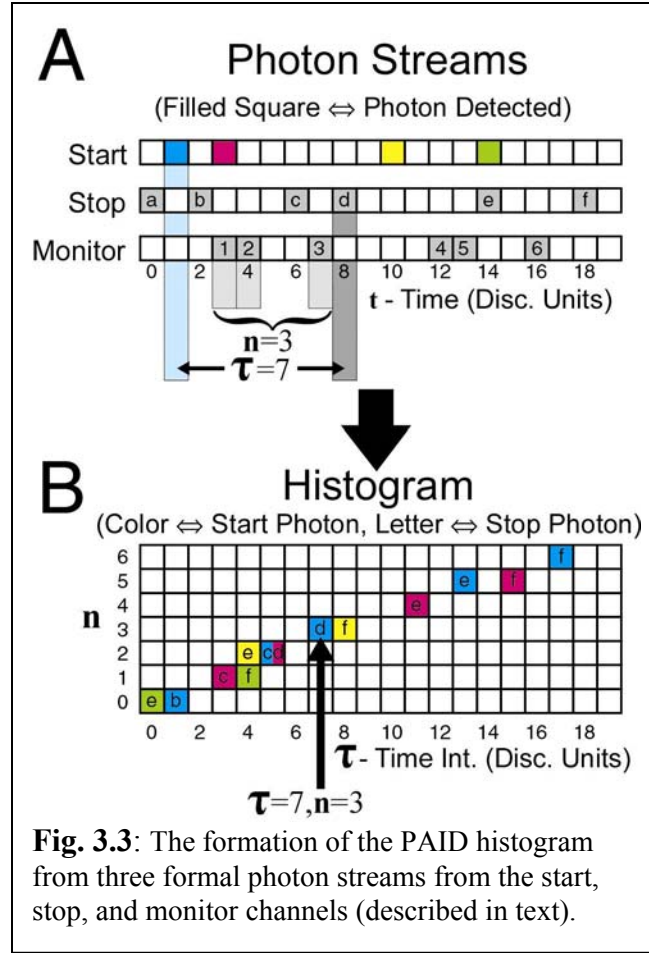
$$C_{STM}(\mathbf{n}|\tau) = \frac{\left\langle I_S(t) I_T(t+\tau) \delta\left(\mathbf{n}, \int_t^{t+\tau} d\theta I_M(\theta)\right) \right\rangle}{\langle I_S(t) \rangle \langle I_T(t) \rangle}. \quad (3.7)$$

The additional factor slices the cross-correlation into strips with different numbers of counted monitor photons. Rather than a photon count probability distribution (approximated by the photon count histogram in PCH and FIDA), the PAID function acts as a photon count distribution of fluorescence correlation. The estimator for the PAID function (using discrete variables for a finite experiment of length \mathcal{T}) is

$$\hat{C}_{STM}(\mathbf{n}|\tau) = \frac{\tau \sum_{i=1}^{N_s} \sum_{j=1}^{N_r} \delta(\tau, \mathbf{t}_{Tj} - \mathbf{t}_{Si}) \delta(\mathbf{n}, \mathbf{n}_{Mij})}{N_S N_T} \quad (3.8)$$

The PAID function $C_{STM}(\mathbf{n}|\tau)$ describes the distribution of count rate in the stop channel over the number \mathbf{n} of intervening photons in the monitor channel within a time interval τ since receiving a start photon. For each pair of photons \mathbf{t}_{Si} and \mathbf{t}_{Tj} , an event is placed in a 2D histogram, where one axis is the time interval $\tau = \mathbf{t}_{Tj} - \mathbf{t}_{Si}$, and the other axis is the number of monitor photons counted $\mathbf{n} = \mathbf{n}_{Mij}$.

Fig. 3.3 shows how a PAID histogram is formed from the start, stop, and monitor photon streams using Eq. (3.8) (See appendices 3.A and 3.B for details). In Fig. 3.3A, there are photon streams from three channels shown, the start, stop, and monitor channels. The time axis is shown in discrete clock units, as measured by the digital counter-timer board in Fig. 3.2. A filled square indicates that a photon was detected at that time position. Each start photon is



identified with a different color, each stop photon with a different letter, and each monitor photon with a different numbers. Each photon in the start channel is paired in turn with each photon in the stop channel that occurs later in time. The time interval between the start and stop photons is one axis in the PAID histogram, shown in 3.3B. The second axis is the number of monitor photons counted in the time interval between the start and stop photons. One example photon pair is shown in the figure: the blue start photon is paired with stop photon “d”. The time interval between these two photons is 7 clock units, and there are 3 monitor photons (numbers 1,2, and 3) between them. The

corresponding entry into the PAID histogram in 3.3B is coded with the cyan background and the letter “d”. Other entries in the histogram are interpreted analogously.

Note that, by summing Eq. (3.8) over \mathbf{n} and comparing to Eq. (3.5), we obtain the following identity,

$$\hat{C}_{ST}(\boldsymbol{\tau}) = \sum_{\mathbf{n}=0}^{\infty} \hat{C}_{STM}(\mathbf{n}|\boldsymbol{\tau}) \quad (3.9)$$

This means that the cross-correlation estimator is the collapse of the PAID estimator $\hat{C}_{STM}(\mathbf{n}|\boldsymbol{\tau})$ onto the time interval $\boldsymbol{\tau}$ axis.

For a single-channel experiment, the same channel constitutes the start, stop, and monitor channels, $[I_S(t) = I_T(t) = I_M(t)]$; the number of photons counted between each pair of photons is $\mathbf{n} = \int_{t_{is}}^{t_{js}} dt I_S(t) = j - i - 1$ for the start photon indexed by i and the stop photon indexed by j . In terms of discrete variables, this special case of the PAID estimator is written for a finite experiment of length \mathcal{T} ,

$$\hat{C}_{SSS}(\mathbf{n}|\boldsymbol{\tau}) = \frac{\mathcal{T} \sum_{i=1}^{N_S} \sum_{j=1}^{N_S} \delta(\boldsymbol{\tau}, \mathbf{t}_{sj} - \mathbf{t}_{si}) \delta(\mathbf{n}, j - i - 1)}{N_S^2} \quad (3.10)$$

This PAID estimator is the series of waiting time distributions to the \mathbf{n}^{th} photon (useful concept for autocorrelations that cannot be extended to cross-correlations). In [34], a similar construction with a single value of \mathbf{n} was used as a criterion in sifting for bursts.

Equation (3.8) can be further extended to include higher order temporal correlations, or more monitor photon streams, by adding factors of the form $\delta(\boldsymbol{\tau}_2, \mathbf{t}_{T_2j} - \mathbf{t}_{S_2i})$ for temporal correlations and factors of the form $\delta(\mathbf{n}_2, \mathbf{n}_{M_2ij})$ for more

monitor photon streams (S_2 , T_2 , and M_2 are additional formal photon streams; \mathbf{n}_2 and τ_2 are additional photon counting and time interval variables).

The photon-counting dimension added to create the PAID estimator allows information on molecular brightness to be extracted in addition to the parameters already available to FCS. By collapsing the PAID histograms onto the time interval axis, one obtains the correlation estimates used in FCS. This allows direct comparison of the results for the PAID histograms to results from FCS. This new method can capitalize on the general familiarity with FCS, while providing information available using PCH or FIDA.

3.2.2. Application of PAID to fluorescent species diffusing in solution

Fluorescence fluctuation experiments determine molecular properties by characterizing the stochastic temporal fluctuations of fluorescence intensity. Fluorescent molecules diffusing freely in solution (avoiding surface-induced perturbations) are excited and detected using a single-molecule epi-fluorescence confocal microscope (see Fig. 3.2). The fluorescence signal is split into spectral regions that match the emission spectra of the fluorophores. For F freely diffusing, fluorescent species in solution, we specify the species by an index with values $\alpha = 1 \dots F$; we associate $\alpha = 0$ with a constant background exhibiting Poisson statistics. The tightly focused laser excitation and pinhole on the detection path used in single-molecule confocal microscopy define the effective detection volume V_{eff} . The z axis is defined as the optical axis of the microscope, and the x and y axes are perpendicular to it. For a Gaussian detection volume, the width of the effective detection volume is ω in the x and y directions, and l in the z direction

(see also appendix 3.C). (Note: non-Gaussian detection volumes are also encountered).

The primary parameters of a diffusing species α that can be extracted from fluorescence fluctuation experiments are:

1. τ_α^D , the diffusion time of a molecule of species α across the effective detection volume. We define the diffusion time to be the time at which the autocorrelation amplitude decays by a factor of 2. For a Gaussian detection volume with $l \gg \omega$, $\tau_\alpha^D = \frac{\omega^2}{4D_\alpha}$, where D_α is the diffusion constant.
2. c_α , the occupancy or average number of molecules of species α in the effective detection volume V_{eff} . The concentration is obtained by dividing the occupancy by the effective detection volume.
3. $q_{\alpha A}$, the brightness or count rate per molecule averaged over the effective detection volume V_{eff} of species α in detector channel A .

To find the average count rate for species α in detector channel A , $k_{\alpha A}$, we use $k_{\alpha A} = c_\alpha q_{\alpha A}$. For the background ($\alpha = 0$), the only parameters are $\{k_{0A}\}$, the count rate in each detector channel A .

Other properties of fluorophores extracted from fluorescence fluctuation experiments are the rate for intersystem crossing to the triplet state, the triplet-state lifetime, the rate for photobleaching, the singlet-state lifetime, and photon antibunching [136]. Fluorescence saturation can also affect the shape of the effective detection volume [137]. As a simplifying first approximation, we have not modeled these effects here, but will in future studies.

We assume that the time between subsequent association or dissociation events is much larger than the diffusion time τ_α^D . This means that if we monitor an equilibrium $A + B \rightleftharpoons AB$, we expect to observe A, B, and AB, but not the association or dissociation events between A and B. This allows us to model the diffusing species as static species, ignoring any fluctuations within the time scale of diffusion across the detection volume. A lower bound on the time between association events can be found from diffusion-limited encounter rates between A and B. If A and B are assumed to be of similar size, the encounter rate $k_{\text{encounter}}$ is approximately $k_{\text{encounter}} = 8RT/3\eta$, where η is the viscosity of the solution, T is the temperature, and R is the molar gas constant. Near room temperature, this is approximately $k_{\text{encounter}} \sim 10^{10} \text{ M}^{-1}\text{s}^{-1}$. This means that if there is a 1 nM concentration of B, the rate at which molecules of species A will encounter molecules of species B is 10 s^{-1} . This gives a time between encounter of 100 ms, which is at least 100 times slower than the diffusion time of the molecules across the detection volume. We also point out that, in order to have a significant population of complexes, the dissociation rate for $AB \rightarrow A + B$ must be similar to or slower than the encounter rate. So, at nanomolar concentrations, we do not expect to observe a significant number of association or dissociation events within the diffusion time of the fluorescent species.

We now describe how the parameters of a diffusing species affect the PAID estimator for a single channel, $C_{\text{SSS}}(\mathbf{n}|\boldsymbol{\tau})$, for a single diffusing species ($\alpha = 1$), a single detector channel ($A = 1$) and background. The parameters describing the system are the occupancy c_1 , brightness per molecule in channel $A = 1$, q_{11} , diffusion time τ_1^D , and background count rate k_{01} . At time interval $\tau = 0$, a photon is received from a fluorescent

diffusing molecule of species $\alpha = 1$. The molecule that emitted the photon is somewhere inside the effective detection volume V_{eff} since the position distribution for emitting molecules matches the detection volume (see appendix 3.C.1). In addition to the molecule that emitted the photon, there are an average of c_1 other molecules of species $\alpha = 1$ inside the effective detection volume (for a total of $c_1 + 1$ molecules at $\tau = 0$); since the molecules are assumed independent and there are a large number of other molecules present inside a solution of comparatively large volume, the presence of one molecule of a species does not affect the probability of another molecule being present. This is equivalent to assuming that the number of molecules present at one time in the effective detection volume follows a Poisson distribution. So, while the molecule that emitted the photon is present (time interval $\tau \ll \tau_1^D$), the average count rate in detector channel A is the average number of molecules present $(1 + c_1)$ multiplied by the brightness per molecule (q_{11}) : $k_{11}(\tau \ll \tau_1^D) = (1 + c_1)q_{11}$. After a time interval $\tau \gg \tau_1^D$, the molecule that emitted the photon has diffused out of the detection volume, and the average count rate returns to the value for an arbitrary time, $k_{11}(\tau \gg \tau_1^D) = c_1q_{11}$.

Fig. 3.4A shows how PAID records this sequence of events for a 30 s simulation with diffusion time $\tau_1^D = 100 \mu\text{s}$, brightness per molecule $q_{11} = 50 \text{ kHz}$, occupancy $c_1 = 0.1$, and no background $k_{01} = 0.0 \text{ kHz}$. There is a peak of high correlation density at small τ , outlined by the white and red contours, that decays with a time interval scale $\tau \sim \tau_1^D$, just as with an autocorrelation used in FCS. This indicates that the molecule that emitted the photon at time interval $\tau = 0$ is still present in the detection

volume. Since the count rate at this time interval is $k_{11}(\tau \ll \tau_1^D) = (1 + c_1)q_{11}$, the peak of high correlation density follows a trajectory in the histogram of the form $\mathbf{n} \sim (1 + c_1)q_{11}\tau$

[$(1 + c_1)q_{11}$ is the slope (vertical offset in log-log plot) of the red ridge]. After the molecule diffuses out of the detection volume, the peak decays in height, indicating that the molecules present are uncorrelated with the initial photon. The count rate is decreased to $k_{11}(\tau \gg \tau_1^D) = c_1q_{11}$, and the correlation density peak follows a trajectory in histogram of the form $\mathbf{n} \sim c_1q_{11}\tau$, which in the log-log plot has the same slope as before but with a lower offset.

Individual parameters influence specific features in the PAID histograms. Figs. 4B-4E show

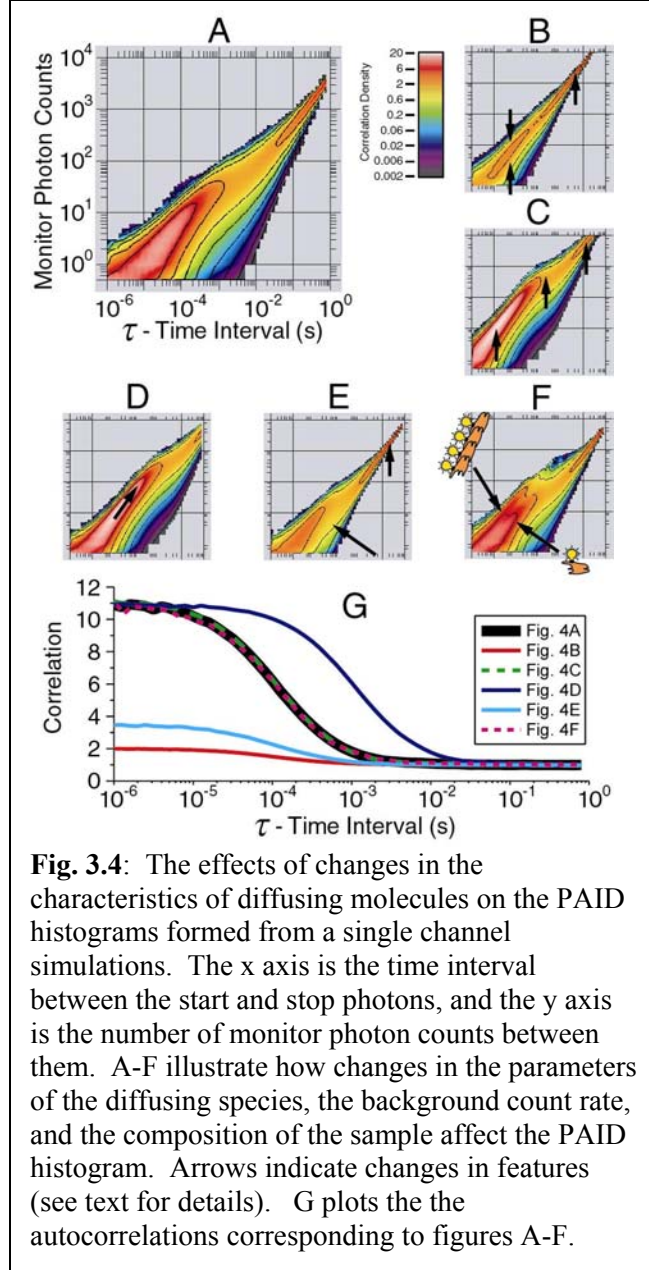


Fig. 3.4: The effects of changes in the characteristics of diffusing molecules on the PAID histograms formed from a single channel simulations. The x axis is the time interval between the start and stop photons, and the y axis is the number of monitor photon counts between them. A-F illustrate how changes in the parameters of the diffusing species, the background count rate, and the composition of the sample affect the PAID histogram. Arrows indicate changes in features (see text for details). G plots the the autocorrelations corresponding to figures A-F.

the effects of changes in the parameters τ_1^D , c_1 , q_{11} , and k_{01} of the diffusing molecules on the PAID histogram. In Fig. 3.4B, the occupancy was increased by a factor of 10 compared to Fig. 3.4A, $c'_1 = 10 \times c_1$. The histogram is narrower in the vertical direction

(shown by *opposing arrows*), the correlation amplitude is lower by a factor of 10, and the long time count rate is higher by a factor of 10 (shown by *arrow* on the upper-right).

In Fig. 3.4C, the brightness is increased by a factor of 10, $q'_{11} = 10 \times q_{11}$, shifting the histogram up in the log-log plot as indicated by the arrows. Also, the histogram is slightly narrower along the monitor photon count axis, since the shot noise decreased with higher photon count values.

In Fig. 3.4D, the diffusion time is increased by a factor of 10 compared to Fig. 3.4A, $\tau_1'^D = 10 \times \tau_1^D$. Notice that the red and white contours are extended by a factor of 10 in time interval, as shown by the arrow.

In Fig. 3.4E, a constant background with rate $k_{01} = 5.0$ kHz is added. The correlation amplitude is decreased since many of the start photons are now uncorrelated background photons, and the background component can be seen as a slower falloff of the histogram to the right of the main correlation peak (shown by the *arrow*). The total count rate is also doubled, which can be seen at long time intervals τ .

In Fig. 3.4F, a second species is added with 4 times the brightness, $q'_{21} = q_{11} \times 4$, an occupancy $c_2 = 0.006$, and diffusion time $\tau_2^D = 100 \mu s$ along with a background component with $k_{01} = 0.765$ kHz. These parameters were chosen so that the correlation curves corresponding to Figs. 4A and 4F would overlap, emphasizing the limitations of FCS.

The advantages of PAID over FCS can be seen in Fig. 3.4G, which shows the autocorrelations for each of the simulations in Figs. 4A-4F. In FCS, the occupancy is extracted from the correlation amplitude, which is $C_{ss}(\tau=0) = 1 + 1/c_1$ for a single

diffusing species with no background. For the simulation for Fig. 3.4A, $c_1 = 0.1$, so the autocorrelation amplitude is $C_{ss}(\tau = 0) = 11.0$ (*black curve* in Fig. 3.4G.) One limitation of FCS is that an increase in occupancy and an increase in the background count rate have the same effect on the correlation curve: both changes decrease the correlation amplitude. Compare the black curve in Fig. 3.4G to the red curve, which is for a 10-fold increase in occupancy ($c'_1 = 10 \times c_1$), and to the cyan curve, which is for the addition of background ($k_{01} = 5$ kHz). In contrast, with PAID, the addition of an uncorrelated background (Fig. 3.4E) and the increase in occupancy (Fig. 3.4B) are distinguishable: an increase in occupancy only narrows the distribution whereas an increase in background adds an additional component at lower count rate. Another limitation of FCS is that a change in molecular brightness does not affect the correlation curve: compare the black curve in Fig. 3.4G with the dashed green curve, for which $q'_{11} = 10 \times q_{11}$. While the two autocorrelation curves overlap, the PAID histograms (Figs. 4A and 4C) are clearly distinguished. Also, the autocorrelation corresponding to the two-component sample of Fig. 3.4F (*magenta line*) is indistinguishable from the autocorrelation corresponding to homogeneous sample of Fig. 3.4A. This indicates that FCS does not have the ability to detect heterogeneity in brightness.

Clearly discernable visual features in histograms often provide the first clues to interesting findings (such as additional subpopulations) or experimental problems. The photon counting histograms used in FIDA/PCH and FIMDA weight all time bins equally. At low occupancy, most of the bins correspond to times when no molecule is present and very few photons are counted. Under these conditions, most of the time bins that contain a large number of photons due to the presence of fluorescent molecules occur at low

probability. In contrast, the PAID histogram focuses on photon-rich regions (as do the cross-correlation estimator and the burst analysis methods such as MFD.) It retains the intuitive nature of the correlation function, while simultaneously providing information available so far only by using the photon counting histogram. Another advantage of PAID is that while single-molecule burst analysis methods can only be applied to samples with low occupancy, PAID can be applied to samples with low and intermediate occupancy, so that it has a larger dynamic range for measuring binding constants.

3.2.3. Application of PAID to the determination of stoichiometry

There are many applications where one wants to study an oligomerizing system. Examples include receptor ion channel oligomerization in the cell membrane [138, 139], and the formation of amyloid plaques associated with neurodegenerative diseases (associated with prions) [17, 18, 140]. As depicted in Fig. 3.1A, monomeric species and complexes or aggregates can be distinguished by differences in their brightness and diffusion time. For a single diffusing species, and no background, one could determine the occupancy and diffusion time using FCS. The molecular brightness could be extracted by dividing the average count rate by the measured occupancy. However, background is always present (although it can be subtracted), and, more importantly, a variety of species are likely to be present in oligomerizing systems. In aggregation processes, there can be a wide distribution of species carrying variable numbers of subunits. Incomplete labeling, quenching of fluorescence, and photobleaching can further result in species with different brightness. Because of these complications, the method used ought to be able to detect heterogeneity in the molecular brightness. The PCH/FIDA methods address this issue. However, because the models for these methods

do not account for diffusion, the time bin size used must be kept significantly shorter than the diffusion time. This prevents the full use of the photon data stream, and does not allow the extraction of the diffusion time (which may be useful for differentiating quenched aggregates from non-quenched monomers). The PAID histogram is ideal for the simultaneous measurement of these properties. The model developed here accounts for diffusion over the entire range of time intervals. The brightness and diffusion time of several sub-populations can be monitored as functions of experimental conditions or time. An example of a PAID histogram for a heterogeneous sample made up of monomers and tetramers is shown in Fig. 3.4F.

3.2.4. Application of PAID to binding

Dual-channel methods provide improved sensitivity over single-channel methods for the detection and characterization of the binding of two different molecules using fluorescence fluctuation methods [111]. As illustrated in Fig. 3.1B, in a dual-color fluorescence binding assay, one molecule A^y is labeled with a fluorophore of one color (for example “yellow”, denoted y), while the second molecule B^r is labeled with a fluorophore of another color (for example “red”, denoted r). Each fluorophore is excited by a distinct laser wavelength. There are three species present in solution: free molecules (A^y and B^r), and complexes (A^yB^r). By extending cross-correlation FCS to PAID, we can use the information on brightness to more accurately distinguish between species and background. In cross-correlation FCS studies, leakage and background can cause difficulty in determining the occupancy of complexes [30]. Although control experiments can be used to extract this background and leakage, it is of greater utility if

one can extract all of these parameters from one data set. Control experiments are then needed only for checking consistency, rather than extracting values to be used in the binding experiment.

Bandpass filters are used to select spectral regions for different channels. The “yellow” and “red” fluorophores y and r have corresponding “yellow” and “red” detection channels, denoted, respectively, Y and R . Because of the vibronic tail of organic fluorophores toward the red end of their emission spectra, there is typically a significant contribution from y into the detection channel R . The contribution from r into the detection channel Y is typically negligible.

We extract information about binding using a series of PAID histograms. For two-channel experiments, there are 8 possible configurations for the PAID histogram (shown in table 3.1): the start, stop, and monitor channels can independently be assigned the yellow or red channel, which gives 8 possibilities. The configuration of the start and stop

Table 3.1: Possible channel assignments for two-channel PAID histogram

Start - S	Stop - T	Monitor - M
Red - R	Red - R	Yellow - Y
Red - R	Red - R	Red - R
Red - R	Yellow - Y	Red - R
Red - R	Yellow - Y	Yellow - Y
Yellow - Y	Red - R	Red - R
Yellow - Y	Red - R	Yellow - Y
Yellow - Y	Yellow - Y	Red - R
Yellow - Y	Yellow - Y	Yellow - Y

channels selects species of interest, which emit photons in both the start and stop channels. The choice of monitor channel determines the fluorophore which will be analyzed in terms of brightness using the PAID histogram.

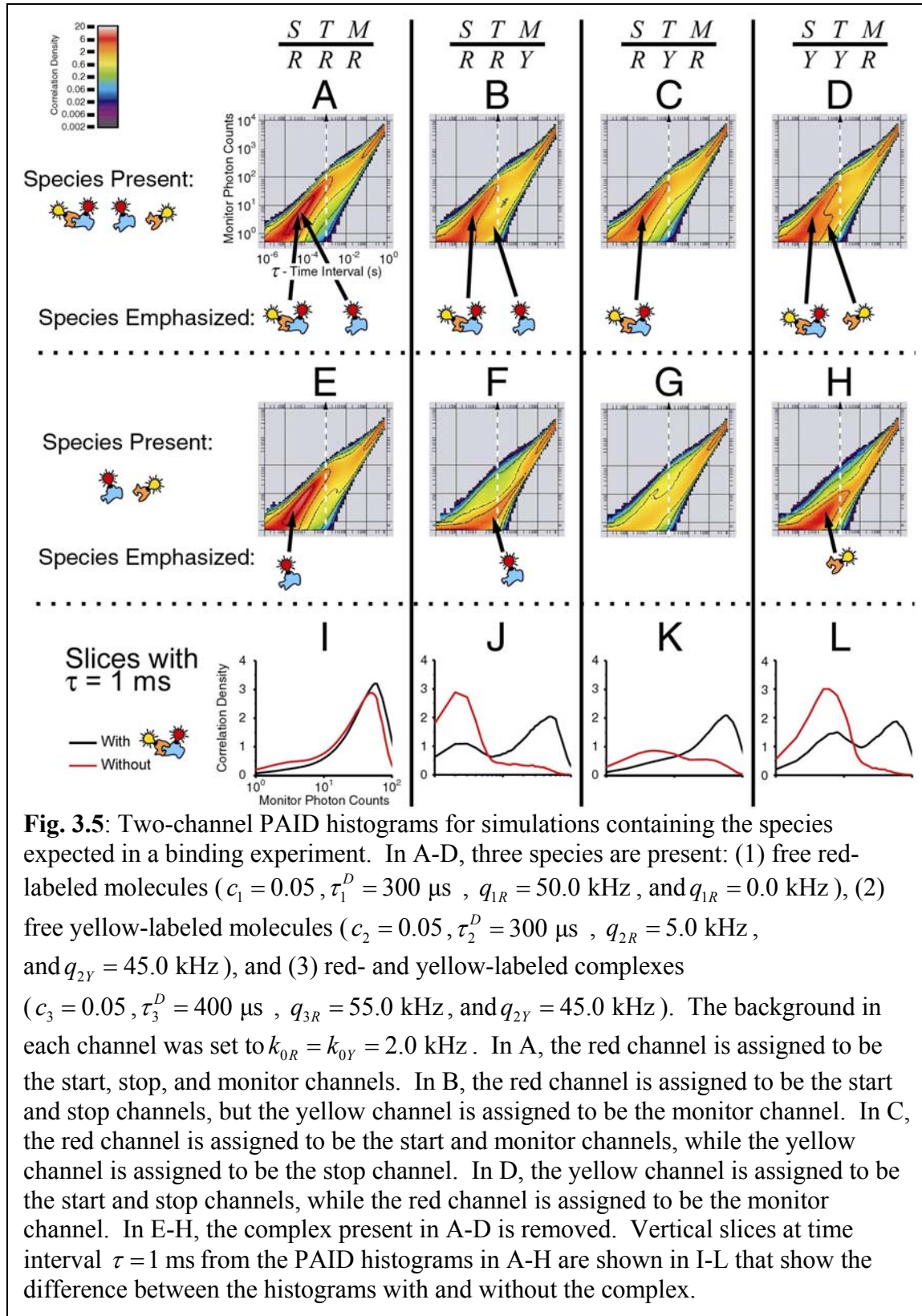


Fig. 3.5 shows PAID histograms for a simulation of a binding experiment. Figs. 3.5A-D show PAID histograms for a two-channel experiment if background, free molecules A^y and B^r , and complexes A^yB^r are present. Figs. 3.5E-H show the PAID histograms if the complexes A^yB^r are absent. The cartoons of the free molecules and complexes indicate which species contribute to any large correlation density peak. Figs. 3.5I-L compares vertical slices at time interval $\tau=1$ ms for the histograms in the presence and absence of A^yB^r .

For the PAID histograms with the red channel assigned as the start channel ($S = R$) and the yellow channel assigned as the stop channel ($T = Y$), time regions where complexes are present are emphasized, since complexes emit photons in both channels whereas the free molecules do not. There are two PAID histograms with $S = R$ and $T = Y$; one assigns the red channel to the monitor channel ($M = R$), and monitors the brightness of r (Fig. 3.5C shows the PAID histogram with A^yB^r present, and Fig. 3.5G shows the PAID histogram with A^yB^r absent.) Note that the correlation density peak in Fig. 3.5C corresponding to the complex is absent in Fig. 3.5G (the small correlation peak present in Fig. 3.5G corresponds to the contribution of y into R). The other PAID histogram with $S = R$ and $T = Y$ assigns the yellow channel to the monitor channel $M = Y$, and monitors the brightness of the yellow fluorophore. There are two more possible histograms, where the assignments of the start and stop channels are swapped ($S = Y$ and $T = R$). The four histograms described so far appear similar to Figs. 3.5C and 3.5G, and so only one example is shown. Together, these four histograms

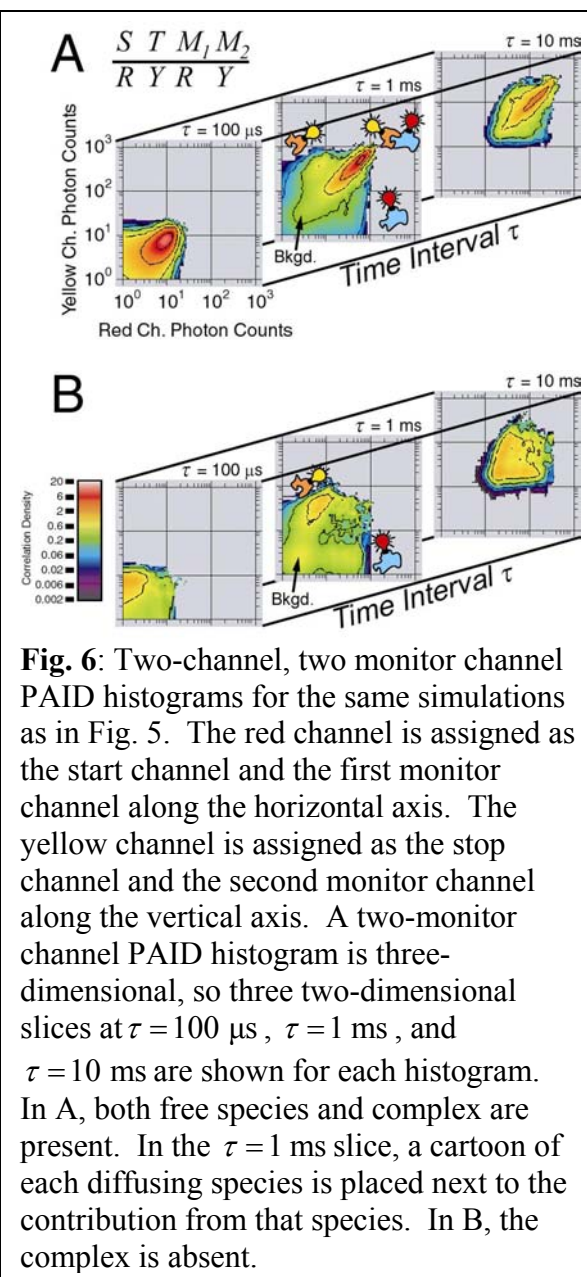
determine the occupancy, diffusion, and brightness in the yellow and red channels of A^yB^r .

The PAID histograms that assign the red channel to the start and stop channels ($S = R$ and $T = R$) emphasize time regions where B^r and A^yB^r are present, since both emit photons in the red channel. For the histogram that assigns the red channel to the monitor channel ($M = R$), the contributions from B^r and A^yB^r overlap since both have a similar brightness in channel R . This is the situation shown in Figs. 5A, 5E, and 5I. There is only one correlation peak visible, where B^r and A^yB^r both contribute. When A^yB^r is absent, in Fig. 3.5E, there is no dramatic change in the histogram. However, for the histogram with the yellow monitor channel, $M = Y$, the contributions from B^r and A^yB^r are well separated since A^yB^r emits in Y whereas B^r does not (see Figs. 3.5B and 3.5J). When A^yB^r is absent, the corresponding correlation density peak is noticeably absent (see Figs. 3.5F and 3.5J). The PAID histograms that assign the yellow channel to the start and stop channels ($S = Y$ and $T = Y$), emphasize A^y and A^yB^r in a similar manner. See Figs. 3.5D and 3.5H for a comparison of the PAID histograms with $S = Y$, $T = Y$, and $M = R$ when A^yB^r is present and absent, respectively.

Although not absolutely necessary for PAID (in contrast to cross-correlation FCS), binding assays are ideally performed by first extracting the properties of the free molecules in experiments where A^y or B^r are present. Only then are the binding experiments performed with both species present. The parameters extracted for A^y and B^r can be fixed if necessary in the fitting of the binding measurement to improve the sensitivity of the method.

By performing a global fit of all eight two-channel PAID histograms, the brightness of the complex in both channels, the diffusion time of the complex, and the occupancy of the complex can all be extracted while obtaining the occupancies, diffusion times, and brightness of the free components.

Higher sensitivity could be achieved if two monitor channels were used for the two-channel experiments, allowing the use of ratiometric information not available with a single monitor channel. Observables in single-molecule diffusion studies that depend on the ratio of two channels are more sensitive than brightness. A PAID histogram with two monitor channels has three axes: the time interval axis τ , the number of photons in the red channel \mathbf{n}_R , and the number of photons counted in the yellow channel \mathbf{n}_Y . Fig. 3.6A shows three slices of this histogram at different time intervals when A^y , B^r , and A^yB^r are present, and Fig. 3.6B shows the



same three slices when A^yB^r is absent. The histograms shown are for the PAID

histogram with the red channel assigned as the start channel ($S = R$), the yellow channel assigned as the stop channel ($T = Y$), and a monitor channel for each channel ($M_1 = R$ and $M_2 = Y$). A cartoon of a particular type of molecule is placed in the $\tau = 1$ ms slice at the approximate location where it contributes. The histograms in Figs. 3.5C and 3.5G are the collapse of Figs. 3.6A and 3.6B, respectively, summing along the yellow monitor channel axis, while keeping the time interval and red monitor channels axes. For an isolated burst, the number of photons counted depends on the diffusion path taken through the detection volume, whereas the ratio between two channels does not. For example, the correlation density peak in Fig. 3.6A at $\tau = 1$ ms corresponding the complex is wider in the direction of the diagonal $\mathbf{n}_R = \mathbf{n}_Y$ than in the perpendicular direction. The one monitor channel PAID histogram is a collapse of the two monitor channel histogram onto the Y or R axis. This collapse smears the central peak; the subpopulations of complex and free molecules are not clearly separated in the one monitor channel case, but are separated with two monitor channels (compare the $\tau = 1$ ms slice in Fig. 3.6A with the corresponding single monitor channel histogram in Fig. 3.5C.) Although the benefits are clear, the fitting model has not yet been extended to account for two monitor channels. The remainder of the paper will use only a single monitor channel.

3.2.5. Model for PAID

Our model for the PAID function is detailed in appendix 3.C. Here we give the general outline and the guiding principles of the model, which is used to fit the data using non-linear least squares method. For this, accuracy and efficiency are the two most

important requirements. Without accuracy, fitted values may be skewed and features in the residuals will not be easily distinguished from features due to subpopulations in a heterogeneous sample. Efficient model calculations are necessary to make a fitting routine practical. Efficiency issues arise more often in models based on numerical methods than those based on analytical formulas due to the increased computational burden.

The assumption that the molecules in solution diffuse independently, with the time between association and dissociation events much longer than the diffusion time, allows the PAID function for all molecules to be expressed as a sum of convolutions of the PAID function for a single molecule with the photon count probability distributions for many molecules (for details see appendices 3.C and 3.G). The expressions for single molecules are approximated by Monte Carlo simulation of possible diffusion paths through the confocal detection volume (similar to [141]). A scaling law is used to model changes in brightness or diffusion time. Depending on the accuracy desired, the confocal detection volume is set as an analytical Gaussian detection volume, as a numerical approximation, or as an experimentally measured detection volume, allowing the direct application of the expected detection volume to the model. Our model is able to account for the possible diffusion paths through that volume, in contrast to either FIDA or FIMDA [122, 130]. There, only the volume density for a given brightness value is required. This indeed simplifies their model, but comes at the expense of not being able to model the possible diffusion paths.

A slight modification of the PAID model allows the calculation of an alternative and more accurate model for FIMDA [130], referred to as “modified FIMDA”. A

comparison of the parameters extracted using PAID, FIMDA, and the modified FIMDA model reveals whether any differences in the accuracy of extracted parameters are caused by the change in the fitting model or the change in the histogram.

To obtain the final expressions for the PAID function through the combination of the single-molecule expressions, it is necessary to compute many convolutions, which produces the primary bottleneck in the model calculation. Because of the wide temporal and dynamic ranges over which fluorescence fluctuations occur, logarithmic axes are desirable. For the most efficient calculation, the convolution method used must work in a logarithmic domain. However, pure Fast Fourier Transform (FFT) methods demand linearly spaced data, which quickly produces huge arrays. A novel method is presented in appendix 3.H that combines the use of the FFT with a quasi-logarithmic scale, making the model calculation practical.

3.3. Materials and methods

3.3.1. Simulation of translational diffusion of molecules, and photon emission and detection

The simulations for translational diffusion of molecules, photon emission and detection were performed as in [142], with modifications. A Gaussian excitation/detection volume with $\omega = 0.35\mu\text{m}$, $l = 1.75\mu\text{m}$ is placed at the center of a three-dimensional simulation box of size $V_{\text{box}} = 3.5 \times 3.5 \times 17.5\mu\text{m}^3$. A Gaussian excitation/detection volume need not be used. In fact, another volume is used for the analysis of the experimental data in section 3.4 (the idealized Gaussian detection volume does not accurately match the detection volume of the actual experimental setup). We use a rough approximation to the detection volume, ignoring vector diffraction and the differences between the excitation and detection profiles for different wavelengths. We calculated using scalar diffraction the expected laser excitation profile when the oil immersion objective is focused $20\mu\text{m}$ inside the aqueous solution. We used random sampling of contributions from plane waves. The use of plane waves for vector diffraction is described in references [143, 144]. The effect of the pinhole in the detection path ($100\mu\text{m}$) was calculated using geometric optics, similar to [145], except that the water-glass dielectric surface is taken into account. The peaks of the excitation profile and detection profile maxima did not overlap in the z direction, so they were translated with respect to each other until they did. Adjustment of the pinhole or the

photodetectors along the emission light path to maximize the signal would produce similar results (we do not adjust the pinhole in our setup, but we do adjust the photodetectors). By multiplying the two profiles, we obtain the detection volume. This volume is used as the basis for calculating the kernels used for fitting the experimental data. The size of the calculated effective detection volume is $3.2 \mu\text{m}^3$. For this volume, a concentration of 1 nM corresponds to an occupancy of 1.9. The diffusion time of a molecule of species α with a diffusion constant D_α through this detection volume, was calculated by simulating many paths through the detection volume: $\tau^D = (2.8 \times 10^{-10} \text{ cm}^2) / D_\alpha$.

A fixed number of molecules is placed inside the simulation box, which has periodic boundary conditions (when a molecule leaves the volume, it comes back through on the opposite side at the same lateral position). Diffusion into and out of the detection volume is simulated by a series of steps, generated at a time scale short enough to ignore the effects of diffusion on the excitation rate of the molecules within this step. We use $\Delta t = 1 \mu\text{s}$, since we choose diffusion times such that $\tau^D \geq 100 \mu\text{s}$. At each time step, the distance step for each dimension (x,y,z) is determined by a pseudorandom number generated with a Gaussian distribution, with mean $\mu = 0$ and standard deviation $\sigma = \sqrt{2D\Delta t}$, where D is the diffusion constant. The diffusion step generation distribution is taken directly from the Green's function for three-dimensional diffusion [Eq. (3.23) in appendix 3.C.2;[146]]. At each diffusion step, a series of pseudo-random numbers is generated with an exponential distribution with a decay rate λ that depends on the excitation rate for the molecule's position (See Eq.(3.17)) until time Δt is passed, thereby generating a series of arrival times for emitted photons. The photons are

assumed to emit immediately upon excitation, although additional photophysics should be taken into account (future studies). Finally, another pseudo-random number is generated to see which if any channel detects the photon. If the photon is detected, the time of arrival and detection channel are saved. The resulting photon sequences can be subjected to any of the possible data reduction and analysis techniques.

3.3.2. Fitting routine

We use the Levenberg-Marquardt nonlinear least squares fitting procedure [147] to extract the parameters from the data, calculating the necessary partial derivatives numerically. The model used is described in detail in appendix 3.C. To estimate the standard deviation of errors, we use ten independent instances of the histogram to calculate an estimate of the statistical errors of each bin. The statistical errors are used as weights in the fitting routine (this method is used for FCS in [142]. If a bin is nonzero in fewer than ten instances, it is excluded from the fit. Without this restriction, we found that only a few points dominate the value for χ^2 (the χ^2 merit function is not ideal for sparsely populated bins in histograms).

3.3.3. Preparation of dsDNA

We used fluorescently-labeled dsDNA fragments as a model system for exploring the capabilities of PAID. Five dsDNA fragments were synthesized: (1) Cy5-dsDNA, (2) dsDNA-Cy3, (3) Cy3-dsDNA, (4) Cy3-dsDNA-Cy3, and (5) Cy5-dsDNA-Cy3. The dsDNA was prepared using standard PCR protocols [148] with one or two of the DNA primers labeled with a fluorophore at their 5' end. The fluorophores used were Cy3 (emits in the “yellow” part of the spectrum) and Cy5 (emits in the “red” part of the

spectrum). We prepared Cy3-dsDNA and Cy3-dsDNA-Cy3 for testing the single-channel applications of PAID, and we prepared Cy5-dsDNA, dsDNA-Cy3, and Cy5-dsDNA-Cy3 for testing two-color applications. For Cy5-dsDNA-Cy3 and Cy3-dsDNA-Cy3, the separation between the two fluorophores is large enough (65 bp, ~ 240 Å) to preclude any FRET between the Cy3 and Cy5 or Cy3 and another Cy3. The experimental data were acquired for 5 minutes on dilute samples (30 pM – 1 nM) of dsDNA fragments in a 20 mM HEPES buffer in the presence of 50 mM NaCl, 5% glycerol, and 1 mM MEA (pH 7.0).

3.3.4. Experimental setup

The experimental setup is similar to the one described in diffusion FRET studies [(see Fig. 3.2) and [33, 58]. Two laser beams (514 nm Ar⁺ excites Cy3 and 633 nm HeNe excites Cy5) are introduced into and coupled out of the optical fiber. For all measurements, we used 200 μ W from the 514 nm laser and 66 μ W from the 633 nm laser. The 514 nm line weakly excites Cy5 ($\sim 3\%$ of maximum), but this effect is overwhelmed by the 633 nm excitation. A triple band dichroic mirror (390-510-630 TBDR, Omega optical, Brattleboro, Vermont) is used to reflect the two laser lines, while transmitting the emissions of Cy3 and Cy5. The laser is focused 20 μ m inside the solution by a 100X 1.3 NA Zeiss Neofluar oil immersion objective. Fluorescence from the excitation volume is split into two detection channels with a dichroic mirror (630 DMLP, Omega Optical, Brattleboro, Vermont), the Cy5 channel (>650 nm), and the Cy3 channel (550 nm-610 nm). Silicon avalanche photodiodes (SPCM-AQR-14, PerkinElmer, Vaudreuil, Quebec, Canada) are used to detect the photons. The electronic pulses resulting from these photons are individually timed by a counter-timer board (PCI-6602, National Instruments, Austin Texas), and stored in a PC.

3.4. Results

3.4.1. Simulations – extracting stoichiometry in a single channel

We generated two series of single-channel, single-species simulations in a Gaussian detection volume to demonstrate the ability of PAID to simultaneously extract occupancy, brightness, and diffusion time and to compare it to FCS, FIDA (PCH is assumed to obtain similar results), and FIMDA. Because the simulations have only one channel, the PAID histogram assigns that channel to be the start, stop, and monitor channels. The first series consists of 10 simulations of 30 s each, with an occupancy $c_1 = 0.1$ (low occupancy), diffusion time $\tau_1^D = 100 \mu\text{s}$, and brightness per molecule $k_{11} = 50 \text{ kHz}$. The second series is the same, except that the 10 simulations are 10 s each, with an occupancy of $c_1 = 1.0$ (intermediate occupancy).

The estimated parameters extracted using each method are shown in table 3.2; the parameters for simulations with low occupancy ($c_1 = 0.1$) are shown at the top, and those for simulations with intermediate occupancy ($c_1 = 1.0$) are shown at the bottom. The first column lists the names of the parameters for the fit, along with χ^2 . The second column lists the parameter values for the simulations. The remaining columns show the sample mean and sample standard deviation of the parameters extracted from 10 fits using the listed methods: PAID, modified FIMDA, FIMDA, FCS, and FIDA. For a sample size N , the error in the sample mean found is a factor of \sqrt{N} smaller than the sample standard deviation listed for each parameter [149]. So for 10 fits, we expect the error in the mean

Table 3.2: Parameters Extracted using PAID, modified FIMDA, FIMDA, FCS, and FIDA for single-channel, single-component simulations in a Gaussian detection volume

Parameters	Simulation	PAID Fit	Modified FIMDA Fit	FIMDA Fit	FCS Fit	FIDA Fit
10 Simulations (30 s each): Low Occupancy ($C_1=0.1$)						
χ^2	-	1.19 ± 0.17	1.13 ± 0.14	4.69 ± 0.64	1.51 ± 0.52	0.63 ± 0.27
k_{01} (kHz)	0.0	0.01 ± 0.01	0.002 ± 0.003	0.005 ± 0.008	N.A.	0.02 ± 0.01
c_1 (mol)	0.1	0.100 ± 0.002	0.099 ± 0.002	0.100 ± 0.002	0.099 ± 0.002	0.105 ± 0.003
τ_1^D (μ s)	100.0	98 ± 2	99 ± 1	99 ± 2	95 ± 2	N.A.
q_{11} (kHz/mol)	50.0	48.9 ± 0.8	49.2 ± 0.9	49.7 ± 0.8	N.A.	47.3 ± 0.7
10 Simulations (10 s each): Intermediate Occupancy ($C_1=1.0$)						
χ^2	-	1.01 ± 0.13	0.80 ± 0.11	1.04 ± 0.21	1.12 ± 0.48	0.66 ± 0.33
k_{01} (kHz)	0.0	0.03 ± 0.03	0.06 ± 0.02	0.13 ± 0.09	N.A.	0.26 ± 0.23
c_1 (mol)	1.0	0.99 ± 0.02	1.00 ± 0.02	0.99 ± 0.02	0.99 ± 0.01	1.05 ± 0.03
τ_1^D (μ s)	100.0	99 ± 2	101 ± 3	94 ± 3	95 ± 1	N.A.
q_{11} (kHz/mol)	50.0	49.5 ± 0.7	48.6 ± 0.5	50.8 ± 0.7	N.A.	47.6 ± 0.6

Parameter values listed as N.A. (not applicable) are not able to be extracted using the listed method.

values quoted to be about a factor of $\sqrt{10} \approx 3$ smaller than the standard deviations quoted.

We generated two additional series of simulations to test the ability of these methods to detect the stoichiometry of multiple subunits in a single-channel experiment. As before, the first series is for low occupancy ($c_1=c_2=0.05$), and the second is for intermediate occupancy ($c_1=c_2=0.5$). The second species has twice the brightness of the first species, plus a 50% longer diffusion time (a convenient value somewhat longer than would be expected for a dimer). Table 3.3 shows the results for the two-component simulations. The structure for table 3.3 is the same as table 3.2, except that there are additional parameters required to account for the second species.

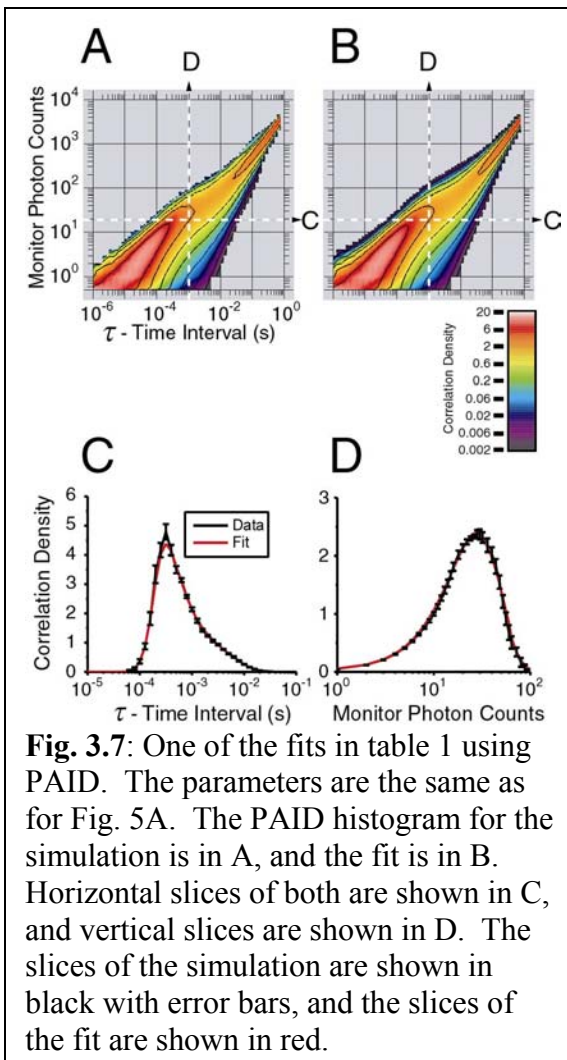
Table 3.3: Parameters Extracted using PAID, modified FIMDA, FIMDA, FCS, and FIDA for single-channel, two-component simulations in a Gaussian detection volume

Parameters	Simulation	PAID Fit	Modified FIMDA Fit	FIMDA Fit	FCS Fit	FIDA Fit
10 Simulations (30 s each): Low Occupancy ($C_1 + C_2 = 0.1$)						
χ^2	-	0.77 ± 0.12	0.75 ± 0.12	1.13 ± 0.93	Did not converge	0.47 ± 0.24
k_{01} (kHz)	2.0	2.00 ± 0.01	2.00 ± 0.01	1.90 ± 0.03		1.99 ± 0.08
C_1 (mol)	0.05	0.048 ± 0.002	0.048 ± 0.002	0.064 ± 0.003		0.059 ± 0.007
τ_1^D (μ s)	100.0	100 ± 7	99 ± 7	117 ± 11		N.A.
q_{11} (kHz/mol)	50.0	49.9 ± 4.1	50.2 ± 4.9	50.7 ± 5.2		48.1 ± 7.5
C_2 (mol)	0.05	0.052 ± 0.003	0.052 ± 0.003	0.042 ± 0.005		0.048 ± 0.009
τ_2^D (μ s)	150.0	145 ± 5	146 ± 5	146 ± 8		N.A.
q_{21} (kHz/mol)	100.0	98.0 ± 3.2	98.4 ± 3.3	105.7 ± 3.0		99.6 ± 5.2
10 Simulations (10 s each): Intermediate Occupancy ($C_1 + C_2 = 1.0$)						
χ^2	-	0.88 ± 0.22	0.58 ± 0.06	0.55 ± 0.06	Did not converge	0.65 ± 0.27
k_{01} (kHz)	2.0	2.03 ± 0.05	2.05 ± 0.04	1.6 ± 0.5		1.62 ± 0.91
C_1 (mol)	0.5	0.45 ± 0.08	0.43 ± 0.13	0.51 ± 0.12		0.57 ± 0.09
τ_1^D (μ s)	100.0	88 ± 18	95 ± 25	92 ± 16		N.A.
q_{11} (kHz/mol)	50.0	52.5 ± 4.4	50.4 ± 5.0	51.5 ± 7.7		45.6 ± 11.3
C_2 (mol)	0.5	0.53 ± 0.07	0.56 ± 0.12	0.50 ± 0.13		0.52 ± 0.14
τ_2^D (μ s)	150.0	153 ± 4	148 ± 10	144 ± 12		N.A.
q_{21} (kHz/mol)	100.0	96.4 ± 3.1	94.4 ± 5.6	101.2 ± 6.5		96.9 ± 5.8

For the single-species simulations, the PAID method performed well; the average error for each parameter was at most 2% for both the low and high occupancy simulations. The fitted values for the background levels were factors of 500 and 1700 below the average count rates of the low and high occupancy simulations, respectively. This indicates that the PAID method is able to detect the presence or absence of the background. The parameters for the single diffusing species were also extracted correctly. The diffusion time and brightness parameters extracted by PAID in the low

occupancy simulations may have a 2% bias downward (the mean value found for these parameters is off by more than 1/3 of the standard deviation). The fit for one PAID histogram is shown in Fig. 3.7. The fit is within the error bars for almost all of the data points (some are outside, which is expected for accurately estimated error bars).

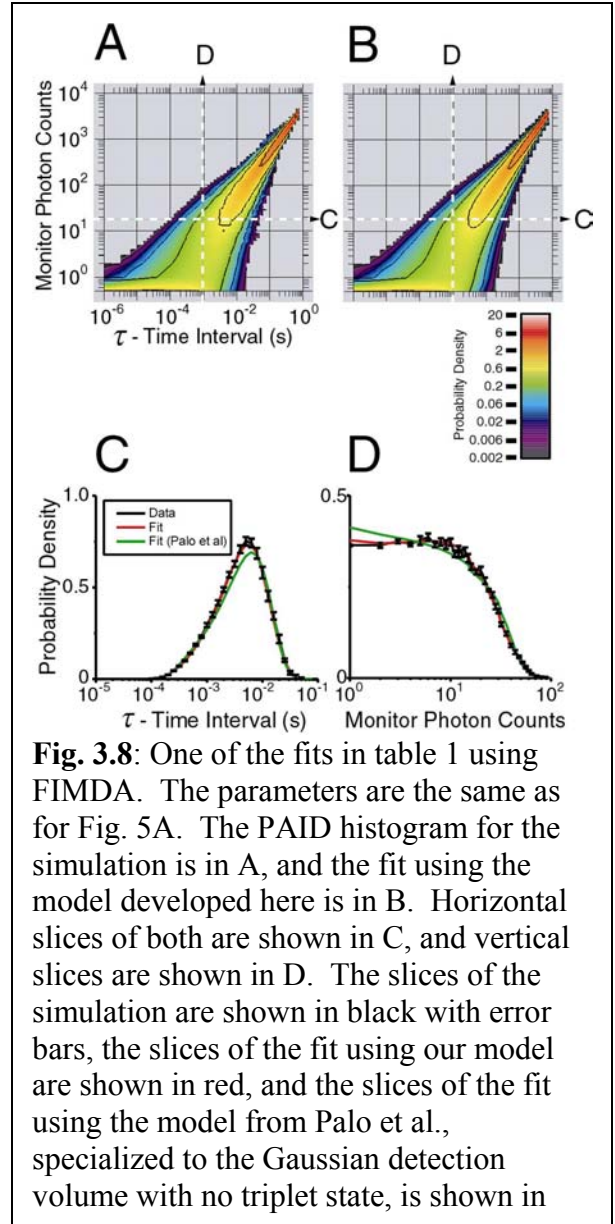
PAID also performed well with the two-species simulations. The errors in the parameters extracted from the intermediate occupancy simulations (3%-20%) are larger than those extracted from the low occupancy simulations (3%-8%). For the



intermediate occupancy simulations, there are biases in the values extracted for the concentration and diffusion time of the dimmer species of around 10%.

It is interesting to compare the performance of PAID with FIMDA, since both methods have the same capabilities for the simultaneous extraction of occupancy, diffusion time, and molecular brightness for a single channel. To provide a more direct comparison to PAID, the FIMDA histograms were created using the same time bin sizes and photon count bins as the PAID histogram (appendix 3.A). The spacing between each counted time interval was set to 10 μ s; for longer time bin sizes, a given photon

contributes to several counted intervals. Therefore, each entry into the histogram is not independent, and the error bars are determined by forming several histograms and calculating the standard deviation [142]. The columns in tables 3.2 and 3.3 labeled “modified FIMDA” use our model to extract the parameters from the histograms, and the columns labeled “FIMDA” use the original FIMDA model. With the exception of the simulations for the mixture at intermediate occupancy, the accuracy of the parameters extracted using the modified FIMDA model was very similar to the accuracy found using PAID. For the mixture at intermediate occupancy, the errors found using the modified FIMDA model are consistently larger than the errors found using PAID (except for the background; the errors in occupancies are 24% and 26% rather than 16% and 14%). It may be that the PAID histogram has better resolving power than the FIMDA histogram in this regime (additional simulations over a wider range of parameter values will be needed to verify this, and help discover the cause).



Some differences were found between fitting the FIMDA histograms with the modified FIMDA model and the original model proposed in [130]. For the single-species simulations at low occupancy, the accuracy of the extracted values is similar to the accuracy found using PAID and modified FIMDA, but χ^2 is significantly higher than 1. This comes from the region where time delays are larger than the diffusion time. The fits for one modified FIMDA histogram using the modified FIMDA model and the original FIMDA model are shown in Fig. 3.8. It is possible to see in fig. 3.8C and 3.8D the deviation of the FIMDA model (*green line*) from the data (*black line*). For the single-species simulations at intermediate occupancy, the χ^2 is near 1, and the extracted parameters are close to the simulation values, except for a 5% downward bias in the diffusion time. The parameters extracted using the FIMDA model for the simulations of the mixtures had larger biases than those extracted with the modified FIMDA model. For the low occupancy mixture, the biases in the occupancies were close to 20%. It performed better with the intermediate occupancy simulations (with smaller biases in the occupancy values), except that the background count rate values extracted were off by 25%. We attribute the increased biases found using the original FIMDA model to the assumption made that the functional form of the photon counting histogram changes only through changes in effective brightness and effective occupancy. In the view of the original model, at time bins larger than the diffusion time, the effective occupancy is increased while the effective brightness is reduced; the detection volume increases in size as time passes, but retains the same shape. This view does not account for the dynamic picture, neglecting for example the chance that a molecule re-crosses the detection volume.

The accuracy of the parameters extracted from the single-species simulations using FCS was similar to that found using PAID and FIMDA (except that the brightness is not able to be extracted). The diffusion times found did have a 5% downward bias. For the mixture simulations, the FCS fits did not converge in either the high or low occupancy simulations. Significantly different results with the same χ^2 were found with the same data set. This problem arises because FCS relies on only the diffusion time to detect the presence of multiple subpopulations. Even if the subpopulations were detected in this case, there would be additional problems. The background level and the brightness of the species must be determined using other methods to extract occupancy. Even with this information available, it is still not possible to tell which brightness corresponds to which diffusion time.

The statistical errors of the parameters extracted using FIDA for the single-species simulations were similar to the errors found using the other methods. The time bin width used for the simulations was chosen to be 1/5 the shortest diffusion time (20 μs). The short time bin width is necessary since the FIDA model assumes the molecules are stationary during the counting interval (this also precludes the extraction of diffusion time). Even with this short time bin, there is some upward bias in the occupancies extracted, along with some downward bias in the brightness values extracted due to the diffusion of the species during the time bin. The errors of the parameters extracted from the two-species simulations were larger for FIDA than for the other methods (for 8 out of 10 extracted parameters, FIDA had the largest errors for all of the fits, excluding FCS).

3.4.2. Simulations – monitoring binding with two channels

The use of PAID and cross-correlation FCS in two-channel applications with two spectrally separable fluorophores is investigated using multiple species simulations. Three species are present (same as introduced in section 3.2.4): free molecules labeled with a yellow fluorophore (A^y), free molecules labeled with a red fluorophore (B^r), and complexes of these two species (A^yB^r). The diffusion time of A^yB^r is increased by 33% as compared to A^y and B^r , but the brightness of each fluorophore is assumed to be unaffected. As in the single-channel case, there are two occupancy regimes investigated, the low and intermediate occupancy regimes. The simulations for tables 3.4 and 3.5 were created with these three subpopulations plus background. The fluorophore y was set to have a total brightness of 50.0 kHz, 90% in channel Y and 10% in channel R . The fluorophore r was set to have a total brightness of 50.0 kHz, 100% in channel R . The background level was set to $k_{0G} = k_{0R} = 2.0$ kHz.

Table 3.4 shows the estimated parameters extracted from the simulations with low occupancy, and table 3.5 shows the estimated parameters extracted from simulations with intermediate occupancy. The first column lists the parameters of the fit, along with χ^2 . The second column lists the parameter values for the simulations, which were 30 s long for table 3.4 and 10 s long for table 3.5. For each simulation, three fits were performed. The results are in the third, fourth, and fifth columns. The first fit uses PAID with all parameters freely varying. The second fit also uses PAID, but the parameters for the background and free molecules are all fixed, except for the occupancies of the free components. For these two PAID fits, all combinations of the two-channel PAID

Table 3.4: Parameters Extracted using PAID and cross-correlation FCS for two-channel, three-component simulations in a Gaussian detection volume at low occupancy

Parameters	Simulation	PAID Fit - Unrestricted	PAID Fit - Restricted	Cross-correlation FCS Fit
10 Simulations (30 s each): Low Occupancy ($C_1 = C_2 = C_3 = 0.05$)				
χ^2	-	0.72 ± 0.05	0.79 ± 0.07	0.95 ± 0.12
k_{0R} (kHz)	<i>2.0</i>	2.00 ± 0.01	<i>2.0</i>	<i>2.0</i>
k_{0Y} (kHz)	<i>2.0</i>	2.00 ± 0.01	<i>2.0</i>	<i>2.0</i>
C_1 (mol)	<i>0.05</i>	0.049 ± 0.003	0.049 ± 0.003	0.050 ± 0.004
τ_1^D (μ s)	<i>300.0</i>	287 ± 21	<i>300.0</i>	296 ± 12
q_{1R} (kHz/mol)	<i>50.0</i>	50.3 ± 1.1	<i>50.0</i>	<i>50.0</i>
q_{1Y} (kHz/mol)	<i>0.0</i>	0.05 ± 0.03	<i>0.0</i>	<i>0.0</i>
C_2 (mol)	<i>0.05</i>	0.049 ± 0.003	0.050 ± 0.003	0.050 ± 0.003
τ_2^D (μ s)	<i>300.0</i>	294 ± 21	<i>300.0</i>	291 ± 12
q_{2R} (kHz/mol)	<i>5.0</i>	4.8 ± 0.2	<i>5.0</i>	<i>5.0</i>
q_{2Y} (kHz/mol)	<i>45.0</i>	44.8 ± 0.8	<i>45.0</i>	<i>45.0</i>
C_3 (mol)	<i>0.05</i>	0.050 ± 0.003	0.050 ± 0.003	0.051 ± 0.002
τ_3^D (μ s)	<i>400.0</i>	394 ± 17	389 ± 20	385 ± 23
q_{3R} (kHz/mol)	<i>55.0</i>	54.9 ± 0.9	55.2 ± 0.2	<i>55.0</i>
q_{3Y} (kHz/mol)	<i>45.0</i>	44.7 ± 0.6	44.8 ± 0.2	<i>45.0</i>

Values that are fixed are shown in italics, with no errors listed.

histogram, as listed in table 3.1, are fitted simultaneously. Because each histogram emphasizes different species, this allows the parameters for all species to be extracted. The results for these two fits are shown in the third and fourth columns of tables 3.4 and 3.5. The third fit uses cross-correlation FCS to simultaneously fit the autocorrelations of the red and yellow channels and the two cross-correlations, with all of the brightness values and background rates fixed.

The fit performed using PAID without any restrictions on parameter values extracted reliable values (within 1-10% for all parameters in both sets of simulations).

Table 3.5: Parameters Extracted using PAID and cross-correlation FCS for two-channel, three-component simulations in a Gaussian detection volume at intermediate occupancy

Parameters	Simulation	PAID Fit - Unrestricted	PAID Fit - Restricted	Cross-correlation FCS Fit
10 Simulations (10 s each): Intermediate Occupancy ($C_1 = C_2 = C_3 = 0.5$)				
χ^2	-	0.81 ± 0.05	0.90 ± 0.11	0.76 ± 0.29
k_{0R} (kHz)	2.0	2.02 ± 0.06	2.0	2.0
k_{0Y} (kHz)	2.0	2.00 ± 0.05	2.0	2.0
C_1 (mol)	0.5	0.50 ± 0.01	0.49 ± 0.02	0.050 ± 0.02
τ_1^D (μ s)	300.0	320 ± 28	300.0	298 ± 10
q_{1R} (kHz/mol)	50.0	49.1 ± 0.6	50.0	50.0
q_{1Y} (kHz/mol)	0.0	0.06 ± 0.07	0.0	0.0
C_2 (mol)	0.5	0.49 ± 0.02	0.49 ± 0.02	0.50 ± 0.03
τ_2^D (μ s)	300.0	306 ± 32	300.0	289 ± 21
q_{2R} (kHz/mol)	5.0	4.9 ± 0.5	5.0	5.0
q_{2Y} (kHz/mol)	45.0	44.5 ± 1.2	45.0	45.0
C_3 (mol)	0.5	0.50 ± 0.03	0.49 ± 0.02	0.49 ± 0.02
τ_3^D (μ s)	400.0	395 ± 13	390 ± 19	388 ± 16
q_{3R} (kHz/mol)	55.0	54.3 ± 1.1	55.0 ± 0.8	55.0
q_{3Y} (kHz/mol)	45.0	44.5 ± 1.5	45.1 ± 0.5	45.0

Unexpectedly, the accuracy of the extracted parameters did not increase dramatically by restricting the parameters for the brightness of the free components and the background rates (there was an improvement for the brightness values for the complex, but no improvement for the diffusion time or for the occupancies).

The parameters extracted using cross-correlation FCS had similar statistical accuracy (in the 4-7% range) to those found using PAID. The diffusion time values may be somewhat better with cross-correlation FCS (the error bars were on average 20% smaller), but there are fewer than half as many freely varying parameters. We fixed all of

the brightness and background parameters to their simulation values, and thus were able to extract the correct occupancies. For experiments, it would be necessary to measure the background and brightness values using a different method than FCS.

This analysis demonstrates that it is possible to extract the occupancy, diffusion time, and brightness in multiple channels of several species by fitting all of the two-channel PAID histograms simultaneously. This provides the ability to perform consistency checks between the parameters extracted for the free components in the experiment versus the control experiments, and increasing the applicability of FCS-related methods to areas where precise controls are more difficult to develop. For example, the autofluorescence background in living cells would change as a function of position. It would not be possible to obtain background measurements for a particular spatial position in a cell with different fluorescent species present.

3.4.3. One-channel experiments

Measurements were performed on the DNA fragments (described in section 3.3.3) to test the ability of PAID to detect subpopulations in solution based on the properties available in a single channel. Three samples were tested in the intermediate occupancy regime. The first contained 1 nM of Cy3-dsDNA, and the second contained 1 nM of Cy3-dsDNA-Cy3. The third contained 1 nM each of Cy3-dsDNA and Cy3-dsDNA-Cy3. The concentration of DNA was determined using UV-Vis spectrophotometry ($\epsilon_{\text{Cy3}, 550}=150,000 \text{ cm}^{-1}\text{M}^{-1}$; $\epsilon_{\text{Cy3}, 650}=250,000 \text{ cm}^{-1}\text{M}^{-1}$) and fluorescence spectrophotometry.

By assuming that the dsDNA is a rod-like polymer with length $L = 240 \text{ \AA}$, and diameter $b = 20 \text{ \AA}$, we calculate the averaged translational diffusion constant using [accounting for transverse and longitudinal diffusion; [103]],

$$D = \frac{\ln(L/b)}{3\pi\eta L} k_B T. \quad (3.11)$$

η is the dynamic viscosity of the solution [$\eta = 1.16 \text{ mPa s}$ for an aqueous solution containing 5% glycerol (by volume); [150]]. Using these values and $T = 25 \text{ }^\circ\text{C}$, the translational diffusion constant is $D = 3.9 \times 10^{-7} \text{ cm}^2/\text{s}$. For the volume described in section 3.3.1, these dsDNA fragments have a diffusion time of $\tau^D = 710 \text{ }\mu\text{s}$. This value will be compared to the parameters extracted from experimental data sets.

Table 3.6 shows the results of fits using PAID for the single-species samples as well as the mixture. For the single-species samples, all parameters are allowed to vary except for the background. The background level was determined in a separate, buffer-only experiment. The diffusion times and brightness of each component is then fixed in the fit for the mixture. As mentioned in section 3.3.1, the occupancy of the calculated detection volume for a 1 nM sample should be 1.9. The occupancies extracted from the Cy3-dsDNA only sample ($c = 2.09$) and the Cy3-dsDNA-Cy3 only sample ($c = 3.48$) provide a test of the size of the confocal detection volume. The occupancies extracted from the two single-species samples are larger than the occupancy ($c = 1.9$) expected from the detection volume calculation, perhaps indicating a detection volume larger than calculated. The diffusion times extracted, however, are 10%-30% smaller than expected for the dsDNA fragments in the calculated detection volume (710 μs). Although the error

Table 3.6: Parameters Extracted using PAID for single-channel, one- and two-component, intermediate occupancy experiments

Parameters	Cy3-dsDNA	Cy3-dsDNA-Cy3	Cy3-dsDNA, Cy3-dsDNA-Cy3
10 Fits (30 s each): Intermediate Occupancy			
χ^2	6.2 ± 0.8	2.6 ± 0.3	0.42 ± 0.16
k_{01} (kHz)	1390*	1390	1390
DNA Fragment 1	Cy3-dsDNA	None	Cy3-dsDNA
C_1 (mol)	2.09 ± 0.03		2.4 ± 0.9
τ_1^D (μ s)	502 ± 14		502
q_{11} (kHz/mol)	12.8 ± 0.2		12.8
DNA Fragment 2	None	Cy3-dsDNA-Cy3	Cy3-dsDNA-Cy3
C_2 (mol)		3.48 ± 0.05	4.2 ± 0.9
τ_2^D (μ s)		630 ± 19	630
q_{21} (kHz/mol)		20.8 ± 0.5	20.8

*Background was determined by an experiment with buffer only

distribution is quite wide (up to 40%), the occupancies extracted from the mixture are consistent with the occupancies extracted from the single-species samples.

3.4.4. Two-channel experiments

Measurements were performed on the DNA fragments (described in section 3.3.3) to test the ability of PAID analysis to detect subpopulations in solution and to measure their properties, as would be necessary in a binding experiment. The fluorophores used were Cy3 (as the yellow fluorophore y) and Cy5 (as the red fluorophore r). The concentration of Cy5-dsDNA (1 nM) was determined using UV-Vis spectrophotometry ($\epsilon_{\text{Cy5}, 650}=250,000 \text{ cm}^{-1}\text{M}^{-1}$) and fluorescence spectrophotometry. The occupancy determined using FCS was 1.8, which is lower than the results with Cy3-dsDNA and

Cy3-dsDNA-Cy3 in section 3.4.3. This is most likely due to the properties of Cy5; when performing single-molecule measurements using Cy5 as a FRET acceptor, a large percentage of the molecules had non-fluorescent Cy5, a well-known phenomenon possibly due to photobleaching [33]. Initial, higher concentration (>10 nM) samples were prepared for dsDNA-Cy3 and Cy5-dsDNA-Cy3. Occupancies and diffusion times were extracted using FCS. Based on the occupancies measured at higher concentration and the dilutions used, the occupancies for the intermediate occupancy samples are estimated to be 0.85 ± 0.09 for Cy5-dsDNA, 1.15 ± 0.05 for dsDNA-Cy3, and 0.84 ± 0.03 for Cy5-dsDNA-Cy3. The occupancies for the low occupancy samples are 10 times smaller. The value for Cy5-dsDNA-Cy3 was found by analyzing the Cy3 fluorescence,

Table 3.7: Expected occupancies of samples for two-channel test experiments

Sample	Cy5-dsDNA	dsDNA-Cy3	Cy5-dsDNA-Cy3
Low Occupancy			
1	0.085 ± 0.009		
2		0.115 ± 0.005	
3			0.084 ± 0.003
4	0.085 ± 0.009	0.115 ± 0.005	
5	0.085 ± 0.009	0.115 ± 0.005	0.084 ± 0.003
Intermediate Occupancy			
6	0.85 ± 0.09		
7		1.15 ± 0.05	
8			0.84 ± 0.03
9	0.85 ± 0.09	1.15 ± 0.05	
10	0.85 ± 0.09	1.15 ± 0.05	0.84 ± 0.03

so the occupancy quoted includes Cy5-dsDNA-Cy3 and ~~Cy5~~-dsDNA-Cy3 (with photobleached Cy5).

The fragments were prepared alone and in mixtures, with concentrations corresponding to low and intermediate occupancy. The compositions of the test samples are listed in table 3.7; each dsDNA fragment added to a sample is listed with the occupancy that is expected to be extracted using PAID. Samples 1-3 and 6-8 were solutions of a single DNA fragment, either Cy5-dsDNA, dsDNA-Cy3, or Cy5-dsDNA-Cy3. These correspond to A^y , B^r , and A^yB^r in the binding simulations in section 3.4.2. Samples 4 and 9 were mixtures of dsDNA-Cy3 and Cy5-dsDNA, which correspond, respectively, to the species A^y and B^r in the simulations in section 3.4.2. Finally, samples 5 and 10 were mixtures of dsDNA-Cy3, Cy5-dsDNA, and Cy5-dsDNA-Cy3, which correspond to the species A^y , B^r , and A^yB^r in section 3.4.2.

Fig. 3.9 shows PAID histograms for two of the low occupancy data sets: the first from the sample with Cy5-dsDNA, dsDNA-Cy3, and Cy5-dsDNA-Cy3 present (Figs. 3.9A-D), and the second from the sample with only Cy5-dsDNA and dsDNA-Cy3 (Figs. 3.9E-H). Figs. 3.9I-L compares vertical slices at time interval $\tau = 1$ ms for the histograms in the presence and absence of Cy5-dsDNA-Cy3. These experimental PAID histograms are plotted in the same format as the PAID histograms in Fig. 3.5, which were for simulations. By comparing the Figs. 3.9A-D and Figs. 3.9E-H, it is possible to see the effects of the presence of the double-labeled species Cy5-dsDNA-Cy3.

Figs. 3.9A, 3.9E, and 3.9I use the red channel (R) as the start, stop, and monitor channels emphasizing Cy5-dsDNA and Cy5-dsDNA-Cy3. However, it does not distinguish well between these species since they both emit approximately equally in the

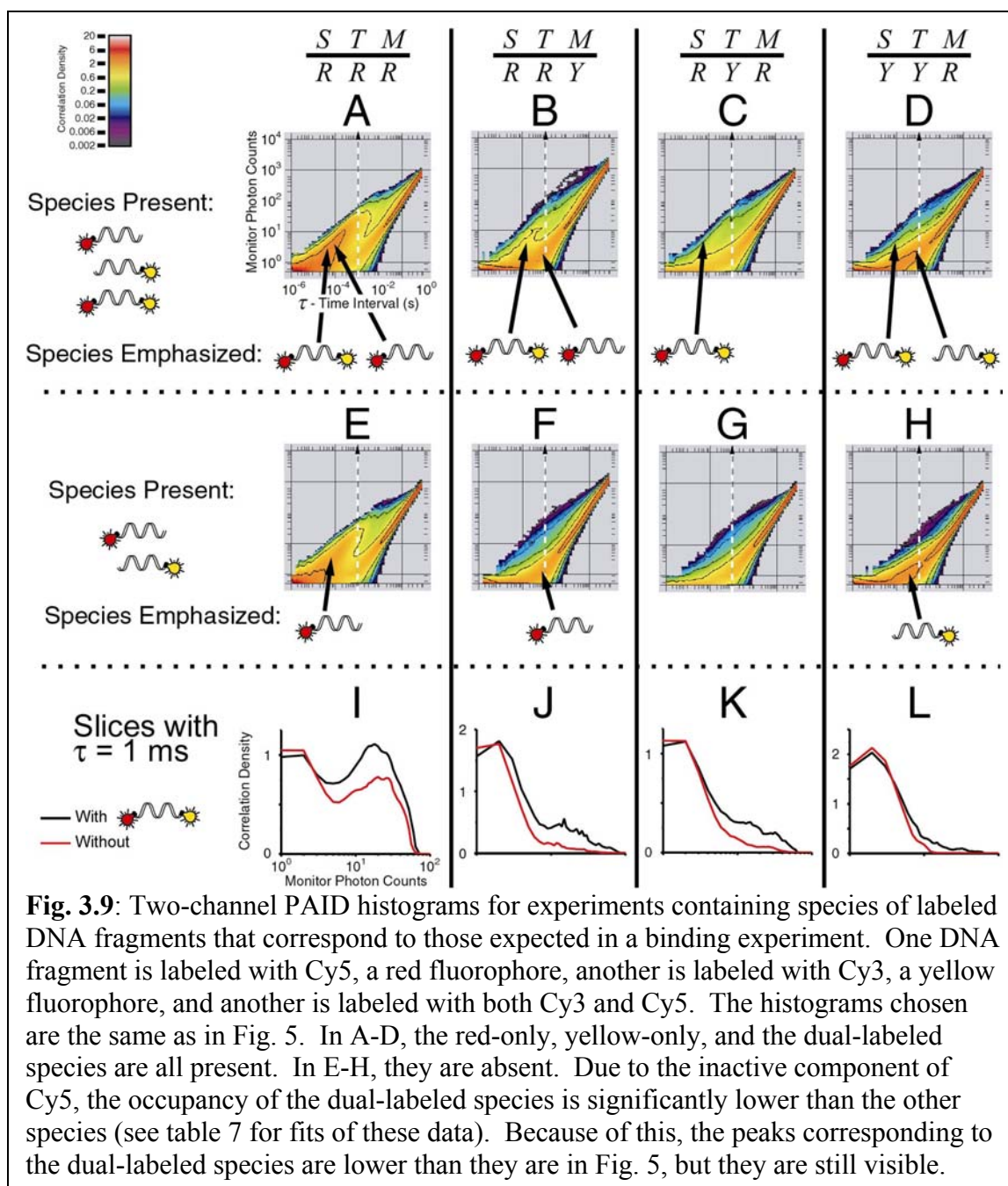


Fig. 3.9: Two-channel PAID histograms for experiments containing species of labeled DNA fragments that correspond to those expected in a binding experiment. One DNA fragment is labeled with Cy5, a red fluorophore, another is labeled with Cy3, a yellow fluorophore, and another is labeled with both Cy3 and Cy5. The histograms chosen are the same as in Fig. 5. In A-D, the red-only, yellow-only, and the dual-labeled species are all present. In E-H, they are absent. Due to the inactive component of Cy5, the occupancy of the dual-labeled species is significantly lower than the other species (see table 7 for fits of these data). Because of this, the peaks corresponding to the dual-labeled species are lower than they are in Fig. 5, but they are still visible.

channel R . The omission of the Cy5-dsDNA-Cy3 decreases amplitude of the correlation density peak. At this low occupancy the background produces the majority of the photons, and, in contrast to the typical situation in FCS, a decrease in occupancy decreases the correlation amplitude rather than increasing it.

In Figs. 3.9B, 3.9F, and 3.9J, the monitor channel is set to channel Y . This configuration emphasizes the same two species, but is able to distinguish between them since Cy5-dsDNA does not emit in channel Y whereas Cy5-dsDNA-Cy3 does. Figs. 3.9C and 3.9G assign the channel R as the start channel, the channel Y as the stop channel, and the channel R as the monitor channel. This configuration emphasizes Cy5-dsDNA-Cy3. Without Cy5-dsDNA-Cy3, the peak shown by the arrow in Fig. 3.9C disappears.

Finally, Figs. 3.9D and 3.9H assign the channel Y as the start and stop channels, and the channel R as the monitor channel. This configuration emphasizes dsDNA-Cy3 and Cy5-dsDNA-Cy3, separating them by their emission in channel R . In this case, because the occupancy of dsDNA-Cy3 is quite a bit higher than Cy5-dsDNA-Cy3, the peak corresponding to Cy5-dsDNA-Cy3 is less pronounced, although it is still significant.

For both the low and intermediate occupancy data sets, 300 s of data were collected. The intermediate occupancy data sets were split into 10 sections of 30 s each. PAID histograms were calculated for each of the 10 sections, and the standard deviation of each bin was calculated to estimate the error of each bin. Each section was fit separately, and the mean and standard deviation of each fitted parameter is listed in the table, as was done for the simulations.

The same procedure was performed for the low occupancy data sets. However, there were too few bursts from the Cy5-dsDNA-Cy3 and C5-dsDNA fragments. The errors in the diffusion times were too large (on the order of the diffusion time itself). Therefore, we fit the histogram of the data for all 300 s in order to obtain better statistics.

We used bootstrap sampling to obtain error estimates for the extracted parameters [151]. We again split the data into 10 sections of 30 s each and randomly selected 10 of these 30 s sections (with replacement), averaging the PAID histograms for the selected sections. We repeated this process 10 times, and fit each of the resulting histograms. The standard deviation of the 10 values extracted for each parameter is quoted as error bars in each table for low occupancy data.

Tables 3.8 and 3.9 show the results of fits for the single-species samples: dsDNA-Cy3, Cy5-dsDNA, and Cy5-dsDNA-Cy3. Using the detection volume described in section 3.3.1, we obtained fits with χ^2 values in the range 1-10 (ideally $\chi^2 \sim 1$). The

Table 3.8: Parameters extracted using PAID for two-channel, single-species, low occupancy experiments

Parameters	Sample 1, Cy5-dsDNA	Sample 2, dsDNA-Cy3	Sample 3, Cy5-dsDNA-Cy3
1 Fit* (300 s): Low occupancy			
χ^2	9.4 ± 0.7	5.5 ± 0.1	1.9 ± 0.3
k_{0R} (kHz)	0.82 ± 0.01	0.76 ± 0.01	0.68 ± 0.01
k_{0Y} (kHz)	1.30 ± 0.03	1.14 ± 0.03	0.95 ± 0.01
<i>DNA Fragment 1</i>	<i>Cy5-dsDNA</i>	<i>dsDNA-Cy3</i>	<i>Cy5-dsDNA-Cy3</i>
C_1 (mol)	0.026 ± 0.001	0.073 ± 0.003	0.023 ± 0.003
τ_1^D (μ s)	565 ± 21	570 ± 9	665 ± 64
q_{1R} (kHz/mol)	10.2 ± 0.4	0.94 ± 0.03	0.8 ± 0.1
q_{1Y} (kHz/mol)	0.06 ± 0.02	10.0 ± 0.3	9.2 ± 0.8
<i>DNA Fragment 2</i>	<i>None</i>	<i>None</i>	<i>Cy5-dsDNA-Cy3</i>
C_2 (mol)			0.012 ± 0.001
τ_2^D (μ s)			650 ± 10
q_{2R} (kHz/mol)			6.8 ± 0.3
q_{2Y} (kHz/mol)			6.7 ± 0.3

*All 300 s of low occupancy data fit at once to improve statistics

discrepancy can be attributed to photophysical properties of the dyes such as triplet state fluctuations, saturation of fluorescence, and photobleaching, or to the deviation of the experimental detection volume from the modeled volume. If the Gaussian detection volume used for the simulations is used to fit the experimental, significantly higher χ^2 values are found. For example, fitting the dsDNA-Cy3 data sets resulted in fits with $\chi^2 = 13.1$ and $\chi^2 = 32.5$ for the low occupancy and high occupancy data sets, respectively. With the more accurate detection volume, the values are $\chi^2 = 5.5$ and $\chi^2 = 2.2$. This highlights the critical role the shape of the detection volume plays in the model.

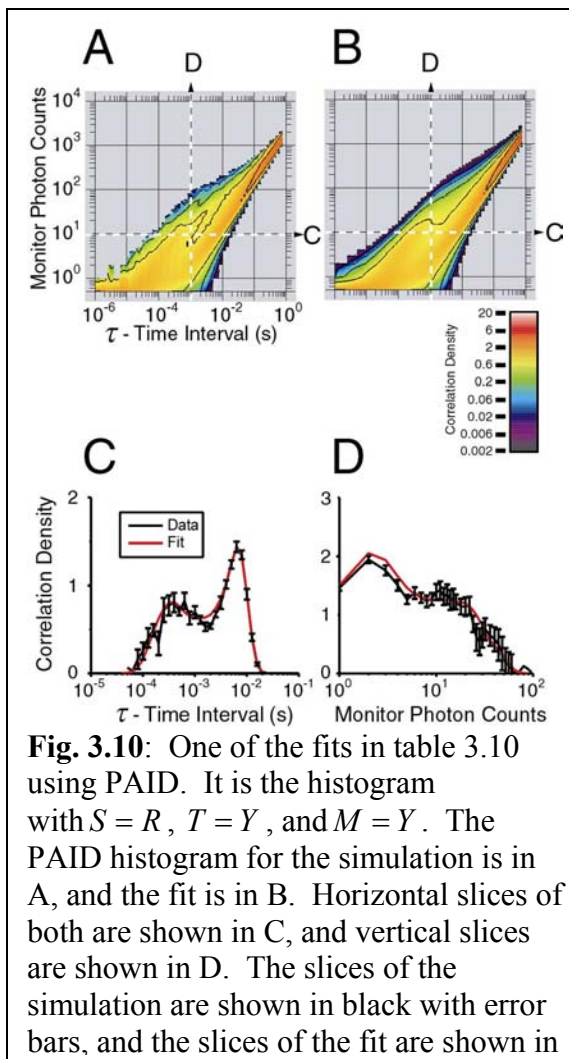
Table 3.9: Parameters extracted using PAID for two-channel, single-species, intermediate occupancy experiments

Parameters	Sample 6, Cy5-dsDNA	Sample 7, dsDNA-Cy3	Sample 8, Cy5-dsDNA-Cy3
10 Fit (30 s): Intermediate occupancy			
χ^2	4.7 ± 0.5	2.2 ± 0.3	1.4 ± 0.1
k_{0R} (kHz)	1.30 ± 0.01	0.99 ± 0.01	0.92 ± 0.03
k_{0Y} (kHz)	1.33 ± 0.03	1.44 ± 0.01	1.29 ± 0.03
<i>DNA Fragment 1</i>	<i>Cy5-dsDNA</i>	<i>dsDNA-Cy3</i>	<i>Cy5-dsDNA-Cy3</i>
C_1 (mol)	0.68 ± 0.02	1.08 ± 0.04	0.32 ± 0.03
τ_1^D (μ s)	389 ± 24	554 ± 59	703 ± 36
q_{1R} (kHz/mol)	9.4 ± 0.5	0.82 ± 0.03	0.70 ± 0.09
q_{1Y} (kHz/mol)	0.02 ± 0.01	9.0 ± 0.4	10.7 ± 0.7
<i>DNA Fragment 2</i>	<i>None</i>	<i>None</i>	<i>Cy5-dsDNA-Cy3</i>
C_2 (mol)			0.24 ± 0.02
τ_2^D (μ s)			575 ± 13
q_{2R} (kHz/mol)			7.6 ± 0.4
q_{2Y} (kHz/mol)			7.6 ± 0.5

Fig. 3.10 shows an example of one of the fits for table 3.10. It is the histogram with $S = R$, $T = Y$, and $M = Y$. This histogram emphasizes only the species Cy5-dsDNA-Cy3. The peak toward higher photon counts in the vertical slice is caused by this species. The fit is usually within the error bars, and follows the data to within 10%.

The background rates, occupancies, diffusion times, and brightness in each channel were free parameters. To fit the data for the Cy5-dsDNA-Cy3 fragment in samples 3 and 8, two components were necessary, one with Cy3 only and another with Cy3 and Cy5 (due to the photobleached or non-fluorescent Cy5). When parameters corresponding to Cy5-dsDNA were added, there was only a small occupancy fitted (~ 0.001 , not shown).

The results for samples 4, 5, 10, and 11 (composed of mixtures of DNA fragments) are shown in tables 3.10 and



3.11. The dsDNA-Cy3 and Cy5-dsDNA mixture simulates non-interacting species in solution, and the dsDNA-Cy3, Cy5-dsDNA, and Cy5-dsDNA-Cy3 mixture simulates an interacting species in solution. For each sample, we show two fits using PAID. The first fit assumes the correct number of species, but allows all of the parameters to freely vary.

Table 3.10: Parameters extracted using PAID for two-channel, multiple-species, low occupancy experiments

Parameters	Sample 4 dsDNA-Cy3, Cy5-dsDNA Unrestricted 2 component	Sample 4 dsDNA-Cy3, Cy5-dsDNA Restricted 3 component	Sample 5 dsDNA-Cy3, Cy5-dsDNA, Cy5-dsDNA-Cy3, Unrestricted 3 component	Sample 5 dsDNA-Cy3, Cy5-dsDNA, Cy5-dsDNA-Cy3, Restricted 3 component
1 Fit (300 s): Low occupancy				
χ^2	2.8 ± 0.2	34 ± 2	2.3 ± 0.4	12 ± 1
k_{0R} (kHz)	0.87 ± 0.01	0.71	0.80 ± 0.01	0.71
k_{0Y} (kHz)	1.04 ± 0.01	1.15	1.12 ± 0.01	1.15
DNA Fragment 1	<i>Cy5-dsDNA</i>	<i>Cy5-dsDNA</i>	<i>Cy5-dsDNA</i>	<i>Cy5-dsDNA</i>
C_1 (mol)	0.018 ± 0.001	0.028 ± 0.001	0.011 ± 0.001	0.027 ± 0.001
τ_1^D (μ s)	430 ± 9	565	357 ± 4	565
q_{1R} (kHz/mol)	11.0 ± 0.2	10.2	15.4 ± 0.4	10.2
q_{1Y} (kHz/mol)	0.01 ± 0.02	0.06	0.02 ± 0.03	0.06
DNA Fragment 2	<i>dsDNA-Cy3</i>	<i>dsDNA-Cy3</i>	<i>dsDNA-Cy3</i>	<i>dsDNA-Cy3</i>
C_2 (mol)	0.068 ± 0.001	0.065 ± 0.001	0.077 ± 0.003	0.085 ± 0.001
τ_2^D (μ s)	526 ± 5	570	571 ± 13	570
q_{2R} (kHz/mol)	0.95 ± 0.02	0.94	0.89 ± 0.02	0.94
q_{2Y} (kHz/mol)	10.2 ± 0.1	10.0	11.2 ± 0.3	10.0
DNA Fragment 3	<i>None</i>	<i>Cy5-dsDNA-Cy3</i>	<i>Cy5-dsDNA-Cy3</i>	<i>Cy5-dsDNA-Cy3</i>
C_3 (mol)		0.001 ± 0.001	0.015 ± 0.002	0.014 ± 0.001
τ_3^D (μ s)		650	684 ± 35	650
q_{3R} (kHz/mol)		6.8	7.3 ± 0.7	6.8
q_{3Y} (kHz/mol)		6.7	6.8 ± 0.3	6.7

* Includes contributions from ~~Cy5~~-dsDNA-Cy3

The second fit uses the single-species parameters already extracted to restrict the parameters for the free components, except for occupancy. These fits allow us to show that a sample with two species can be distinguished from a sample with three species, as is necessary for a binding experiment.

Table 3.11: Parameters extracted using PAID for two-channel, multiple-species, intermediate occupancy experiments

Parameters	Sample 9 dsDNA-Cy3, Cy5-dsDNA Unrestricted 2 component	Sample 9 dsDNA-Cy3, Cy5-dsDNA Restricted 3 component	Sample 10 dsDNA-Cy3, Cy5-dsDNA, Cy5-dsDNA-Cy3, Unrestricted 3 component	Sample 10 dsDNA-Cy3, Cy5-dsDNA, Cy5-dsDNA-Cy3, Restricted 3 component
10 Fits (30 s each): Intermediate occupancy				
χ^2	1.8 ± 0.1	3.0 ± 0.5	3.0 ± 0.3	4.8 ± 0.7
k_{0R} (kHz)	1.4 ± 0.1	0.71	1.66 ± 0.02	0.71
k_{0Y} (kHz)	1.44 ± 0.01	1.15	1.3 ± 0.1	1.15
DNA Fragment 1	Cy5-dsDNA	Cy5-dsDNA	Cy5-dsDNA	Cy5-dsDNA
C_1 (mol)	0.43 ± 0.03	0.57 ± 0.02	0.37 ± 0.03	0.74 ± 0.03
τ_1^D (μ s)	353 ± 23	389	356 ± 33	389
q_{1R} (kHz/mol)	11.0 ± 0.4	9.4	14.5 ± 1.1	9.4
q_{1Y} (kHz/mol)	0.20 ± 0.09	0.02	0.3 ± 0.2	0.02
DNA Fragment 2	dsDNA-Cy3	dsDNA-Cy3	dsDNA-Cy3*	dsDNA-Cy3*
C_2 (mol)	0.86 ± 0.02	0.96 ± 0.02	1.0 ± 0.2	1.56 ± 0.03
τ_2^D (μ s)	559 ± 25	554	503 ± 44	554
q_{2R} (kHz/mol)	0.75 ± 0.05	0.82	0.5 ± 0.2	0.82
q_{2Y} (kHz/mol)	9.8 ± 0.4	9.0	11.5 ± 0.9	9.0
DNA Fragment 3	None	Cy5-dsDNA-Cy3	Cy5-dsDNA-Cy3	Cy5-dsDNA-Cy3
C_3 (mol)		0.01 ± 0.01	0.58 ± 0.15	0.22 ± 0.03
τ_3^D (μ s)		575	451 ± 10	575
q_{3R} (kHz/mol)		7.6	5.3 ± 1.1	7.6
q_{3Y} (kHz/mol)		7.6	6.4 ± 0.4	7.6

* Includes contributions from ~~Cy5~~-dsDNA-Cy3

The occupancies extracted (shown in tables 3.8-3.11) are less than those estimated in table 3.7. For the single-species, low occupancy data (table 3.8), the extracted occupancies were 35%-70% lower than expected, whereas for the single-species, intermediate occupancy samples, they are 4%-20% lower than expected (note that in comparing the occupancies for the Cy5-dsDNA-Cy3 samples with table 3.7, the

occupancies for Cy5-dsDNA-Cy3 and ~~Cy5~~-dsDNA-Cy3 are added). The difference between the extracted and estimated occupancies may be due to sticking of the DNA to the coverslip or to the walls of tubes during handling (this issue arises more often at low concentrations). The diffusion times extracted for the Cy5-dsDNA-Cy3 and dsDNA-Cy3 fragments are similar to what is expected from the calculation in section 3.3.3 (554-703 μs compared to 710 μs). The diffusion times for the Cy5-dsDNA fragments tend to be shorter (389-565 μs). This is likely due to photobleaching of Cy5 within the confocal detection volume.

The occupancies extracted from the mixture samples using the restricted fits were consistent with the occupancies extracted from the single-species samples (within 16%). The fits for the low occupancy data sets, however, had high values for χ^2 (12 and 34), indicating significant deviations from the model. These could result from the model for the detection volume or to fluctuations in the laser excitation power.

For the unrestricted fits of the low occupancy data, the occupancies extracted for the dsDNA-Cy3 and Cy5-dsDNA-Cy3 fragments are consistent with the values obtained using the restricted fits. However, the occupancies extracted for the Cy5-dsDNA fragments are significantly smaller (35%-65%). There is a compensating increase in the brightness extracted for these fragments in channel *R*. For the unrestricted fits of the high occupancy data, the occupancies for the Cy5-dsDNA were again smaller (25%-50%), and there were compensating increases in the brightness in channel *R*. The occupancies extracted using the unrestricted fit from the dsDNA-Cy3 and Cy5-dsDNA-Cy3 fragments in sample 10 are different from those obtained with the restricted fit (a 33% decrease and a 160% increase). With the unrestricted fits, the diffusion times

extracted for the Cy5-dsDNA-Cy3 and dsDNA-Cy3 fragments are similar to what is expected from the calculation in section 3.3.3 (451-684 μs compared to 710 μs). The diffusion times for the Cy5-dsDNA fragments tend to be shorter (353-430 μs), again likely due to photobleaching. The consistency found in the brightness values is quite good (typically within 10%; worst case 50%).

These fits show how it is possible to obtain coincidence information, occupancy, brightness, and diffusion time of several sources in an experimental data set through the use of the PAID histogram. Control experiments can be used to restrict values for many parameters, increasing the confidence level in the remaining fitted parameters.

3.5. Conclusion

The PAID histogram is a data presentation and analysis method that allows simultaneous extraction of information about diffusion, brightness, and coincidence between multiple channels from a single data set. The use of the PAID histogram for cross-correlation studies was studied by extracting parameters from simulated data sets using non-linear least squares fitting based on the PAID model. The parameters extracted agreed well with the simulation parameters. A series of experimental data sets was used to extract the same parameters as from the simulations. These fits show how it is possible to obtain coincidence information, occupancy, brightness, and diffusion time of several sources in a data set through the use of the PAID histogram.

The photon-based histogram design used in developing PAID can be pursued further. The one-monitor channel histograms used in this paper can be extended to use two monitor channels to improve sensitivity. Addition of multiple stop channels can extend higher-order correlation functions (useful for investigating non-Markovian properties) to include information on brightness. By performing the FCS experiments in conjunction with time-correlated single photon counting (TCSPC), each photon will be stamped with the sub-nanosecond resolution time delay between the excitation laser pulse and the fluorescence photon. This information can be attached to the start photon, spreading the PAID histogram into the lifetime dimension. The lifetime of the fluorophore can then be tracked as a function of the time interval between the start and stop photons.

The model developed here is flexible, and will be extended to include photophysical properties of the dyes such as triplet state induced blinking, singlet and triplet state saturation, and photobleaching. As pointed in section 3.4.4, an accurate detection volume is critical to the performance of the PAID model. Therefore, it will be important to measure the detection volume and study how this affects the PAID function model. This will improve confidence that any deviations from the fits are due to additional dynamics or sub-populations not assumed in the fit. The model will be extended to account for two monitor channels to take advantage of the improved ability to separate subpopulations. We have only modeled diffusion dynamics up to now. However, conformational dynamics can also be probed using PAID in combination with FRET.

The model developed for PAID assumes that the molecules are diffusing freely in solution. PAID is not limited to this configuration. It can be applied in cellular environments, on immobilized molecules, or in situations with flow. First, however, the application of PAID to monitoring macromolecular interactions for samples freely diffusing in solution will be pursued. Especially important will be a demonstration of the extraction of stoichiometry in a sample that undergoes aggregation or oligomerization, and of the extraction of binding constants.

Appendices

3.A. Bin specification and normalization for PAID histogram

When forming a PAID histogram for the large number of photons obtained in fluorescence fluctuation experiments, it is more meaningful to place events in bins than to make a scatter plot. In choosing the size and spacing of bins, one needs to consider that fluorescence dynamics occur over a large range of time scales. To cover a large range of time scales with a minimum number of histogram bins, logarithmic or quasi-logarithmic time bins are commonly used in FCS experiments. For the PAID histogram, we choose the bins for the time interval τ axis to be logarithmically spaced, with 10 bins per decade. To use a logarithmic scale for the monitor photon axis is more problematic (especially at low photon counts) since the number of monitor photons that arrive is strictly an integer. The clock time resolution Δt can be chosen small enough to make the integer nature of the discrete time interval variable $\tau = \left\lceil \frac{\tau}{\Delta t} \right\rceil$ negligible in the microsecond regime, but this cannot be done with the number of monitor photons counted. Unless one is willing to use a spacing of bins that is extremely sparse (factors of 2,3,4...), the discrete spacing of the number of monitor photons will cause logarithmic bins to be inconsistently occupied at low \mathbf{n} ; some bins may not even have an integer in them. So, we use the quasi-logarithmic scale that is used in the multiple tau correlation technique for the time interval axis instead for the monitor photon count axis [152, 153]. That is, the first 16 bins are evenly spaced with increments of

1, $(\mathbf{n}_1, \dots, \mathbf{n}_{16}) = (0, 1, \dots, 15)$. Then with each set of 8 bins, one doubles the increment. The next 8 bins are $(\mathbf{n}_{17}, \dots, \mathbf{n}_{24}) = (16-17, 18-19, \dots, 30-31)$ with an increment of 2, followed by $(\mathbf{n}_{25}, \dots, \mathbf{n}_{32}) = (32-35, 36-39, \dots, 60-63)$ with an increment of 4, etc. On the large scale these bins are logarithmically spaced, while on the small scale they are linearly spaced. In this way, we can cover a large dynamic range of integers in a consistent manner with a small number of bins.

After placing events in the histogram bins, normalization is necessary to obtain $C_{STM}(\tau, \mathbf{n})$. First, the histogram is multiplied by the factor $\frac{\mathcal{T}}{N_S N_T}$ in Eq. (3.8). Second, for a bin that has time interval axis limits τ_{low} and τ_{high} and monitor photon axis limits that include the integers \mathbf{n}_{low} through \mathbf{n}_{high} , we divide by the size of the bin $(\tau_{\text{high}} - \tau_{\text{low}})(\mathbf{n}_{\text{high}} - \mathbf{n}_{\text{low}} + 1)$. The value for the bin is then an average of $C_{STM}(\tau, \mathbf{n})$ over the bin limits, rather than an integral over the bin limits. This normalizes the histogram, giving us $C_{STM}(\tau, \mathbf{n})$. However, it is not an ideal representation for a logarithmic scale: when plotting a slice of the histogram in the logarithmic scale of the monitor photon count axis, for a constant time interval, we would like the actual area under the curve to correspond to the value of the correlation $C_{ST}(\tau)$. To do this, we approximate the photon monitor variable \mathbf{n} as a continuous variable n , then convert to a logarithmic scale using the expression $\zeta = \log_{10} n$. We want to keep the relation in (3.9) valid in the new variable. We approximate the sums over \mathbf{n} as integrals over a continuous variable n , and convert to the logarithmic variable ζ :

$$\begin{aligned}
C_{ST}(\boldsymbol{\tau}) &= \sum_{\mathbf{n}=0}^{\infty} C_{STM}(\boldsymbol{\tau}, \mathbf{n}) \\
&= \int_0^{\infty} dn C_{STM}(\boldsymbol{\tau}, [n]) \\
&= \int_{-\infty}^{\infty} d\zeta (n \ln 10) C_{STM}(\boldsymbol{\tau}, [n]) \\
&\equiv \int_{-\infty}^{\infty} d\zeta C'_{STM}(\boldsymbol{\tau}, \zeta)
\end{aligned} \tag{3.12}$$

By looking at the differentials, we find that by changing variables from n to ζ we change amplitude of the PAID by a factor $(\ln 10)n$. So, the histogram bins are in addition weighted by a factor of $(\mathbf{n} + 0.5) \ln 10$. We add 0.5 because we consider each bin in n as covering a range between \mathbf{n} and $\mathbf{n} + 1$, and the average over this range is $\mathbf{n} + 0.5$. This only makes a difference at low n , and causes the $n = 0$ bin to be weighted by the factor 0.5 rather than 0.

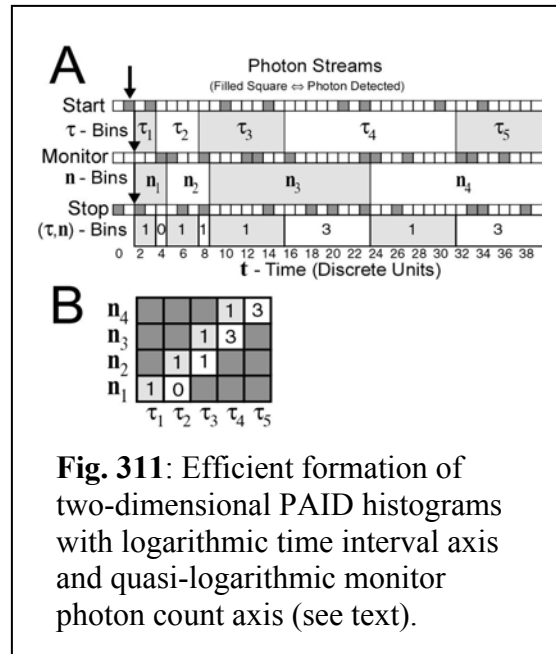
3.B. Algorithms for constructing PAID histograms

For the PAID method to be practical, it is important to use an efficient way to form the PAID histograms from photon streams. The most straightforward algorithm is to compare each photon from the start channel with each photon in the stop channel, then calculate how many monitor photons fall between each start and stop photon. If there are N_s photons in the start channel, and N_T photons in the stop channel, then there are $\sim N_s N_T$ entries into the histogram. This makes the algorithm $O(N^2)$, which prevents the use of a large dynamic range in the PAID histogram. (It is possible to compare only the first stop photons for each start photon, but this would limit the dynamic range.)

A more efficient algorithm can be developed if we take advantage of the logarithmic spacing of the time interval

bins τ_a and the quasi-logarithmic spacing of the monitor photon count bins n_b used in the PAID histogram. The procedure is illustrated in Fig. 3.11. The start, stop, and monitor channel photon streams are shown in Fig. 3.11A. There is a filled square placed at the integer-valued time of arrival of each detected photon, t_i^s . The time

interval and monitor photon count bins corresponding to the first start photon, denoted by the arrow at the top, are shown. The time interval bins, spaced logarithmically with



integer time intervals 2,4,8,16,..., are shown as gray and white bands below the start channel photon stream. The monitor photon count bins, spaced logarithmically with monitor photon counts 1,2,4,... are shown as gray and white bands below the monitor channel photon stream. The gray and white bands below the stop photon channel show how the time interval and monitor photon count bins combine to form the two-dimensional histogram bins. Each bin is labeled with the number of stop photons counted within the bin. These values are then transferred to the two-dimensional PAID histogram in Fig. 3.11B. The procedure to perform this algorithm is as follows:

1. Consider each start photon arrival time t_i^S . Search for the photons in the stop channel and monitor channel that are closest to this time.
2. Set the current time interval (τ) bin to $a_{\text{curr}} = 1$, and the current monitor photon count (n) bin to $b_{\text{curr}} = 1$.
3. Calculate the time interval τ_M at which the monitor channel switches to the next monitor count bin $b_{\text{curr}} + 1$.
4. If this time interval τ_M is less than the time interval of the $(a_{\text{curr}} + 1)^{\text{th}}$ τ bin, perform a binary search on the stop channel to find the photon arriving just after the time τ_M , to determine how many stop photons arrive in the current bin. Add these to the $(a_{\text{curr}}, b_{\text{curr}})$ bin of the histogram, advance $b_{\text{curr}} = b_{\text{curr}} + 1$, and go back to step 3.
5. Otherwise, Perform a binary search on the stop channel to find how many stop photons arrive up to the time of the $(a_{\text{curr}} + 1)^{\text{th}}$ τ bin. Add these to the

$(a_{\text{curr}}, b_{\text{curr}})$ bin of the histogram and advance $a_{\text{curr}} = a_{\text{curr}} + 1$. Go back to step 3, unless there are no more stop photons or $(a_{\text{curr}}, b_{\text{curr}})$ is outside of the histogram.

6. Go back to step 1 unless there are no more start photons.

This algorithm takes advantage of the fact that the start, stop, and monitor channels are ordered lists (each successive photon is at a later time) by performing binary searches. A modified search algorithm that uses increments of increasing size from the initial search index to bracket the desired value before performing a standard binary search was found to be most effective (see description of **hunt** in [154].) Also, because of the logarithmic spacing on both axes, a small number of binary searches can cover a large dynamic range. The algorithm is extendable to multiple monitor channels.

3.C. Development of model for PAID

We develop a model of the PAID function for several species of diffusing molecules with a Poisson background in a tightly focused laser excitation volume. The PAID function is expressible in terms of the photon counting probability distributions and the PAID function for single molecules. The photon count probability distribution and the PAID function for single molecules are expressed in terms of four path integrals, which we estimate using Monte Carlo simulations of diffusion paths. These path integrals need only be calculated once; changes in the diffusion time and brightness parameters can be accounted for by a scaling law. This means that, although the model is not expressed in closed form, it can still be used in a fitting routine.

Precise definitions of the effective detection volume V_{eff} and the brightness per molecule in detector channel A , $q_{\alpha A}$ are needed. As a function of a molecule's spatial position, $\vec{x} = [x, y, z]$, neglecting intersystem crossing to triplet states and assuming that the fluorescence lifetime is zero, the rate of photons $\lambda_{\alpha A}(\vec{x})$ coming from a fluorescent molecule of species α is

$$\lambda_{\alpha A}(\vec{x}) = \sigma_{\alpha} \varphi_{\alpha} I_0 d_{\alpha A} \text{Exc}(\vec{x}) \text{CEF}(\vec{x}). \quad (3.13)$$

I_0 is the excitation intensity at the center of the confocal volume, σ_{α} is the absorption cross-section of the fluorophore, φ_{α} is the quantum efficiency of the fluorophore, and $d_{\alpha A}$ is the detection efficiency at the center of the confocal volume for detector A . These can be grouped into one parameter $q_{\alpha A}^0 = d_{\alpha A} I_0 \sigma_{\alpha} \varphi_{\alpha}$, the brightness at the center of the

confocal volume for detector A . $\text{Exc}(\vec{x})$ is the excitation profile of the laser beam, and $\text{CEF}(\vec{x})$ is the collection efficiency function of the collection optics [145]. If there is more than one laser source, then $\text{Exc}(\vec{x})$ may be different for each. $\text{CEF}(\vec{x})$ in general varies as a function of detection wavelength. For simplicity, we use the same $\text{Exc}(\vec{x})$ and $\text{CEF}(\vec{x})$ for each excitation and each detection wavelength. We will account for these effects in future analyses. The detectivity is defined as the product of the excitation and detection efficiency profiles $\phi(\vec{x}) \equiv \text{Exc}(\vec{x})\text{CEF}(\vec{x})$. For simulations, we assume a Gaussian detectivity, $\phi(\vec{x}) = \exp\left[-2(x^2 + y^2)/\omega^2 - 2z^2/l^2\right]$, where ω is the $1/e^2$ width of the confocal volume in the x and y directions, and l is length of the volume in the z direction. For the experiments, we use the confocal detection volume for the oil immersion objective described in section 3.3.1. With the new definitions, Eq. (3.13) can be written

$$\lambda_{\alpha A}(\vec{x}) = q_{\alpha A}^0 \phi(\vec{x}). \quad (3.14)$$

The brightness per molecule $q_{\alpha A}$ is defined as the average photon count rate in detector channel A over the detection profile $\phi(\vec{x})$,

$$q_{\alpha A} = \frac{\int \lambda_{\alpha A}(\vec{x}) \phi(\vec{x}) dV}{\int \phi(\vec{x}) dV} = q_{\alpha A}^0 \frac{\int \phi^2(\vec{x}) dV}{\int \phi(\vec{x}) dV}, \quad (3.15)$$

where $dV = dx dy dz$ is an infinitesimal volume element. For the Gaussian detection

profile, this equation reduces to $q_{\alpha A} = \frac{q_{\alpha A}^0}{2^{3/2}}$.

The effective detection volume is defined as in [27, 118, 120]:

$$V_{\text{eff}} = \frac{\left[\int \phi(\vec{x}) dV \right]^2}{\int \phi^2(\vec{x}) dV}. \quad (3.16)$$

For the case of the Gaussian detection volume above, this equation becomes $V_{\text{eff}} = \pi^{3/2} \omega^2 l$.

With this definition, Eq. (3.14) is now written

$$\lambda_{\alpha A}(\vec{x}) = (q_{\alpha A} V_{\text{eff}}) \frac{\phi(\vec{x})}{\int \phi(\vec{x}) dV}. \quad (3.17)$$

The occupancy c_α is the average number of molecules of species α within the detection volume. If there are \mathcal{N}_α molecules of the diffusing species $\alpha > 0$ in solution, and the volume of the solution is $\mathcal{V}_{\text{sol}} \gg V_{\text{eff}}$, then the following relationship with the occupancy c_α holds, $\frac{\mathcal{N}_\alpha}{\mathcal{V}_{\text{sol}}} = \frac{c_\alpha}{V_{\text{eff}}}$.

The density of molecules as a function of spatial position for species α is $\rho_\alpha(\vec{x}) = \frac{c_\alpha}{V_{\text{eff}}}$. To calculate the average count rate from diffusing species α , we integrate the density of molecules multiplied by the intensity as a function of spatial position,

$$k_{\alpha A} = \int \rho_\alpha(\vec{x}) \lambda_{\alpha A}(\vec{x}) dV = c_\alpha q_{\alpha A}. \quad (3.18)$$

The average count rate $k_{\alpha A}$ from a diffusing species α in detection channel A is the product of the occupancy c_α and the average brightness $q_{\alpha A}$. The total average count rate in detector A is the sum of the average rate of photons of all species and background

$$k_A \equiv k_{0A} + \sum_{\alpha=1}^N k_{\alpha A}. \quad (3.19)$$

Average intensities are denoted by k , and instantaneous intensities are denoted by λ .

3.C.1. Spatial distribution of molecules upon detection of start photon

The first step in modeling the PAID function is to obtain expressions for the spatial distribution of the fluorescent molecules at the time a start photon is received. At the time a start photon arrives from a diffusing source $\alpha > 0$ (defined as time interval $\tau = 0$), the molecule that emitted the photon is inside the effective detection volume, meaning that the spatial probability distribution for that molecule matches the excitation-detection volume. This can be seen as follows. Consider the intensity in the start detection channel of a molecule of species α as a function of spatial position, $\lambda_{\alpha S}(\vec{x})$, given by Eq.(3.17) while specifying the detector channel $A = S$. The probability that a start photon is received from the molecule at a specific spatial position is directly proportional to the intensity in the start detection channel of the molecule at that position. So, the probability distribution $\mathcal{P}_{\alpha h}^{\text{corr}}(\vec{x})$ for the position of a molecule of species α when it emits a photon can be obtained by dividing the intensity $\lambda_{\alpha S}(\vec{x})$ by its integral over all space,

$$\mathcal{P}_{\alpha}^{\text{corr}}(\vec{x}) = \frac{\lambda_{\alpha S}(\vec{x})}{\int dV \lambda_{\alpha S}(\vec{x})} = \frac{\phi(\vec{x})}{\int dV \phi(\vec{x})}, \quad (3.20)$$

where $dV = dx dy dz$ is an infinitesimal volume element. This expression assumes that there is no triplet state saturation, and that there is no significant diffusion within the fluorescence lifetime. The superscript “corr” means correlated, signifying that the subsequent photons coming from this molecule are correlated with the start photon.

In contrast, the molecules of a diffusing species $\alpha > 0$ that did not emit the start photon are equally likely to be anywhere in the solution at $\tau = 0$, so the probability distribution for these molecules is

$$\mathcal{P}_\alpha^{\text{unc}}(\vec{x}) = \frac{1}{\mathcal{V}_{\text{sol}}}. \quad (3.21)$$

The superscript “unc” means uncorrelated, signifying that the photons coming from these molecules are uncorrelated with the start photon.

3.C.2. Calculation of the cross-correlation

The cross-correlation measures the average rate of photons received in the stop detection channel T upon receiving a photon in the start detection channel S , normalized by the average count rate in the stop detection channel. As the main task in calculating the cross-correlation, we obtain the average rate of receiving stop photons from a source β a time interval τ after receiving a start photon from source α , $k_{\alpha S \rightarrow \beta T}(\tau)$. This is the rate averaged over all possible initial spatial positions as well as all possible later spatial positions. Although this will allow us to calculate the cross-correlation function, it will not allow us to calculate the PAID function without the further development of the theory in the next few sections. To obtain the total density of molecules of a species β at time interval $\tau = 0$, upon receiving a start photon from a molecule of species α , we add the “correlated” and “uncorrelated” components:

$$\rho_{\alpha S \rightarrow \beta}(\vec{x}, \tau = 0) = \mathcal{P}_\alpha^{\text{corr}}(\vec{x}, \tau = 0) \delta(\alpha, \beta) + \mathcal{N}_\beta \mathcal{P}_\beta^{\text{unc}}(\vec{x}, \tau = 0) \quad (3.22)$$

The second term on the right is the contribution of the \mathcal{N}_β molecules of species β that did not emit the photon. If $\alpha = \beta$, then the molecule that emitted the photon gives the contribution indicated in the first term on the right, and there are $\mathcal{N}_\beta - 1$ uncorrelated molecules. Since $\mathcal{N}_\beta \gg 1$, we approximate $\mathcal{N}_\beta - 1 \approx \mathcal{N}_\beta$.

In order to obtain the cross-correlation from this initial distribution, the density of molecules at a later time can be calculated by integration against the Green's function for three-dimensional diffusion of species β [146],

$$g_{\beta}(\vec{x}, \tau | \vec{x}_0) = (4\pi D_{\beta} \tau)^{-3/2} \exp\left[-\frac{(\vec{x} - \vec{x}_0)^2}{4D_{\beta} \tau}\right]. \quad (3.23)$$

The resulting density of molecules as a function of the spatial variables \vec{x} and time interval τ is

$$\rho_{\alpha S \rightarrow \beta}(\vec{x}, \tau) = \int dV_0 \rho_{\alpha S \rightarrow \beta}(\vec{x}_0, \tau = 0) g_{\beta}(\vec{x}, \tau | \vec{x}_0), \quad (3.24)$$

or substituting Eqs. (3.20)-(3.22), and simplifying,

$$\rho_{\alpha S \rightarrow \beta}(\vec{x}, \tau) = \frac{c_{\beta}}{V_{\text{eff}}} + \delta(\alpha, \beta) \frac{\int dV_0 \phi(\vec{x}_0) g_{\beta}(\vec{x}, \tau | \vec{x}_0)}{\int dV_0 \phi(\vec{x}_0)}, \quad (3.25)$$

The total count rate on the stop detector T for photons coming from molecules of species β given that the start photon was from species α , $k_{\alpha S \rightarrow \beta T}(\tau)$, is equal to the integral over space of the number density for molecules of species β multiplied by the intensity in the stop photon stream of a molecule of species β as a function of spatial position $\lambda_{\beta T}(\vec{x})$:

$$k_{\alpha S \rightarrow \beta T}(\tau) = \int dV \rho_{\alpha S \rightarrow \beta}(\vec{x}, \tau) \lambda_{\beta T}(\vec{x}). \quad (3.26)$$

Using Eq. (3.17) and Eq. (3.25), this expression becomes

$$k_{\alpha S \rightarrow \beta T}(\tau) = k_{\beta T} + \delta(\alpha, \beta) q_{\beta T} \frac{\int dV \phi(\vec{x}) \int dV_0 \phi(\vec{x}_0) g_{\beta}(\vec{x}, \tau | \vec{x}_0)}{\int dV \phi^2(\vec{x}_0)}. \quad (3.27)$$

The first term is the contribution of the uncorrelated molecules of species β that did not emit the start photon. The second term is the contribution of the molecule that emitted the photon, if $\alpha = \beta$. This expression is valid for all diffusing species $\alpha, \beta > 0$. If the

start photon came from the background process so that $\alpha = 0$, there is no difference between the count rate at an arbitrary time t and at the moment the start photon is received. So, for $\beta = 0$, the source α of the start photon does not matter,

$$k_{\alpha S \rightarrow 0T}(\tau) = k_{0T} \quad (3.28)$$

For $\beta > 0$, Eq. (3.27) is still valid if the start photon is from the background source, $\alpha = 0$.

Equations (3.27) and (3.28) give us the average count rate in the stop detector channel T given that a photon was received in the start detector channel S from source α . These can be used to calculate the cross-correlation function by summing $k_{\alpha\beta T}(\tau)$ over all sources β , as well as all possible sources α for the start photon. Each term is weighted with the count rate of each source α in the start detector channel S , $k_{\alpha S}$. To normalize the result, we divide by the product of the total count rate in the start channel k_S multiplied by the total count rate in the stop channel k_T , as in Eq. (3.3). This gives us the cross-correlation function for channel S and channel T ,

$$C_{ST}(\tau) = \frac{\sum_{\alpha=0}^M \sum_{\beta=0}^M k_{\alpha S} k_{\alpha S \rightarrow \beta T}(\tau)}{k_S k_T} \quad (3.29)$$

If a Gaussian detection volume is used for the detectivity $\phi(\vec{x})$, the standard formulas for FCS are recovered.

While the above arguments using the density of molecules provide the correlation function, they will not be sufficient to calculate the PAID function $C_{STM}(\mathbf{n}|\tau)$. The initial density of molecules given by Eq. (3.22) is still correct, but the information contained in the density of molecules is not sufficient to determine the distribution of correlation in the

monitor photon count axis \mathbf{n} . To be able to model the PAID function, it is necessary to know the history of the molecules, the possible diffusion paths of the molecules.

3.C.3. Photon count probability distribution for a single path of a single molecule

Before calculating the PAID function, we obtain the photon count probability distribution for the monitor detection channel given that a start photon was received from a molecule of species α at time interval $\tau = 0$. A possible diffusion path l of a molecule in solution is defined by its spatial position as a function of time interval τ , $\vec{x}_l(\tau) = [x_l(\tau), y_l(\tau), z_l(\tau)]$. S is defined as the set of all possible paths l from all starting positions at time interval $\tau = 0$ to all ending positions at time interval τ . At time interval $\tau = 0$, the probability distribution for the initial position is given by Eq. (3.20) for the molecule from species α that emitted the start photon $\mathcal{P}(\vec{x}_l(0)) = \mathcal{P}_\alpha^{\text{corr}}(\vec{x}_l(0))$ and by Eq. (3.21) for the molecules of species β that did not, $\mathcal{P}(\vec{x}_l(0)) = \mathcal{P}_\beta^{\text{unc}}(\vec{x}_l(0))$. Each of the expressions for photon count probability distributions in this section and the following section can be applied to both correlated and uncorrelated molecules, so we omit the superscript “corr” or “unc”. When we discuss the combination of the distributions of all molecules, these superscripts will be present. For species β , the probability for the whole path up to time interval τ is given by the following expression (following Eq. 8 in [155]):

$$\begin{aligned} \mathcal{P}_\beta(l|\tau) &= \lim_{\Delta\tau \rightarrow 0} \left(\prod_{h=0}^{\tau/\Delta\tau} \int_{dV} \frac{d\vec{x}_l}{(4\pi D_\beta \Delta\tau)^{3/2}} \right) \mathcal{P}(\vec{x}_l(0)) \exp \left\{ -\frac{[\vec{x}_l^{h+1} - \vec{x}_l^h]^2}{4D_\beta \Delta\tau} \right\} \\ &= \mathcal{P}(\vec{x}_l(0)) \exp \left\{ -\int d\tau \frac{[\dot{\vec{x}}_l(\tau)]^2}{4D_\beta} \right\} \end{aligned} \quad (3.30)$$

To specify that correlated paths are used, we add a superscript “corr”. To specify that uncorrelated paths are used, we add instead a superscript “unc”. The probability for the path l is obtained by multiplying the probability density for the initial position by the transition probability to every subsequent position spaced by a time interval $\Delta\tau$. The transition probability is the Green’s function for three-dimensional diffusion given in Eq. (3.23).

The intensity in the monitor detector channel M for the molecule of species β as a function of time is found using Eq.(3.17),

$$\lambda_{\beta Ml}(\tau) = \lambda_{\beta M} [\vec{x}_l(\tau)]. \quad (3.31)$$

This expression translates, for a path l , a diffusion path into an intensity path. Note that this expression gives the instantaneous intensity at the spatial positions along a diffusion path, not the intensity averaged over all possible spatial positions as was used in the previous section.

For a given path l of one molecule, the probability that \mathbf{n} photons have been received at a time interval τ in detection channel M is ${}^1P_{\beta Ml}(\mathbf{n}|\tau)$. The 1 indicates that it is for a single molecule. We take a differential equation-based approach to obtain the distribution of photon counts, modified from [156], which contains the same information as the approach in [157]. The differential equation governing the time evolution of ${}^1P_{\beta Ml}(\mathbf{n}|\tau)$ is:

$$\frac{\partial {}^1P_{\beta Ml}(\mathbf{n}|\tau)}{\partial \tau} = \lambda_{\beta Ml}(\tau) {}^1P_{\beta Ml}(\mathbf{n}-1|\tau) - \lambda_{\beta Ml}(\tau) {}^1P_{\beta Ml}(\mathbf{n}|\tau). \quad (3.32)$$

This equation gives the rate of change in the probability that \mathbf{n} photons have been detected at a time τ . The first term on the right gives the increase in this probability due

to a photon detected when $\mathbf{n}-1$ had previously been received. The rate of such photons is given by multiplying the total count rate $\lambda_{\beta MI}(\tau)$ by the probability to have detected $\mathbf{n}-1$ photons, ${}^1P_{\beta MI}(\mathbf{n}-1|\tau)$. The second term gives the decrease in the probability to have detected \mathbf{n} photons due to a photon detected when \mathbf{n} had previously been detected. The rate of such photons is given by multiplying the total count rate $\lambda_{\beta MI}(\tau)$ by the probability to have detected \mathbf{n} photons, ${}^1P_{\beta MI}(\mathbf{n}|\tau)$. The initial conditions are ${}^1P_{\beta MI}(\mathbf{n}=0|\tau=0)=1$, and ${}^1P_{\beta MI}(\mathbf{n}|\tau=0)=0$ for all $\mathbf{n} \neq 0$. Equation (3.32) is an infinite series of coupled first order differential equations. By solving these equations using, for example, the generating function ${}^1G_{\beta MI}(s|\tau) = \sum_{\mathbf{n}=0}^{\infty} s^{\mathbf{n}} {}^1P_{\beta MI}(\mathbf{n}|\tau)$ we obtain the Poisson distribution:

$$\begin{aligned} {}^1P_{\beta MI}(\mathbf{n}|\tau) &= \exp[-\Lambda_{\beta MI}(\tau)] \frac{[\Lambda_{\beta MI}(\tau)]^{\mathbf{n}}}{\mathbf{n}!} \\ &\equiv \text{Poi}(\Lambda_{\beta MI}(\tau), \mathbf{n}), \end{aligned} \quad (3.33)$$

where we call

$$\Lambda_{\beta MI}(\tau) \equiv \int_0^{\tau} \lambda_{\beta MI}(\tau') d\tau' \quad (3.34)$$

the cumulative intensity. The photon count probability distribution at a time τ for a particular path depends only on the cumulative intensity $\Lambda_{\beta MI}(\tau)$, which depends on the history of the intensity path in a way not seen with the cross-correlation in the previous section. There, the evolution of the instantaneous spatial probability distribution was sufficient to calculate the correlation function. Here, we need to know not only the

probability distribution for where the molecules are at the time interval τ , but where they have been since the start photon was detected.

3.C.4. Photon count probability distribution for all paths of a single molecule

When all possible intensity paths are taken into account, the photon counting probability distribution for a molecule of species β , ${}^1P_{\beta M}(\mathbf{n}|\tau)$, is a weighted average over all paths of the photon counting probability distribution ${}^1P_{\beta MI}(\mathbf{n}|\tau)$,

$${}^1P_{\beta M}(\mathbf{n}|\tau) = \int_S \mathcal{D}(l) \mathcal{P}_\beta(l|\tau) {}^1P_{\beta MI}(\mathbf{n}|\tau) \quad (3.35)$$

$\mathcal{P}_\beta(l|\tau)$ is given by Eq. (3.30), and S is the set of paths from all initial positions to all final positions after a time interval τ . The only variable in ${}^1P_{\beta MI}(\mathbf{n}|\tau)$ that depends on the path is the value $\Lambda_{\beta MI}(\tau)$, given by Eqs. (3.31) and (3.34). So, the path integral can be recast in terms of a simple integral of ${}^1P_{\beta MI}(\mathbf{n}|\tau) = \text{Poi}(\Lambda_{\beta MI}(\tau), \mathbf{n})$ against the probability for a given value of $\Lambda_{\beta MI}(\tau)$,

$${}^1P_{\beta M}(\mathbf{n}|\tau) = \int_0^\infty d\Lambda {}^1\tilde{P}_{\beta M}(\Lambda|\tau) \text{Poi}(\Lambda, \mathbf{n}) \quad (3.36)$$

The expression ${}^1P_{\beta M}(\mathbf{n}|\tau)$ is the Poisson transform of ${}^1\tilde{P}_{\beta M}(\Lambda|\tau)$. There are two possible spaces to work in, the photon count \mathbf{n} -space and the cumulative intensity Λ -space. Functions in Λ space are denoted with a tilde. The probability density ${}^1\tilde{P}_{\beta M}(\Lambda|\tau)$ is given by the expression

$${}^1\tilde{P}_{\beta M}(\Lambda|\tau) = \int_S \mathcal{D}(l) \mathcal{P}_\beta(l|\tau) \delta(\Lambda - \Lambda_{\beta MI}(\tau)) \quad (3.37)$$

This is the probability density, considering all possible paths, to have a particular value of the cumulative intensity Λ at a time interval τ . We approximate this integral later using Monte Carlo sampling of possible diffusion paths. (NOTE: this function ${}^1\tilde{P}_{\beta M}(\Lambda|\tau)$ corresponds to the probability density $\mathcal{P}(E)$ in [158]). The function ${}^1\tilde{P}_{\beta M}(\Lambda|\tau)$ depends on the diffusion time τ_β^D and brightness $q_{\beta M}$ of each species. Working in Λ space is advantageous because changes in the brightness and diffusion time parameters for the species β can be taken into account by scaling in the appropriate dimensions. A change in $q_{\beta M}$ corresponds to a scaling in the Λ dimension since $\Lambda_{\beta M}(\tau)$ is directly proportional to $q_{\beta M}$. A change in τ_β^D corresponds to scaling in both the Λ and τ dimensions. The diffusion time enters the model only as a product of the form $D_\sigma \Delta \tau$ (see Eq. (3.30)). A scaling in the time interval τ axis accounts for a change in diffusion time in that expression. The scaling in Λ is also necessary since $\Lambda_{\beta M}(\tau)$ is a cumulative integral over time which increases proportionally with a scaling in the time interval axis. If ${}^1\tilde{P}_{\sigma M}(\Lambda|\tau)$ is computed for a standard species σ with the diffusion time τ_σ^D and brightness $q_{\sigma M}$, then for a different species β with diffusion time τ_β^D and brightness $q_{\beta M}$, we have the scaling law

$${}^1\tilde{P}_{\beta M}(\Lambda|\tau) = {}^1\tilde{P}_{\sigma M}\left(\Lambda \frac{\tau_\sigma^D q_{\sigma M}}{\tau_\beta^D q_{\beta M}} \middle| \tau \frac{\tau_\sigma^D}{\tau_\beta^D}\right) \quad (3.38)$$

So, if one calculates ${}^1\tilde{P}_{\sigma M}^{\text{corr}}(\Lambda|\tau)$ for the molecule that emitted the start photon, and ${}^1\tilde{P}_{\sigma M}^{\text{unc}}(\Lambda|\tau)$ for the molecules that did not, any differences in diffusion time and brightness between molecular species can be calculated using the scaling law.

For the background source $\beta=0$, assumed to be a pure Poisson source with intensity k_{0M} in the monitor detection channel, the photon count probability distribution is

$$P_{0M}(\mathbf{n}|\tau) = \text{Poi}(k_{0M}\tau, \mathbf{n}) \quad (3.39)$$

In Λ -space, this is

$$\tilde{P}_{0M}(\Lambda|\tau) = \delta(\Lambda - k_{0M}\tau) \quad (3.40)$$

3.C.5. Photon count probability distribution for all molecules in solution

We combine the photon count probability distributions for single molecules to obtain the photon count probability distribution for all molecules in solution. The molecules are assumed to be non-interacting (at least within the diffusion time), so we assume independence when we combine the photon count distributions. This means that the photon count distribution for the combined source of all molecules and background is the convolution of the photon count distributions for all molecules and background (See appendix 3.E). The photon count distribution of probability for all molecules in solution given that molecule $h=1$ of species α emitted a start photon is then,

$$P_{\alpha M}(\mathbf{n}|\tau) = \left(P_{0M} * {}^1P_{\alpha M}^{\text{corr}} * \prod_{\beta=1}^F ({}^1P_{1M}^{\text{unc}})^{\mathcal{N}_{\beta} - \delta(\alpha, \beta)} \right) (\mathbf{n}|\tau) \quad (3.41)$$

Note that the symbol for convolution $*$ is inside the parentheses, indicating repeated convolutions rather than products. This is the convolution of the distributions for the

background, the molecule that emitted the start photon, and all the other molecules starting with species $\beta=1$, all the way up to $\beta=F$. If the start photon came from the background $\alpha=0$, then $P_{\alpha 1M}^{\text{corr}}$ is removed from the above successive convolutions. For $\alpha=\beta$, there are $\mathcal{N}_\alpha-1$ convolutions for the uncorrelated molecules, since one of molecules emitted the photon and is taken into account by ${}^1P_{\alpha M}^{\text{corr}}$. As shown in appendix 3.F, these convolutions can be performed equivalently in Λ -space and \mathbf{n} space. To convert Eq. (3.41) to Λ -space, replace each \mathbf{n} with a Λ , and place a tilde over each quantity \tilde{P} ,

$$\tilde{P}_{\alpha M}(\Lambda|\tau) = \left(\tilde{P}_{0M} * {}^1\tilde{P}_{\alpha M}^{\text{corr}} * \prod_{\beta=1}^F \left({}^1\tilde{P}_{1M}^{\text{unc}} * \right)^{\mathcal{N}_\beta - \delta(\alpha, \beta)} \right) (\Lambda|\tau) \quad (3.42)$$

To obtain the photon count probability distribution for an arbitrary start photon, we sum over all possible sources α of the start photon,

$$P_M(\mathbf{n}|\tau) = \sum_{\alpha=1}^F \frac{k_{\alpha S}}{k_S} P_{\alpha M}(\mathbf{n}|\tau) \quad (3.43)$$

The weighting factor $\frac{k_{\alpha S}}{k_S}$ is the probability that the start photon came from source α .

FIMDA uses a series of photon counting histograms with different time bin widths to extract the occupancy, diffusion time, and brightness of several diffusing species simultaneously. A modification of Eq. (3.41) can be used to model the FIMDA histogram. In PAID, a photon is received at the start of each counting interval. Because of this, there is a distinction between correlated and uncorrelated molecules. However, in FIMDA, the start of the counting interval is uncorrelated with the photon sequence. If we remove the correlated photon count distribution in Eq. (3.41), we obtain a model for the

FIMDA histogram. The single-molecule photon count distributions used in this model are calculated as described above.

3.C.6. Photon count distribution of stop channel intensity for a single molecule in solution

To model the PAID function, we will combine the expressions for the photon count distribution with the cross-correlation given in the previous sections. The primary task is to calculate the distribution of the intensity in the stop detection channel T over the monitor photon count variable \mathbf{n} at a time interval τ , $k_{\alpha S \rightarrow \beta TM}(\mathbf{n}|\tau)$, given that a start photon was received from source α at time interval $\tau = 0$. This distribution, $k_{\alpha S \rightarrow \beta TM}(\mathbf{n}|\tau)$, is related to the PAID function considering only a single species β by a constant factor: a normalization is applied to $k_{\alpha S \rightarrow \beta TM}(\mathbf{n}|\tau)$, similar to Eq. (3.29),

$${}^1C_{STM}(\mathbf{n}|\tau) = \frac{k_{\alpha S} k_{\alpha S \rightarrow \beta TM}(\mathbf{n}|\tau)}{k_S k_T}.$$

For a single path l of a molecule from source β , the monitor photon count distribution of the stop channel intensity is calculated by multiplying the rate in the stop channel by the probability to have received \mathbf{n} monitor photons,

$${}^1k_{\beta MTl}(\mathbf{n}|\tau) = {}^1P_{\beta MI}(\mathbf{n}|\tau) \lambda_{\beta TI}(\tau) \quad (3.44)$$

The superscript 1 indicates that the expression is for a single molecule. As a function of time interval τ , the total intensity in the stop channel is $\lambda_{\beta TI}(\tau)$. ${}^1k_{\beta MTl}(\mathbf{n}|\tau)$ is how this intensity is on average divided up among the different values of the monitor photon counts \mathbf{n} .

When all possible paths are taken into account, the monitor photon count distribution of the stop channel intensity for a single molecule of species β , ${}^1k_{\beta MT}(\mathbf{n}|\tau)$, is a weighted average over all paths of the distribution for a single path ${}^1k_{\beta MTl}(\mathbf{n}|\tau)$,

$${}^1k_{\beta MT}(\mathbf{n}|\tau) = \int_S \mathcal{D}(l) \mathcal{P}_\beta(l|\tau) {}^1P_{\beta MI}(\mathbf{n}|\tau) \lambda_{\beta TI}(\tau) \quad (3.45)$$

As in Eq. (3.37), $\mathcal{P}_\beta(l|\tau)$ is given by Eq. (3.30), and S is the set of paths from all initial positions to all final positions after a time interval τ . We can rewrite Eq. (3.45) as an integration of the Poisson distribution against the contribution to the stop channel intensity for a given value of cumulative intensity Λ ,

$${}^1k_{\beta MT}(\mathbf{n}|\tau) = \int_0^\infty d\Lambda {}^1\tilde{k}_{\beta MT}(\Lambda|\tau) \text{Poi}(\Lambda, \mathbf{n}) \quad (3.46)$$

where

$${}^1\tilde{k}_{\beta MT}(\Lambda|\tau) = \int_S \mathcal{D}(l) \mathcal{P}_\beta(l|\tau) \lambda_{\beta TI}(\tau) \delta(\Lambda - \Lambda_{\beta MI}(\tau)) \quad (3.47)$$

The difference between this equation and Eq. (3.37) is the additional factor of the intensity in the stop channel of the path l , $\lambda_{\beta TI}(\tau)$. Because of this factor, Eq. (3.47) gives the cumulative intensity distribution of the stop channel intensity, rather than the cumulative intensity distribution of probability.

The scaling law in Eq. (3.38) also applies here, with one additional factor, the brightness in the stop detector channel $q_{\beta T}$. If ${}^1\tilde{k}_{\sigma MT}(\Lambda|\tau)$ is computed for a standard species σ with the diffusion time τ_σ^D and brightness $q_{\sigma M}$ in the monitor channel and brightness $q_{\sigma T}$ in the stop channel, then for a different species β with diffusion time τ_β^D ,

brightness $q_{\beta M}$ in the monitor channel and brightness $q_{\beta T}$ in the stop channel, we have the following scaling law

$${}^1\tilde{k}_{\beta MT}(\Lambda|\tau) = \frac{q_{\beta T}}{q_{\sigma T}} {}^1\tilde{k}_{\sigma MT} \left(\Lambda \frac{\tau_{\sigma}^D q_{\sigma M}}{\tau_{\beta}^D q_{\beta M}} \middle| \tau \frac{\tau_{\sigma}^D}{\tau_{\beta}^D} \right) \quad (3.48)$$

As with the cumulative intensity probability distribution in Eq. (3.37), one evaluation of the cumulative intensity distribution of the stop channel intensity is made for the molecule that emitted the start photon, ${}^1\tilde{k}_{\beta MT}^{\text{corr}}(\Lambda|\tau)$, and one for the molecules that did not, ${}^1\tilde{k}_{\beta MT}^{\text{unc}}(\Lambda|\tau)$. Any changes in the parameters τ_{β}^D , $q_{\beta M}$, and $q_{\beta T}$ can be taken into account by using the scaling law.

For the background source $\beta = 0$, assumed to be a pure Poisson source with intensity k_{0M} in the monitor detection channel and intensity k_{0T} in the stop detection channel, the photon count distribution of stop channel intensity is

$$k_{0MT}(\mathbf{n}|\tau) = k_{0T} \text{Poi}(k_{0M}\tau, \mathbf{n}) \quad (3.49)$$

In Λ -space this becomes,

$$\tilde{k}_{0M}(\Lambda|\tau) = k_{0T} \delta(\Lambda - k_{0M}\tau) \quad (3.50)$$

3.C.7. PAID function for all molecules in solution

To account for all of the other molecules in solution, ${}^1k_{\beta MT}(\mathbf{n}|\tau)$ is convolved with the photon count probability distribution for all other molecules and background (see appendix 3.E). If the molecule in question emitted the start photon, then

$$k_{\alpha S \rightarrow \beta MT}^{\text{corr}}(\mathbf{n}|\tau) = \delta(\alpha, \beta) \left(P_{0M} * {}^1k_{\alpha MT}^{\text{corr}} * \prod_{\gamma=1}^F \left({}^1P_{\gamma M}^{\text{unc}} \right)^{\mathcal{N}_{\gamma} - \delta(\alpha, \gamma)} \right) (\mathbf{n}|\tau) \quad (3.51)$$

The first factor is the background photon count probability distribution. The second factor is the monitor photon count distribution of stop channel intensity for the molecule that emitted the start photon. The rest of the factors come from the molecules of all the species that did not emit the photon. These are successive convolutions, not products, as indicated by the star $*$ inside the parentheses. For $\alpha = \gamma$, there are $\mathcal{N}_\alpha - 1$ convolutions for the uncorrelated molecules, since one of molecules emitted the photon and is taken into account by ${}^1k_{\alpha MT}^{\text{corr}}$.

If the molecule in question did not emit the start photon, then

$$k_{\alpha S \rightarrow \beta MT}^{\text{unc}}(\mathbf{n}|\tau) = \left(\mathcal{N}_\beta - \delta(\alpha, \beta) \right) \left(P_{0M} * {}^1P_{\alpha MT}^{\text{corr}} * {}^1k_{\beta MT}^{\text{unc}} * \prod_{\gamma=1}^F \left({}^1P_{\gamma M}^{\text{unc}} * \right)^{\mathcal{N}_\gamma - \delta(\alpha, \gamma) - \delta(\beta, \gamma)} \right) (\mathbf{n}|\tau) \quad (3.52)$$

The pre-factor is how many molecules of species β there are in solution. The first convolved factor is the background photon count probability distribution. The second convolved factor is the monitor photon count probability distribution for the molecule that emitted the start photon. The third convolved factor is the monitor photon count distribution of stop channel intensity for the molecule of species β that did not emit the start photon. The rest of the convolved factors come from the molecules of all the species that did not emit the photon. For $\alpha = \gamma$, there is one less convolution for the uncorrelated molecules, since one of molecules emitted the photon and is taken into account by ${}^1P_{\alpha MT}^{\text{corr}}$. For $\beta = \gamma$, there is one less convolution for the uncorrelated molecules, since one of molecules is the one whose intensity is being calculated and is taken into account with ${}^1k_{\beta MT}^{\text{unc}}$.

For the background,

$$k_{\alpha S \rightarrow 0MT}(\mathbf{n}|\tau) = \left(k_{0M} * {}^1P_{\alpha MT}^{\text{corr}} * \prod_{\gamma=1}^F ({}^1P_{\gamma M}^{\text{unc}} *)^{\mathcal{N}_{\gamma} - \delta(\alpha, \gamma)} \right) (\mathbf{n}|\tau) \quad (3.53)$$

The first factor is the monitor photon count distribution of stop channel intensity for the background. The second factor is the monitor photon count probability distribution for the molecule that emitted the start photon. The rest of the factors come from the molecules of all the species that did not emit the photon. For $\alpha = \gamma$, there is one less convolution for the uncorrelated molecules, since one of molecules emitted the photon and is taken into account by ${}^1P_{\alpha MT}^{\text{corr}}$.

We now sum the contributions to $k_{\alpha S \rightarrow \beta TM}(\mathbf{n}|\tau)$ of all molecules, obtaining,

$$k_{\alpha S \rightarrow \beta TM}(\mathbf{n}|\tau) = k_{\alpha S \rightarrow \beta TM}^{\text{corr}}(\mathbf{n}|\tau) + k_{\alpha S \rightarrow \beta TM}^{\text{unc}}(\mathbf{n}|\tau) \quad (3.54)$$

The first term on the right is for any contribution that is correlated with the start photon, and the second term is for the contribution that is uncorrelated with the start photon. To obtain the final expression for the PAID function, we sum over all possible sources α of the start photon, weighted by the intensity of each source in the start channel, just as with the cross-correlation. To normalize the result, we divide by the product of the total count rate in the start channel k_S multiplied by the total count rate in the stop channel k_T , as in Eq.(3.29).

$$C_{STM}(\mathbf{n}|\tau) = \frac{\sum_{\alpha=0}^M \sum_{\beta=0}^M k_{\alpha S} k_{\alpha S \rightarrow \beta TM}(\mathbf{n}|\tau)}{k_S k_T} \quad (3.55)$$

Remember, to convert any of the \mathbf{n} -space expressions to Λ -space, replace each \mathbf{n} with a Λ , and place a tilde over each quantity \tilde{P} or \tilde{k} . This is the final expression for the PAID function. It is calculated by adjusting the distributions ${}^1\tilde{P}_{\beta M}^{\text{unc}}(\Lambda|\tau)$, ${}^1\tilde{k}_{\beta MT}^{\text{unc}}(\Lambda|\tau)$,

${}^1\tilde{\mathbf{P}}_{\beta M}^{\text{corr}}(\Lambda|\tau)$ and ${}^1\tilde{k}_{\beta MT}^{\text{corr}}(\Lambda|\tau)$ for the parameters of each species β , and using Eqs. (3.51)-(3.55). In appendix 3.D, we will describe in more detail how to calculate the PAID function practically.

3.D. Implementation of the model

3.D.1. Evaluation of kernels for model

The distributions ${}^1\tilde{P}_{\sigma M}^{\text{unc}}(\Lambda|\tau)$, ${}^1\tilde{k}_{\sigma MT}^{\text{unc}}(\Lambda|\tau)$, ${}^1\tilde{P}_{\sigma M}^{\text{corr}}(\Lambda|\tau)$ and ${}^1\tilde{k}_{\sigma MT}^{\text{corr}}(\Lambda|\tau)$ for the standard species σ are evaluated using Monte Carlo generation of possible diffusion paths l , a modification of the simulations described in section 3.3.1. The standard species has a diffusion time $\tau_{\sigma}^D = 1$, a brightness $q_{\sigma M} = 1$ in the monitor channel and brightness $q_{\sigma T} = 1$ in the stop channel (each of these has arbitrary units.) As in the previous section, a diffusion path l is simulated by a series of three-dimensional random distance steps, with mean $\mu = 0$ and standard deviation $\sigma = \sqrt{2D\Delta\tau}$, where D is the diffusion constant and $\Delta\tau = 10^{-2} \tau_{\sigma}^D$ is the time interval step. The initial positions are drawn from a uniform distribution across the simulation box $\mathcal{P}(\vec{x}_l(0)) = \frac{1}{V_{\text{box}}}$ for the uncorrelated molecules, and from the detection profile $\mathcal{P}(\vec{x}_l(0)) = \mathcal{P}_{\sigma}^{\text{corr}}(\vec{x}_l(0))$ for the correlated molecules. The uncorrelated distributions are formed from simulations restricted to a finite box of size V_{box} with periodic boundary conditions. Since the probability density for the initial uncorrelated spatial position is a constant with respect to spatial position, the size of the simulation box must be restricted to have a significant number of diffusion-driven crossings of the detection volume. The periodic boundary conditions are necessary to avoid a drain in the number of the molecules from the simulation box. For the correlated distribution, there is no restriction on the simulation box size. The probability density for

the initial correlated spatial position is restricted to the detection volume, and the exit of the molecule from the region of the detection volume causes the average number of molecules per detection volume to return its uncorrelated value. For the species σ , the joint probability for the whole path up to time interval τ is given by the following expression (Eq. (3.30) without the limit):

$$\mathcal{P}_\sigma(l|\tau) = \left(\prod_{h=0}^{\tau/\Delta\tau} \int_{dV} \frac{d\vec{x}_l}{(4\pi D_\sigma \Delta\tau)^{3/2}} \right) \mathcal{P}(\vec{x}_l(0)) \exp \left\{ -\frac{[\vec{x}_l^{h+1} - \vec{x}_l^h]^2}{4D_\sigma \Delta\tau} \right\} \quad (3.56)$$

The distributions are evaluated at a series of time intervals τ that is logarithmically spaced over 10 decades from $\tau = 10^{-6} \tau_\sigma^D$ to $\tau = 10^4 \tau_\sigma^D$ with 100 bins per decade. The cumulative intensity Λ bins are logarithmically spaced over 10 decades from $\Lambda = 10^{-6} q_{\sigma M} \tau_\sigma^D$ to $\Lambda = 10^4 q_{\sigma M} \tau_\sigma^D$ with 10 bins per decade. At each time interval τ in the logarithmically spaced series, the cumulative intensity $\Lambda_{\sigma MI}(\tau) \equiv \int_0^\tau \lambda_{\sigma MI}(\tau') d\tau'$ and the intensity in the stop channel $\lambda_{\sigma TI}(\tau)$ are evaluated. An entry of 1 is entered at the corresponding (τ, Λ) bin in the cumulative intensity probability distribution, ${}^1\tilde{\mathbf{P}}_{\sigma M}^{\text{corr}}(\Lambda|\tau)$ or ${}^1\tilde{\mathbf{P}}_{\sigma M}^{\text{unc}}(\Lambda|\tau)$. Also, an entry $\lambda_{\sigma TI}(\tau)$ is added to the corresponding (τ, Λ) bin in the cumulative intensity distribution of stop channel intensity, ${}^1\tilde{\mathbf{k}}_{\sigma MT}^{\text{corr}}(\Lambda|\tau)$ or ${}^1\tilde{\mathbf{k}}_{\sigma MT}^{\text{unc}}(\Lambda|\tau)$. After simulating a total of 10^5 paths in the correlated case, and 10^7 paths in the uncorrelated case, the estimated distributions are divided by the number of paths used. In the uncorrelated case, there are actually only 10^4 diffusion paths simulated. Each diffusion path is used with 10^3 evenly spaced starting points to give a total of 10^7 effective paths. We can use many different starting points in this case

because the molecules are uncorrelated: there are no special properties of the initial position.

3.D.2. Implementation of the model and fitting routine

We now summarize how we in practice calculate the PAID function for a given set of parameters for F diffusing species and background: the diffusion time τ_α^D , the occupancy c_α , the brightness per molecule $q_{\alpha A}$, and the background intensity q_{0A} . For each species β , we calculate the single molecule cumulative intensity distributions of probability and stop channel intensity for both the correlated and uncorrelated initial positions. We use Eq. (3.38) to calculate ${}^1\tilde{P}_{\beta M}^{\text{corr}}(\Lambda|\tau)$ and ${}^1\tilde{P}_{\beta M}^{\text{unc}}(\Lambda|\tau)$ and use Eq. (3.48) to calculate ${}^1\tilde{k}_{\beta MT}^{\text{corr}}(\Lambda|\tau)$ and ${}^1\tilde{k}_{\beta MT}^{\text{unc}}(\Lambda|\tau)$ from the distributions estimated for the standard set of parameters. In this way, the diffusion time of each species τ_β^D , brightness in the monitor channel $q_{\beta M}$, and brightness in the stop channel $q_{\beta T}$ are all accounted for.

In building up the PAID function $C_{STM}(\mathbf{n}|\tau)$ from these initial distributions, many convolutions are necessary. In order to perform them quickly, we have developed an efficient algorithm to compute convolutions in a quasi-logarithmic scale (see appendix 3.H). ${}^1\tilde{P}_{\beta M}^{\text{unc}}(\Lambda|\tau)$, ${}^1\tilde{k}_{\beta MT}^{\text{unc}}(\Lambda|\tau)$, ${}^1\tilde{P}_{\beta M}^{\text{corr}}(\Lambda|\tau)$ and ${}^1\tilde{k}_{\beta MT}^{\text{corr}}(\Lambda|\tau)$ are rebinned into the quasi-logarithmic scale described in appendix 3.H, and the convolutions are performed in Λ -space.

Now, we use Eqs. (3.51)-(3.54) to calculate the monitor photon count distributions of stop channel intensity for all of the categories of molecules. For each

diffusing species $\beta > 0$, there is a distribution for the correlated and uncorrelated molecules.

The simulations used to form the distributions ${}^1\tilde{P}_{\beta M}^{\text{corr}}(\Lambda|\tau)$ and ${}^1\tilde{k}_{\beta MT}^{\text{corr}}(\Lambda|\tau)$ for correlated initial positions are not restricted to a finite simulation box. Initially, the molecules are inside the detection volume, but the molecules are allowed to diffuse out of the detection volume without restriction as the simulation time passes. Because the size of the simulation box is unrestricted, the difference between \mathcal{N}_γ and $\mathcal{N}_\gamma - \delta(\alpha, \gamma)$ is ignored: in Eqs. (3.51)-(3.54), the expression $\delta(\alpha, \gamma)$ is dropped.

The simulations used to form the distributions ${}^1\tilde{P}_{\beta M}^{\text{unc}}(\Lambda|\tau)$ and ${}^1\tilde{k}_{\beta MT}^{\text{unc}}(\Lambda|\tau)$ for uncorrelated initial positions are restricted to a box with a volume V_{box} , which is larger than the effective detection volume: $V_{\text{box}} \gg V_{\text{eff}}$. The box has harmonic boundary conditions, so that a molecule that comes out of one side reenters the other side. The fundamental concentration for the distributions formed from these simulations is $\frac{1}{V_{\text{box}}}$.

Successive convolution of the distribution ${}^1\tilde{P}_{\beta M}^{\text{unc}}(\Lambda|\tau)$ models an increasing concentration, but only in discrete steps. If the number of uncorrelated molecules of species β inside this box is $N_{\text{box},\beta}$, then we model the uncorrelated photon count probability distribution using $\left({}^1\tilde{P}_{\beta M}^{\text{unc}}(\Lambda|\tau) * \right)^{N_{\text{box},\beta}}$. To have the proper occupancy, then the following relation should be satisfied,

$$\frac{N_{\text{box},\beta}}{V_{\text{box}}} = \frac{\mathcal{N}_\beta}{\mathcal{V}_{\text{sol}}} = \frac{c_\beta}{V_{\text{eff}}}. \quad (3.57)$$

Because the volume of the simulation box used for the distributions for uncorrelated molecules is much smaller than the volume of solution, the distributions ${}^1\tilde{\mathbf{P}}_{\beta M}^{\text{unc}}(\Lambda|\tau)$ and ${}^1\tilde{k}_{\beta MT}^{\text{unc}}(\Lambda|\tau)$ account for a much larger concentration than in section 3.2.6, $\frac{1}{V_{\text{box}}}$ rather than $\frac{1}{V_{\text{sol}}}$. To obtain the proper occupancy, the number of molecules N_{β} in Eqs. (3.51)-(3.54) is replaced by the number of molecules in the simulation box, $N_{\text{box},\beta}$. Using the small box size V_{box} for the uncorrelated molecules and the large box size V_{sol} for the correlated molecules, Eq. (3.51), which is for correlated molecules, is rewritten in Λ -space,

$$\tilde{k}_{\alpha S \rightarrow \beta MT}^{\text{corr}}(\Lambda|\tau) = \delta(\alpha, \beta) \left(\tilde{\mathbf{P}}_{0M} * {}^1\tilde{k}_{\alpha MT}^{\text{corr}} * \prod_{\gamma=1}^F \left({}^1\tilde{\mathbf{P}}_{\gamma M}^{\text{unc}} * \right)^{N_{\text{box},\gamma}} \right) (\Lambda|\tau) \quad (3.58)$$

Equation (3.52), which is for the uncorrelated molecules, is rewritten

$$\tilde{k}_{\alpha S \rightarrow \beta MT}^{\text{unc}}(\Lambda|\tau) = N_{\text{box},\beta} \left(\tilde{\mathbf{P}}_{0M} * {}^1\tilde{\mathbf{P}}_{\alpha MT}^{\text{corr}} * {}^1\tilde{k}_{\beta MT}^{\text{unc}} * \prod_{\gamma=1}^F \left({}^1\tilde{\mathbf{P}}_{\gamma M}^{\text{unc}} * \right)^{N_{\text{box},\gamma} - \delta(\beta, \gamma)} \right) (\Lambda|\tau) \quad (3.59)$$

Equation (3.53), which is for the background, is rewritten

$$\tilde{k}_{\alpha S \rightarrow 0 MT}(\Lambda|\tau) = \left(\tilde{k}_{0M} * {}^1\tilde{\mathbf{P}}_{\alpha MT}^{\text{corr}} * \prod_{\gamma=1}^F \left({}^1\tilde{\mathbf{P}}_{\gamma M}^{\text{unc}} * \right)^{N_{\text{box},\gamma}} \right) (\Lambda|\tau) \quad (3.60)$$

Finally, Eq. (3.54), which combines these expressions, is rewritten

$$\tilde{k}_{\alpha S \rightarrow \beta TM}(\Lambda|\tau) = \tilde{k}_{\alpha S \rightarrow \beta MT}^{\text{corr}}(\Lambda|\tau) + \tilde{k}_{\alpha S \rightarrow \beta MT}^{\text{unc}}(\Lambda|\tau) \quad (3.61)$$

If $N_{\text{box},\beta}$ is not an integer, then the distributions are calculated with the closest integer number of molecules in the simulation box $N'_{\text{box},\beta}$, adjusting the brightness $q'_{\beta M}$ to satisfy the relation $q'_{\beta M} N'_{\text{box},\beta} = q_{\beta M} N_{\text{box},\beta}$. This keeps the total count rate from the species β constant, while using the closest integer for the number of molecules in the simulation

box. Note that the adjusted value for the brightness $q'_{\beta M}$ is used only for the expressions for the uncorrelated molecules, not the correlated molecules.

Converting Eq. (3.55) to Λ -space, we get for the cumulative intensity distribution of correlation,

$$\tilde{C}_{STM}(\Lambda|\tau) = \frac{\sum_{\alpha=0}^M \sum_{\beta=0}^M k_{\alpha S} \tilde{k}_{\alpha S \rightarrow \beta TM}(\Lambda|\tau)}{k_S k_T} \quad (3.62)$$

This is then converted to \mathbf{n} -space to get the PAID function,

$$C_{STM}(\mathbf{n}|\tau) = \int_0^\infty d\Lambda \tilde{C}_{STM}(\Lambda|\tau) \text{Poi}(\Lambda, \mathbf{n}) \quad (3.63)$$

The kernels used as the basis for the model have finite sized bins in Λ , which are indexed by b and have the range $[\Lambda_{\min}^b, \Lambda_{\max}^b)$. Because of the finite bin size, what is

really calculated is the average over a bin $\frac{\int_{\Lambda_{\min}^b}^{\Lambda_{\max}^b} d\Lambda' \tilde{C}_{STM}(\Lambda'|\tau)}{\Lambda_{\max}^b - \Lambda_{\min}^b}$. We assume that the

amplitude is constant across the bins, so that $\tilde{C}_{STM}(\Lambda|\tau) \approx \frac{\int_{\Lambda_{\min}^b}^{\Lambda_{\max}^b} d\Lambda' \tilde{C}_{STM}(\Lambda'|\tau)}{\Lambda_{\max}^b - \Lambda_{\min}^b}$ for Λ in the range $[\Lambda_{\min}^b, \Lambda_{\max}^b)$.

The expression for $C_{STM}(\mathbf{n}|\tau)$ as calculated until now gives the instantaneous rates at a particular τ . However, the time interval bins for the photon counting data have finite extent, and so $C_{STM}(\mathbf{n}|\tau)$ must be averaged over the range of the time bin. To calculate $\tilde{C}_{STM}(\Lambda|\tau)$ within the time interval τ_{\min} and τ_{\max} , we interpolate between $\tilde{C}_{STM}(\Lambda|\tau_{\min})$ and $\tilde{C}_{STM}(\Lambda|\tau_{\max})$. We project $\tilde{C}_{STM}(\Lambda|\tau_{\min})$ forward in time from τ_{\min} ,

noting that the limits of a bin in cumulative intensity scales with time interval,

$$\Lambda'_{\min}(\tau) = \Lambda_{\min}^b \frac{\tau}{\tau_{\min}} \text{ and } \Lambda'_{\max}(\tau) = \Lambda_{\max}^b \frac{\tau}{\tau_{\min}}. \text{ The value interpolated forward from } \tau_{\min}$$

$$\text{is } \tilde{C}_{STM}(\Lambda|\tau) \approx \frac{\int_{\Lambda_{\min}^b}^{\Lambda_{\max}^b} d\Lambda' \tilde{C}_{STM}(\Lambda'|\tau)}{(\Lambda_{\max}^b - \Lambda_{\min}^b) \frac{\tau}{\tau_{\min}}}, \text{ where } b \text{ is chosen so that } \Lambda_{\min}^b \leq \Lambda \frac{\tau_{\min}}{\tau} < \Lambda_{\max}^b.$$

Similarly, the value interpolated backward from τ_{\max}

$$\text{is } \tilde{C}_{STM}(\Lambda|\tau) \approx \frac{\int_{\Lambda_{\min}^b}^{\Lambda_{\max}^b} d\Lambda' \tilde{C}_{STM}(\Lambda'|\tau)}{(\Lambda_{\max}^b - \Lambda_{\min}^b) \frac{\tau}{\tau_{\max}}}, \text{ where } b \text{ is chosen so that } \Lambda_{\min}^b \leq \Lambda \frac{\tau_{\max}}{\tau} < \Lambda_{\max}^b.$$

The interpolated values are averaged over the rectangle bounded by τ_{\min} , τ_{\max} , Λ_{\min}^b , and Λ_{\max}^b . Note that more than one bin may contribute to the averaging.

The final integration over Λ shown in Eq. (3.63) is implemented as a matrix multiplication. The approximation that the value of $\tilde{C}_{STM}(\Lambda|\tau)$ is constant over a bin with limits Λ_{\min}^b , and Λ_{\max}^b leads to the approximation,

$$C_{STM}(\mathbf{n}|\tau) = \sum_b \frac{\int_{\Lambda_{\min}^b}^{\Lambda_{\max}^b} d\Lambda' \tilde{C}_{STM}(\Lambda'|\tau)}{\Lambda_{\max}^b - \Lambda_{\min}^b} \int_{\Lambda_{\min}^b}^{\Lambda_{\max}^b} d\Lambda' \text{Poi}(\Lambda', \mathbf{n}) \quad (3.64)$$

The integral on the right can be expressed in terms of the incomplete gamma

$$\text{function } \gamma(a, x) = \frac{1}{\Gamma(a)} \int_0^x e^{-t} t^{a-1} dt,$$

$$\int_{\Lambda_{\min}^b}^{\Lambda_{\max}^b} \text{Poi}(\Lambda, \mathbf{n}) d\Lambda = \gamma(\mathbf{n}+1, \Lambda_{\max}^b) - \gamma(\mathbf{n}+1, \Lambda_{\min}^b) \quad (3.65)$$

We keep the bin spacing fixed, so the integrals in Eq.(3.65) need to be performed only once to create the matrix.

3.E. Combination of sources for probability distribution

We are given two photon count probability distributions, $P_1(\mathbf{n}_1)$ and $P_2(\mathbf{n}_2)$.

Now, suppose we want to determine the photon count probability distribution for the combined source $P(\mathbf{n})$, where $\mathbf{n} = \mathbf{n}_1 + \mathbf{n}_2$. This can be determined by

$$P(\mathbf{n}) = \sum_{\mathbf{n}_1=0}^{\mathbf{n}} P_1(\mathbf{n}_1) P_2(\mathbf{n} - \mathbf{n}_1 | \mathbf{n}_1) \quad (3.66)$$

To obtain the probability to count \mathbf{n} photons from the combined source, we sum over all possible values of \mathbf{n}_1 . For each value \mathbf{n}_1 , the value of \mathbf{n}_2 is restricted so that the value of the combined total counts is correct, $\mathbf{n}_2 = \mathbf{n} - \mathbf{n}_1$. The probability to have \mathbf{n}_1 counts from source 1 is $P_1(\mathbf{n}_1)$, and the probability to have $\mathbf{n}_2 = \mathbf{n} - \mathbf{n}_1$ counts in source 2 given that there were \mathbf{n}_1 counts from source 1 is $P_2(\mathbf{n} - \mathbf{n}_1 | \mathbf{n}_1)$. We now assume that sources 1 and 2 are independent, so that $P_2(\mathbf{n} - \mathbf{n}_1 | \mathbf{n}_1) = P_2(\mathbf{n} - \mathbf{n}_1)$, and Eq. (3.66) reduces to a convolution,

$$P(\mathbf{n}) = \sum_{\mathbf{n}_1=0}^{\mathbf{n}} P_1(\mathbf{n}_1) P_2(\mathbf{n} - \mathbf{n}_1) \equiv (P_1 * P_2)(\mathbf{n}) \quad (3.67)$$

To combine more than two independent sources, one simply performs successive convolutions, $P(\mathbf{n}) = (P_1 * P_2 * P_3 * P_4 * \dots)(\mathbf{n})$.

3.F. Equivalence of convolutions in \mathbf{n} -space and Λ -space

One property that needs to be established is the equivalence of performing convolutions in \mathbf{n} space and Λ space. Consider three distributions $f(\mathbf{n}|\tau)$, $g(\mathbf{n}|\tau)$, and $h(\mathbf{n}|\tau)$, such that h is the convolution of f and g :

$$h(\mathbf{n}|\tau) = \sum_{\mathbf{n}'=0}^{\mathbf{n}} f(\mathbf{n}'|\tau) g(\mathbf{n}-\mathbf{n}'|\tau) \equiv (f * g)(\mathbf{n}|\tau) \quad (3.68)$$

We can write each of these distributions in \mathbf{n} as a Poisson transformation,

$$\begin{aligned} f(\mathbf{n}|\tau) &= \int_0^\infty \tilde{f}(\Lambda|\tau) \text{Poi}(\Lambda, \mathbf{n}) d\Lambda \\ g(\mathbf{n}|\tau) &= \int_0^\infty \tilde{g}(\Lambda|\tau) \text{Poi}(\Lambda, \mathbf{n}) d\Lambda \\ h(\mathbf{n}|\tau) &= \int_0^\infty \tilde{h}(\Lambda|\tau) \text{Poi}(\Lambda, \mathbf{n}) d\Lambda \end{aligned} \quad (3.69)$$

By substituting the Poisson transformation expressions for $f(\mathbf{n}, \tau)$ and $g(\mathbf{n}, \tau)$ into Eq. (3.68), we get

$$\begin{aligned} h(\mathbf{n}|\tau) &= \int_0^\infty d\Lambda_f \tilde{f}(\Lambda_f|\tau) \int_0^\infty d\Lambda_g \tilde{g}(\Lambda_g|\tau) \sum_{\mathbf{n}'=0}^{\mathbf{n}} \text{Poi}(\Lambda_f, \mathbf{n}') \text{Poi}(\Lambda_g, \mathbf{n}-\mathbf{n}') \\ &= \int_0^\infty d\Lambda_f \tilde{f}(\Lambda_f|\tau) \int_0^\infty d\Lambda_g \tilde{g}(\Lambda_g|\tau) \text{Poi}(\Lambda_f + \Lambda_g, \mathbf{n}) \\ &= \int_0^\infty d\Lambda \left[\int_0^\Lambda d\Lambda' \tilde{f}(\Lambda'|\tau) \tilde{g}(\Lambda - \Lambda'|\tau) \right] \text{Poi}(\Lambda, \mathbf{n}) \end{aligned} \quad (3.70)$$

Since we also know that $h(\mathbf{n}, \tau) = \int_0^\infty d\Lambda \tilde{h}(\Lambda, \tau) \text{Poi}(\Lambda, \mathbf{n})$, we find

$$\tilde{h}(\Lambda|\tau) = \int_0^\Lambda d\Lambda' \tilde{f}(\Lambda'|\tau) \tilde{g}(\Lambda - \Lambda'|\tau) = (\tilde{f} * \tilde{g})(\Lambda|\tau) \quad (3.71)$$

This shows that convolutions can equivalently be performed either in \mathbf{n} -space or Λ -space.

3.G. Combination of sources for the monitor photon count distribution of stop channel intensity

We now determine how to combine the monitor photon count distributions of stop channel intensity for multiple sources. This distribution, $k_{\alpha S \rightarrow \beta TM}(\mathbf{n}|\tau)$, is related to the PAID function considering only a single species β by a constant factor: a normalization

is applied to $k_{\alpha S \rightarrow \beta TM}(\mathbf{n}|\tau)$, similar to Eq. (3.29) ${}^1C_{STM}(\mathbf{n}|\tau) = \frac{k_{\alpha S} k_{\alpha S \rightarrow \beta TM}(\mathbf{n}|\tau)}{k_S k_T}$.

Consider two intensity paths η and ξ from independent sources 1 and 2, respectively. The intensity of each path as a function of time interval is given for each detector channel A , $\lambda_{A\eta}^1(\tau)$ and $\lambda_{A\xi}^2(\tau)$. Each source may be a single molecule, or more than one molecule. For each path, the monitor photon count distribution of the stop channel intensity is calculated by multiplying the rate in the stop channel by the probability to have received \mathbf{n} monitor photons,

$$\begin{aligned} k_{MT\eta}^1(\mathbf{n}|\tau) &= P_{M\eta}^1(\mathbf{n}|\tau) \lambda_{T\eta}^1(\tau) \\ k_{MT\xi}^2(\mathbf{n}|\tau) &= P_{M\xi}^2(\mathbf{n}|\tau) \lambda_{T\xi}^2(\tau) \end{aligned} \quad (3.72)$$

For the path η of source 1, the total intensity in the stop channel is $\lambda_{T\eta}^1(\tau)$ as a function of time interval τ . $k_{MT\eta}^1(\mathbf{n}|\tau)$ gives how much of that intensity on average is detected for a given value of monitor photon counts \mathbf{n} . $k_{MT\xi}^2(\mathbf{n}|\tau)$ is interpreted similarly.

When all possible paths are taken into account, the monitor photon count distributions of the stop channel intensity, $k_{MT}^1(\mathbf{n}|\tau)$ and $k_{MT}^2(\mathbf{n}|\tau)$, are weighted averages over all paths of $k_{MT\eta}^1(\mathbf{n}|\tau)$ and $k_{MT\xi}^2(\mathbf{n}|\tau)$, respectively,

$$\begin{aligned} k_{MT}^1(\mathbf{n}|\tau) &= \int_{S^1} \mathcal{D}(\eta) \mathcal{P}^1(\eta|\tau) k_{MT\eta}^1(\mathbf{n}|\tau) \\ k_{MT}^2(\mathbf{n}|\tau) &= \int_{S^2} \mathcal{D}(\xi) \mathcal{P}^2(\xi|\tau) k_{MT\xi}^2(\mathbf{n}|\tau) \end{aligned} \quad (3.73)$$

$\mathcal{P}^1(\eta|\tau)$ is the probability for a given intensity path η , and S^1 is the set of all intensity paths from up to a time interval τ . $\mathcal{P}^2(\xi|\tau)$ and S^2 are defined analogously. The monitor photon count probability distributions $P_M^1(\mathbf{n}|\tau)$ and $P_M^2(\mathbf{n}|\tau)$ are calculated by similar weighted averages,

$$\begin{aligned} P_M^1(\mathbf{n}|\tau) &= \int_{S^1} \mathcal{D}(\eta) \mathcal{P}^1(\eta|\tau) P_{M\eta}^1(\mathbf{n}|\tau) \\ P_M^2(\mathbf{n}|\tau) &= \int_{S^2} \mathcal{D}(\xi) \mathcal{P}^2(\xi|\tau) P_{M\xi}^2(\mathbf{n}|\tau) \end{aligned} \quad (3.74)$$

Now, say we want to determine the monitor photon count distributions of stop channel intensity for the combined source,

$$\lambda_{T\eta\xi}(\tau) = \lambda_{T\eta}^1(\tau) + \lambda_{T\xi}^2(\tau) \quad (3.75)$$

As before, the monitor photon count distribution of the stop channel intensity is calculated by multiplying the rate in the stop channel by the probability to have received \mathbf{n} monitor photons,

$$k_{MT\eta\xi}(\mathbf{n}|\tau) = P_{M\eta\xi}(\mathbf{n}|\tau) \lambda_{T\eta\xi}(\tau) \quad (3.76)$$

When all possible paths are taken into account, the monitor photon count distributions of the stop channel intensity for the combined source, $k_{MT}(\mathbf{n}|\tau)$, is

$$k_{MT}(\mathbf{n}|\tau) = \int_{S^1} \mathcal{D}(\eta) \mathcal{P}^1(\eta|\tau) \int_{S^2} \mathcal{D}(\xi) \mathcal{P}^2(\xi|\tau) k_{MT\eta\xi}(\mathbf{n}|\tau) \quad (3.77)$$

Now, since sources 1 and 2 are independent, the monitor photon count probability distribution for the combined source is the convolution of the distributions for the individual sources (see appendix 3.C),

$$P_{M\eta\xi}(\mathbf{n}|\tau) = (P_{M\eta}^1 * P_{M\xi}^2)(\mathbf{n}|\tau) \quad (3.78)$$

Using this along with Eq. (3.75), we rewrite Eq. (3.76),

$$k_{MT\eta\xi}(\mathbf{n}|\tau) = \left[\sum_{\mathbf{n}'=0}^{\mathbf{n}} P_{M\eta}^1(\mathbf{n}'|\tau) P_{M\xi}^2(\mathbf{n}-\mathbf{n}'|\tau) \right] (\lambda_{T\eta}^1(\tau) + \lambda_{T\xi}^2(\tau)) \quad (3.79)$$

By substituting this into Eq. (3.77) and grouping terms from the same source, we get

$$\begin{aligned} k_{MT}(\mathbf{n}|\tau) = & \sum_{\mathbf{n}'=0}^{\mathbf{n}} \left\{ \left[\int_{S^1} \mathcal{D}(\eta) \mathcal{P}^1(\eta|\tau) k_{MT\eta}^1(\mathbf{n}'|\tau) \right] \right. \\ & \times \left[\int_{S^2} \mathcal{D}(\xi) \mathcal{P}^2(\xi|\tau) P_{M\xi}^2(\mathbf{n}-\mathbf{n}'|\tau) \right] \\ & + \left[\int_{S^1} \mathcal{D}(\eta) \mathcal{P}^1(\eta|\tau) P_{M\eta}^1(\mathbf{n}'|\tau) \right] \\ & \left. \times \left[\int_{S^2} \mathcal{D}(\xi) \mathcal{P}^2(\xi|\tau) k_{MT\xi}^2(\mathbf{n}-\mathbf{n}'|\tau) \right] \right\} \end{aligned} \quad (3.80)$$

Now, using Eqs. (3.73) and (3.74), we get

$$k_{MT}(\mathbf{n}|\tau) = (k_{MT}^1 * P_M^2)(\mathbf{n}|\tau) + (k_{MT}^2 * P_M^1)(\mathbf{n}|\tau) \quad (3.81)$$

This equation convolves the monitor photon count distribution of stop channel intensity for each source with the photon count distribution of the other, and then adds the results. This equation along with Eq. (3.78) can be applied successively to combine many sources,

$$k_{MT}(\mathbf{n}|\tau) = \left(\sum_{\text{sources } i} k_{MT}^i * \prod_{j \neq i} P_M^j \right)(\mathbf{n}|\tau) \quad (3.82)$$

This expression is used in the text to combine the monitor photon count distributions of stop channel intensity for all of the molecules in solution.

3.H. Efficient calculation of convolutions in a quasi-logarithmic scale

Because of the large number of convolutions necessary to calculate the PAID histogram, it is necessary to have an efficient algorithm for convolutions. The standard method is to Fast Fourier Transform (FFT) the data, multiply the data in the complex transform space, and then FFT back to real space (See for example Ch. 13 of [154]). The FFT, however, requires evenly spaced bins, which can produce huge arrays if one wants a large dynamic range. We use a convolution method inspired by the multiple-tau correlation technique [152, 153] that uses the FFT for small convolutions. For each vector (**a** and **b**) to be convolved, we produce a series of linearly spaced arrays of length 64, where the resolution of each is reduced by a factor of 2 compared to its predecessor. The structure of these vectors is shown in Fig. 3.12A. In the figure, the arrays are of length 8 (rather than 64) for each factor of 2 in resolution. The array with the smallest spacing is shown at the left. In Fig. 3.12A, the first array has a spacing of $\Delta\Lambda = 0.1$. The second array has double the spacing, $\Delta\Lambda = 0.2$. The first four elements are each made up of a sum of two elements from the first array. The third array has a spacing that is doubled again, $\Delta\Lambda = 0.4$. Again, the first four elements are each made up of a sum of two elements from the second array. Continuing this structure to successively lower resolution, one obtains a series of linearly spaced arrays that can efficiently span a large dynamic range.

In Figs. 3.12B and 3.12C, we illustrate how the convolution of two series of such arrays is performed. One array is labeled with lower-case letters, and the other is labeled with upper-case letters. To calculate the convolution of two vectors, **a*****b**, the arrays

with the smallest spacing ($\Delta\Lambda = 0.1$) are convolved with each other first, as shown in Fig. 3.12B. The FFT procedure described above is used, with the arrays are zero-padded to twice the original length. We use the FFTW (Fastest Fourier Transform in the West) set of routines, developed by M. Frigo and S. G. Johnson. The lower half of the array becomes the new array for the smallest spacing. The whole array is rebinned to the next largest spacing, and serves as a contribution to the convolution with spacing $\Delta\Lambda = 0.2$.

In Fig. 3.12C, we show how the convolution for the larger spacing $\Delta\Lambda = 0.2$ is performed. Because we already performed part of the convolution with that spacing, we need to exclude that contribution in subsequent calculations. This is done by setting (or “clipping”) the lower half of

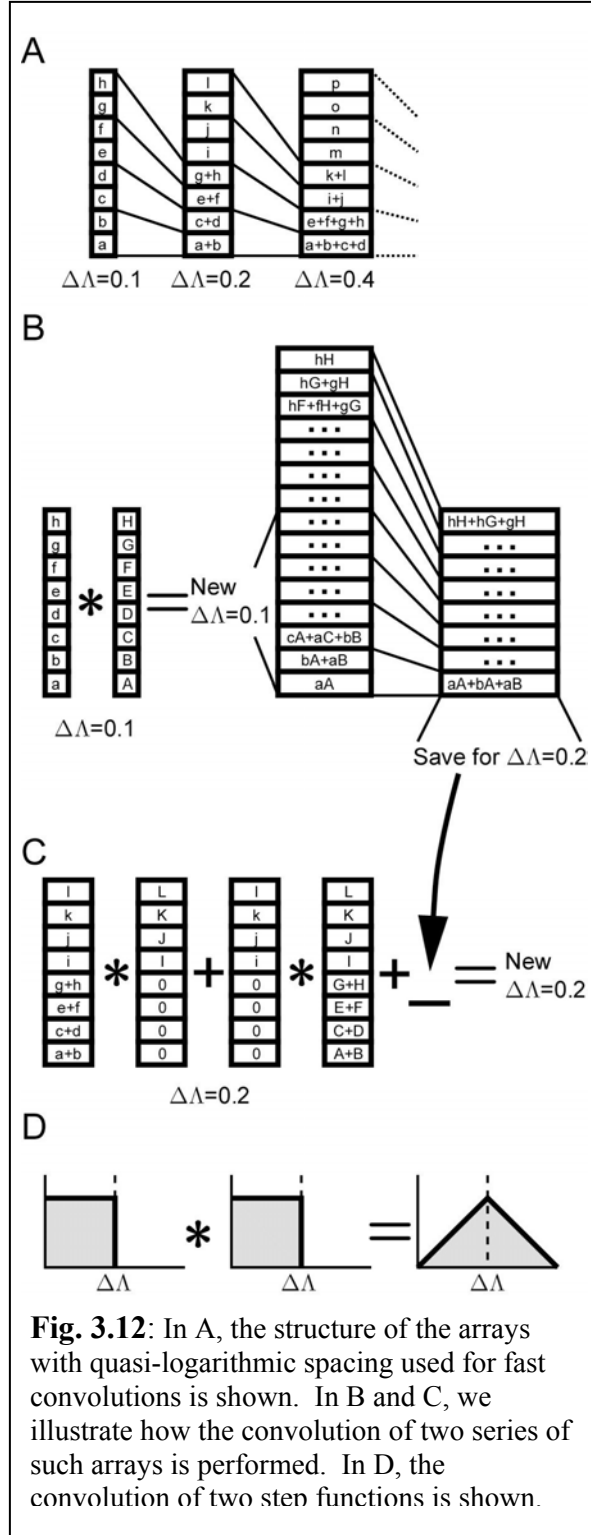


Fig. 3.12: In A, the structure of the arrays with quasi-logarithmic spacing used for fast convolutions is shown. In B and C, we illustrate how the convolution of two series of such arrays is performed. In D, the convolution of two step functions is shown.

one sub-array (*lower-case*) to 0, and convolving it with the other sub-array (*upper-case*).

The clipped version from **a** is convolved with the full version from **b**, and vice versa. By adding these results with the array obtained by rebinning the result with spacing $\Delta\Lambda = 0.1$, we obtain the final result for $\Delta\Lambda = 0.2$. This allows the use of information from higher resolution arrays to contribute to the convolutions with lower resolution arrays.

In the quasi-logarithmically spaced arrays, we approximate the function to be convolved by a series of steps; over the range of each bin, the function is assumed to be constant. When two such steps are convolved, we get a triangle, shown in Fig. 3.12D. The convolution of the two steps leaks into the next bin. The discrete convolutions shown in Figs. 3.12B and 3.12C do not account for this because they assume that the function is nonzero only at discrete values. In order to approximate the continuous functions with the method presented, the convolution is shifted one-half bin up after each FFT-based convolution in Figs. 3.12B and 3.12C.

In Eqs (3.58)-(3.60), there are successive convolutions performed on the same array which have the form $\left({}^1\tilde{\mathbf{P}}_{\gamma M}^{\text{unc}}\right)^{N_{\text{box},\gamma}}$. In order to compute $N_{\text{box},\gamma}$ successive convolutions on the original distribution ${}^1\tilde{\mathbf{P}}_{\gamma M}^{\text{unc}}$, we can use a trick to prevent performing $N_{\text{box},\gamma}$ convolutions directly. We express the number $N_{\text{box},\gamma}$ in binary. By recursively convolving the original array, we obtain a series of vectors for each convolved power of 2: 1,2,4,8,... By convolving only those convolved powers of 2 in the binary representation of $N_{\text{box},\gamma}$, we obtain $\left({}^1\tilde{\mathbf{P}}_{\gamma M}^{\text{unc}}\right)^{N_{\text{box},\gamma}}$. This allows the number of convolutions performed to increase logarithmically with $N_{\text{box},\gamma}$.

References

1. Tamarat, P., et al., *Ten years of single-molecule spectroscopy*. Journal of Physical Chemistry A, 2000. **104**(1): p. 1-16.
2. Weiss, S., *Fluorescence spectroscopy of single biomolecules*. Science, 1999. **283**(5408): p. 1676-83.
3. Moerner, W.E. and M. Orrit, *Illuminating single molecules in condensed matter*. Science, 1999. **283**(5408): p. 1670-6.
4. Ambrose, W.P., et al., *Single molecule fluorescence spectroscopy at ambient temperature*. Chem Rev, 1999. **99**(10): p. 2929-56.
5. Xie, X.S. and J.K. Trautman, *Optical studies of single molecules at room temperature*. Annual Review of Physical Chemistry, 1998. **49**: p. 441-480.
6. Basche, T., et al., *Single-molecule optical detection, imaging and spectroscopy*. 1997.
7. Nie, S. and R.N. Zare, *Optical detection of single molecules*. Annual Review of Biophysics and Biomolecular Structure, 1997. **26**(4): p. 567-96.
8. Frauenfelder, H., S.G. Sligar, and P.G. Wolynes, *The energy landscapes and motions of proteins*. Science, 1991. **254**(5038): p. 1598-603.
9. Rader, S.D. and D.A. Agard, *Conformational substates in enzyme mechanism: the 120 K structure of alpha-lytic protease at 1.5 Å resolution*. Protein Sci, 1997. **6**(7): p. 1375-86.
10. Lu, H. and P.J. Booth, *The final stages of folding of the membrane protein bacteriorhodopsin occur by kinetically indistinguishable parallel folding paths that are mediated by pH*. J Mol Biol, 2000. **299**(1): p. 233-43.
11. Leeson, D.T., et al., *Protein folding and unfolding on a complex energy landscape*. Proc Natl Acad Sci U S A, 2000. **97**(6): p. 2527-32.
12. Goldbeck, R.A., et al., *Multiple pathways on a protein-folding energy landscape: kinetic evidence*. Proc Natl Acad Sci U S A, 1999. **96**(6): p. 2782-7.
13. Moran, L.B., et al., *Transition state heterogeneity in GCN4 coiled coil folding studied by using multisite mutations and crosslinking*. Proc Natl Acad Sci U S A, 1999. **96**(19): p. 10699-704.
14. Shastry, M.C. and J.B. Udgaonkar, *The folding mechanism of barstar: evidence for multiple pathways and multiple intermediates*. J Mol Biol, 1995. **247**(5): p. 1013-27.
15. Deller, M.C., et al., *Crystal structure and functional dissection of the cytostatic cytokine oncostatin M*. Structure Fold Des, 2000. **8**(8): p. 863-74.
16. Pawson, T. and P. Nash, *Protein-protein interactions define specificity in signal transduction*. Genes Dev, 2000. **14**(9): p. 1027-47.
17. Cohen, F.E. and S.B. Prusiner, *Pathologic conformations of prion proteins*. Annual Review of Biochemistry, 1998. **67**(1): p. 793-819.
18. Cohen, F.E., *Protein misfolding and prion diseases*. Journal of Molecular Biology, 1999. **293**(2): p. 313-20.
19. Bieschke, J., et al., *Ultrasensitive detection of pathological prion protein aggregates by dual-color scanning for intensely fluorescent targets*. Proceedings

- of the National Academy of Sciences of the United States of America, 2000. **97**(10): p. 5468-73.
20. Tjernberg, L.O., et al., *Amyloid beta-peptide polymerization studied using fluorescence correlation spectroscopy*. Chem Biol, 1999. **6**(1): p. 53-62.
 21. Eigen, M. and R. Rigler, *Sorting Single Molecules - Application to Diagnostics and Evolutionary Biotechnology*. Proceedings of the National Academy of Sciences of the United States of America, 1994. **91**(13): p. 5740-5747.
 22. Rigler, R., *Fluorescence correlations, single molecule detection and large number screening. Applications in biotechnology*. J Biotechnol, 1995. **41**(2-3): p. 177-86.
 23. Fernandes, P.B., *Technological advances in high-throughput screening*. Curr Opin Chem Biol, 1998. **2**(5): p. 597-603.
 24. Weiss, S., *Measuring conformational dynamics of biomolecules by single molecule fluorescence spectroscopy*. Nat Struct Biol, 2000. **7**(9): p. 724-9.
 25. Bai, C., et al., *Single molecule physics and chemistry*. Proc Natl Acad Sci U S A, 1999. **96**(20): p. 11075-6.
 26. Fisher, T.E., P.E. Marszalek, and J.M. Fernandez, *Stretching single molecules into novel conformations using the atomic force microscope*. Nat Struct Biol, 2000. **7**(9): p. 719-24.
 27. Maiti, S., U. Haupts, and W.W. Webb, *Fluorescence correlation spectroscopy: diagnostics for sparse molecules*. Proceedings of the National Academy of Sciences of the United States of America, 1997. **94**(22): p. 11753-7.
 28. Widengren, J. and R. Rigler, *Fluorescence correlation spectroscopy as a tool to investigate chemical reactions in solutions and on cell surfaces*. Cell Mol Biol (Noisy-le-grand), 1998. **44**(5): p. 857-79.
 29. Kettling, U., et al., *Real-time enzyme kinetics monitored by dual-color fluorescence cross-correlation spectroscopy*. Proceedings of the National Academy of Sciences of the United States of America, 1998. **V95**(N4): p. 1416-1420.
 30. Schwille, P., F.J. Meyer-Almes, and R. Rigler, *Dual-color fluorescence cross-correlation spectroscopy for multicomponent diffusional analysis in solution [see comments]*. Biophysical Journal, 1997. **72**(4): p. 1878-86.
 31. Rippe, K., *Simultaneous binding of two DNA duplexes to the NtrC-enhancer complex studied by two-color fluorescence cross-correlation spectroscopy*. Biochemistry, 2000. **V39**(N9): p. 2131-2139.
 32. Zander, C., et al., *Single-molecule counting and identification in a microcapillary*. Chemical Physics Letters, 1998. **286**(5-6): p. 457-65.
 33. Deniz, A.A., et al., *Single-pair fluorescence resonance energy transfer on freely diffusing molecules: observation of Förster distance dependence and subpopulations*. Proceedings of the National Academy of Sciences of the United States of America, 1999. **96**(7): p. 3670-5.
 34. Fries, J.R., et al., *Quantitative identification of different single molecules by selective time-resolved confocal fluorescence spectroscopy*. Journal of Physical Chemistry a, 1998. **102**(33): p. 6601-6613.
 35. Oster, G. and H. Wang, *ATP synthase: two motors, two fuels*. Structure, 1999. **7**(4): p. R67-72.

36. Dill, K.A. and D. Shortle, *Denatured states of proteins*. Annu Rev Biochem, 1991. **60**: p. 795-825.
37. Smith, L.J., et al., *The concept of a random coil. Residual structure in peptides and denatured proteins*. Fold Des, 1996. **1**(5): p. R95-106.
38. Smith, M.M., *Histone structure and function*. Curr Opin Cell Biol, 1991. **3**(3): p. 429-37.
39. Dale, R.E., J. Eisinger, and W.E. Blumberg, *The orientational freedom of molecular probes. The orientation factor in intramolecular energy transfer*. Biophysical Journal, 1979. **26**(2): p. 161-93.
40. Lakowicz, J.R., *Principles of fluorescence spectroscopy*. 2nd ed. 1999, New York: Kluwer Academic/Plenum. xxiii, 698.
41. Stryer, L. and R.P. Haugland, *Energy transfer: a spectroscopic ruler*. Proc Natl Acad Sci U S A, 1967. **58**(2): p. 719-26.
42. Selvin, P.R., *The renaissance of fluorescence resonance energy transfer*. Nat Struct Biol, 2000. **7**(9): p. 730-4.
43. Ha, T., et al., *Probing the interaction between two single molecules: fluorescence resonance energy transfer between a single donor and a single acceptor*. Proc Natl Acad Sci U S A, 1996. **93**(13): p. 6264-8.
44. Ha, T., et al., *Ligand-induced conformational changes observed in single RNA molecules*. Proceedings of the National Academy of Sciences of the United States of America, 1999. **96**(16): p. 9077-82.
45. Zhuang, X.W., et al., *A single-molecule study of RNA catalysis and folding*. Science, 2000. **288**(5473): p. 2048-2051,2045.
46. Deniz, A.A., et al., *Single-molecule protein folding: diffusion fluorescence resonance energy transfer studies of the denaturation of chymotrypsin inhibitor 2*. Proceedings of the National Academy of Sciences of the United States of America, 2000. **97**(10): p. 5179-84.
47. Jia, Y., et al., *Folding dynamics of single GCN4 peptides by fluorescence resonant energy transfer confocal microscopy*. Chemical Physics, 1999. **247**(1): p. 69-83.
48. Ishii, Y., et al., *Fluorescence resonance energy transfer between single fluorophores attached to a coiled-coil protein in aqueous solution*. Chemical Physics, 1999. **247**(1): p. 163-73.
49. Ha, T., et al., *Single-molecule fluorescence spectroscopy of enzyme conformational dynamics and cleavage mechanism*. Proceedings of the National Academy of Sciences of the United States of America, 1999. **96**(3): p. 893-8.
50. Brasselet, S. and W.E. Moerner, *Fluorescence behavior of single-molecule pH-sensors*. Single Molecules, 2000. **1**(1): p. 17-23.
51. Schutz, G.J., W. Trabsinger, and T. Schmidt, *Direct observation of ligand colocalization on individual receptor molecules*. Biophys J, 1998. **74**(5): p. 2223-6.
52. Sako, Y., S. Minoghchi, and T. Yanagida, *Single-molecule imaging of EGFR signalling on the surface of living cells [see comments]*. Nature Cell Biology, 2000. **2**(3): p. 168-72.

53. Koshioka, M., K. Sasaki, and H. Masuhara, *Time-dependent fluorescence depolarization analysis in three-dimensional microspectroscopy*. Applied Spectroscopy, 1995. **49**(2): p. 224-8.
54. Ha, T., et al., *Polarization spectroscopy of single fluorescent molecules*. Journal of Physical Chemistry B, 1999. **103**(33): p. 6839-6850.
55. Warshaw, D.M., et al., *Myosin conformational states determined by single fluorophore polarization*. Proc Natl Acad Sci U S A, 1998. **95**(14): p. 8034-9.
56. Kinoshita, K., Jr., *Real time imaging of rotating molecular machines*. Faseb J, 1999. **13 Suppl 2**: p. S201-8.
57. Adachi, K., et al., *Stepping rotation of F1-ATPase visualized through angle-resolved single-fluorophore imaging*. Proc Natl Acad Sci U S A, 2000. **97**(13): p. 7243-7.
58. Dahan, M., et al., *Ratiometric measurement and identification of single diffusing molecules*. Chemical Physics, 1999. **247**(1): p. 85-106.
59. Reynaud, S., *Resonance fluorescence: the dressed atom approach*. Annales de Physique, 1983. **8**(4): p. 315-70.
60. VanOrden, A., et al., *Single molecule identification in flowing sample streams by fluorescence burst size and intraburst fluorescence decay rate*. Analytical Chemistry, 1998. **V70**(N7): p. 1444-1451.
61. Widengren, J. and P. Schwille, *Characterization of photoinduced isomerization and back-isomerization of the cyanine dye Cy5 by fluorescence correlation spectroscopy*. Journal of Physical Chemistry a, 2000. **104**(27): p. 6416-6428.
62. Ying, L.M., et al., *Ratiometric analysis of single-molecule fluorescence resonance energy transfer using logical combinations of threshold criteria: A study of 12-mer DNA*. Journal of Physical Chemistry B, 2000. **104**(21): p. 5171-5178.
63. Deniz, A.A., et al., *Ratiometric single-molecule studies of freely diffusing biomolecules*. Annual Review of Physical Chemistry, 2001. **V52**: p. 233-253.
64. Haas, E., et al., *Distribution of end-to-end distances of oligopeptides in solution as estimated by energy transfer*. Proceedings of the National Academy of Sciences of the United States of America, 1975. **72**(5): p. 1807-11.
65. Haas, E. and I.Z. Steinberg, *Intramolecular dynamics of chain molecules monitored by fluctuations in efficiency of excitation energy transfer. A theoretical study*. Biophysical Journal, 1984. **46**(4): p. 429-37.
66. Magde, D., E. Elson, and W.W. Webb, *Thermodynamic fluctuations in a reacting system: measurement by fluorescence correlation spectroscopy*. Physical Review Letters, 1972. **29**(11): p. 705-8.
67. Lu, H.P., L. Xun, and X.S. Xie, *Single-molecule enzymatic dynamics*. Science, 1998. **282**(5395): p. 1877-82.
68. Xie, X.S. and H.P. Lu, *Single-molecule enzymology*. J Biol Chem, 1999. **274**(23): p. 15967-70.
69. Edman, L., et al., *The fluctuating enzyme: a single molecule approach*. Chemical Physics, 1999. **247**(1): p. 11-22.
70. Edman, L. and R. Rigler, *Memory landscapes of single-enzyme molecules*. Proc Natl Acad Sci U S A, 2000. **97**(15): p. 8266-71.

71. Lamb, D.C., et al., *Sensitivity enhancement in fluorescence correlation spectroscopy of multiple species using time-gated detection*. Biophysical Journal, 2000. **79**(2): p. 1129-1138.
72. Brooks, C.L., 3rd, *Simulations of protein folding and unfolding*. Curr Opin Struct Biol, 1998. **8**(2): p. 222-6.
73. Alm, E. and D. Baker, *Matching theory and experiment in protein folding*. Current Opinion in Structural Biology, 1999. **9**(2): p. 189-96.
74. Muñoz, V. and W.A. Eaton, *A simple model for calculating the kinetics of protein folding from three-dimensional structures*. Proceedings of the National Academy of Sciences of the United States of America, 1999. **96**(20): p. 11311-6.
75. Galzitskaya, O.V. and A.V. Finkelstein, *A theoretical search for folding/unfolding nuclei in three-dimensional protein structures*. Proceedings of the National Academy of Sciences of the United States of America, 1999. **96**(20): p. 11299-304.
76. Alm, E. and D. Baker, *Prediction of protein-folding mechanisms from free-energy landscapes derived from native structures*. Proceedings of the National Academy of Sciences of the United States of America, 1999. **96**(20): p. 11305-10.
77. Onuchic, J.N., Z. Luthey-Schulten, and P.G. Wolynes, *Theory of protein folding: the energy landscape perspective*. Annual Review of Physical Chemistry, 1997. **48**(2): p. 545-600.
78. Beligere, G.S. and P.E. Dawson, *Conformationally assisted protein ligation using C-terminal thioester peptides*. Journal of the American Chemical Society, 1999. **121**(26): p. 6332-6333.
79. Merrifield, R.B., J. Am. Chem. Soc., 1963. **85**: p. 2149-2154.
80. Schnolzer, M., et al., *In situ neutralization in Boc-chemistry solid phase peptide synthesis. Rapid, high yield assembly of difficult sequences*. Int J Pept Protein Res, 1992. **40**(3-4): p. 180-93.
81. Hackeng, T.M., J.H. Griffin, and P.E. Dawson, *Protein synthesis by native chemical ligation: expanded scope by using straightforward methodology*. Proc Natl Acad Sci U S A, 1999. **96**(18): p. 10068-73.
82. Itzhaki, L.S., D.E. Otzen, and A.R. Fersht, *The structure of the transition state for folding of chymotrypsin inhibitor 2 analysed by protein engineering methods: evidence for a nucleation-condensation mechanism for protein folding*. Journal of Molecular Biology, 1995. **254**(2): p. 260-88.
83. Oliveberg, M., et al., *The changing nature of the protein folding transition state: implications for the shape of the free-energy profile for folding*. J Mol Biol, 1998. **277**(4): p. 933-43.
84. Lazaridis, T. and M. Karplus, *"New view" of protein folding reconciled with the old through multiple unfolding simulations*. Science, 1997. **278**(5345): p. 1928-31.
85. Ladurner, A.G., et al., *Synergy between simulation and experiment in describing the energy landscape of protein folding*. Proceedings of the National Academy of Sciences of the United States of America, 1998. **95**(15): p. 8473-8.
86. Jackson, S.E. and A.R. Fersht, *Folding of chymotrypsin inhibitor 2. 1. Evidence for a two-state transition*. Biochemistry, 1991. **30**(43): p. 10428-35.

87. Dawson, P.E., et al., *Synthesis of proteins by native chemical ligation*. Science, 1994. **266**(5186): p. 776-9.
88. McPhalen, C.A. and M.N. James, *Crystal and molecular structure of the serine proteinase inhibitor CI-2 from barley seeds*. Biochemistry, 1987. **26**(1): p. 261-9.
89. Englert, A. and M. Leclerc, *Intramolecular energy transfer in molecules with a large number of conformations*. Proceedings of the National Academy of Sciences USA, 1978. **75**(3): p. 1050-1051.
90. Miller, W.G. and C.V. Goebel, *Dimensions of protein random coils*. Biochemistry, 1968. **7**(11): p. 3925-35.
91. Alonso, D.O. and K.A. Dill, *Solvent denaturation and stabilization of globular proteins*. Biochemistry, 1991. **30**(24): p. 5974-85.
92. Pollack, L., et al., *Compactness of the denatured state of a fast-folding protein measured by submillisecond small-angle x-ray scattering*. Proceedings of the National Academy of Sciences of the United States of America, 1999. **96**(18): p. 10115-7.
93. Plaxco, K.W., et al., *Chain collapse can occur concomitantly with the rate-limiting step in protein folding*. Nat Struct Biol, 1999. **6**(6): p. 554-6.
94. Nozaki, Y., *The preparation of guanidine hydrochloride*. Methods Enzymol, 1972. **26 PtC**: p. 43-50.
95. Jackson, S.E. and A.R. Fersht, *Folding of chymotrypsin inhibitor 2. 2. Influence of proline isomerization on the folding kinetics and thermodynamic characterization of the transition state of folding*. Biochemistry, 1991. **30**(43): p. 10436-43.
96. Schaffer, J., et al., *Identification of single molecules in aqueous solution by time-resolved fluorescence anisotropy*. Journal of Physical Chemistry a, 1999. **103**(3): p. 331-336.
97. Forster, S., and M. Schmidt, *Polyelectrolytes in Solution*, in *Advances in Polymer Science 120*. 1995, Springer. p. 51-133.
98. Barrat, J.-L., and Jean-Francois Joanny, *Theory of Polyelectrolyte Solutions*, in *Advances in Chemical Physics*, I.P.a.S.A. Rice, Editor. 1996, John Wiley & Sons. p. 1-65.
99. Yevich, R. and W.K. Olson, *The Spatial Distributions of Randomly Coiling Polynucleotides*. Biopolymers, 1979. **18**: p. 113-145.
100. Mills, J.B., E. Vacano, and P.J. Hagerman, *Flexibility of single-stranded DNA: use of gapped duplex helices to determine the persistence lengths of poly(dT) and poly(dA)*. J Mol Biol, 1999. **285**(1): p. 245-57.
101. Smith, S.B., Y. Cui, and C. Bustamante, *Overstretching B-DNA: the elastic response of individual double-stranded and single-stranded DNA molecules*. Science, 1996. **271**(5250): p. 795-9.
102. Wuite, G.J., et al., *Single-molecule studies of the effect of template tension on T7 DNA polymerase activity*. Nature, 2000. **404**(6773): p. 103-6.
103. Doi, M. and S.F. Edwards, *The theory of polymer dynamics*. 1988, Oxford Oxfordshire, New York: Clarendon Press, Oxford University Press. xiii, 391.
104. Walhout, A.J.M. and M. Vidal, *Protein interaction maps for model organisms*. Nature Reviews Molecular Cell Biology, 2001. **V2**(N1): p. 55-62.
105. Mendelsohn, A.R. and R. Brent, *Protein biochemistry - Protein interaction methods - Toward an endgame*. Science, 1999. **V284**(N5422): p. 1948-1950.

106. Yanagida, M., *Functional proteomics; current achievements*. J Chromatogr B Analyt Technol Biomed Life Sci, 2002. **771**(1-2): p. 89-106.
107. Chalmers, M.J. and S.J. Gaskell, *Advances in mass spectrometry for proteome analysis*. Current Opinion in Biotechnology, 2000. **V11**(N4): p. 384-390.
108. De Angelis, D.A., *Why FRET over genomics?* Physiological Genomics, 1999. **V1**(N2): p. 93-99.
109. Rigler, R. and E. Elson, *Fluorescence correlation spectroscopy : theory and applications*. 2001, Berlin ; New York: Springer. xx, 487.
110. Schwille, P., *Fluorescence Correlation Spectroscopy and Its Potential for Intracellular Applications*. Cell Biochemistry and Biophysics, 2001. **34**: p. 383-408.
111. Rarbach, M., et al., *Dual-color fluorescence cross-correlation spectroscopy for monitoring the kinetics of enzyme-catalyzed reactions*. Methods, 2001. **V24**(N2): p. 104-116.
112. Keller, R.A., et al., *Single Molecule Fluorescence Analysis in Solution*. Applied Spectroscopy, 1996. **V50**(N7): p. A12-A32.
113. Elson, E.L. and D. Magde, *Fluorescence correlation spectroscopy. I. Conceptual Basis and Theory*. Biopolymers, 1974. **13**(1): p. 1-27.
114. Ehrenberg, M. and R. Rigler, *Rotational Brownian motion and fluorescence intensity fluctuations*. Chemical Physics, 1974. **4**(3): p. 390-401.
115. Widengren, J., U. Mets, and R. Rigler, *Fluorescence Correlation Spectroscopy of Triplet States in Solution - a Theoretical and Experimental Study*. Journal of Physical Chemistry, 1995. **99**(36): p. 13368-13379.
116. Widengren, J. and R. Rigler, *Mechanisms of photobleaching investigated by fluorescence correlation spectroscopy*. Bioimaging, 1996. **4**(3): p. 149-57.
117. Magde, D., E.L. Elson, and W.W. Webb, *Fluorescence correlation spectroscopy. II. An experimental realization*. Biopolymers, 1974. **13**(1): p. 29-61.
118. Qian, H. and E.L. Elson, *On the analysis of high order moments of fluorescence fluctuations*. Biophysical Journal, 1990. **57**(2): p. 375-80.
119. Qian, H. and E.L. Elson, *Distribution of molecular aggregation by analysis of fluctuation moments*. Proceedings of the National Academy of Sciences of the United States of America, 1990. **87**(14): p. 5479-83.
120. Palmer, A.G., III and N.L. Thompson, *Optical spatial intensity profiles for high order autocorrelation in fluorescence spectroscopy*. Applied Optics, 1989. **28**(6): p. 1214-20.
121. Chen, Y., et al., *The photon counting histogram in fluorescence fluctuation spectroscopy*. Biophysical Journal, 1999. **77**(1): p. 553-67.
122. Kask, P., et al., *Fluorescence-intensity distribution analysis and its application in biomolecular detection technology*. Proceedings of the National Academy of Sciences of the United States of America, 1999. **96**(24): p. 13756-61.
123. Muller, J.D., Y. Chen, and E. Gratton, *Resolving heterogeneity on the single molecular level with the photon-counting histogram*. Biophysical Journal, 2000. **V78**(N1 PT1): p. 474-486.
124. Chen, Y., et al., *Probing ligand protein binding equilibria with fluorescence fluctuation spectroscopy*. Biophysical Journal, 2000. **79**(2): p. 1074-1084.

125. Margeat, E., et al., *The human estrogen receptor alpha dimer binds a single SRC-1 coactivator molecule with an affinity dictated by agonist structure*. J Mol Biol, 2001. **306**(3): p. 433-42.
126. Van Rompaey, E., et al., *Fluorescence fluctuation analysis for the study of interactions between oligonucleotides and polycationic polymers*. Biol Chem, 2001. **382**(3): p. 379-86.
127. Scheel, A.A., et al., *Receptor-ligand interactions studied with homogeneous fluorescence-based assays suitable for miniaturized screening*. Journal of Biomolecular Screening, 2001. **V6**(N1): p. 11-18.
128. Rudiger, M., et al., *Single-molecule detection technologies in miniaturized high throughput screening: Binding assays for G protein-coupled receptors using fluorescence intensity distribution analysis and fluorescence anisotropy*. Journal of Biomolecular Screening, 2001. **V6**(N1): p. 29-37.
129. Chen, Y., et al., *Molecular brightness characterization of EGFP in vivo by fluorescence fluctuation spectroscopy*. Biophysical Journal, 2002. **V82**(N1): p. 133-144.
130. Palo, K., et al., *Fluorescence intensity multiple distributions analysis: concurrent determination of diffusion times and molecular brightness*. Biophysical Journal, 2000. **79**(6): p. 2858-66.
131. Heinze, K.G., A. Koltermann, and P. Schwille, *Simultaneous two-photon excitation of distinct labels for dual-color fluorescence crosscorrelation analysis*. Proceedings of the National Academy of Sciences of the United States of America, 2000. **97**(19): p. 10377-82.
132. Schwille, P. and K.G. Heinze, *Two-photon fluorescence cross-correlation spectroscopy*. Chemphyschem, 2001. **V2**(N5): p. 269-272.
133. Tellinghuisen, J., et al., *Analysis of Fluorescence Lifetime Data for Single Rhodamine Molecules in Flowing Sample Streams*. Analytical Chemistry, 1994. **V66**(N1): p. 64-72.
134. Eggeling, C., et al., *Monitoring conformational dynamics of a single molecule by selective fluorescence spectroscopy*. Proceedings of the National Academy of Sciences of the United States of America, 1998. **95**(4): p. 1556-61.
135. Kask, P., et al., *Two-dimensional fluorescence intensity distribution analysis: theory and applications*. Biophysical Journal, 2000. **78**(4): p. 1703-13.
136. Mets, U., *Antibunching and Rotational Diffusion in FCS*, in *Fluorescence Correlation Spectroscopy*, R. Rigler, and E.S. Elson, Editor. 2001, Springer. p. 346-359.
137. Widengren, J., *Photophysical Aspects of FCS Measurements*, in *Fluorescence Correlation Spectroscopy*, R. Rigler, and E.S. Elson, Editor. 2001, Springer. p. 276-301.
138. Hebert, T.E. and M. Bouvier, *Structural and functional aspects of G protein-coupled receptor oligomerization*. Biochem Cell Biol, 1998. **76**(1): p. 1-11.
139. Milligan, G., *Neurobiology. Receptors as kissing cousins*. Science, 2000. **288**(5463): p. 65-7.
140. Prusiner, S.B., *Prions*. Proceedings of the National Academy of Sciences of the United States of America, 1998. **95**(23): p. 13363-83.

141. Enderlein, J., David L. Robbins, W. Patrick Ambrose, Peter M. Goodwin, and Richard A. Keller, *Statistics of Single-Molecule Detection*. Journal of Physical Chemistry B, 1997. **101**: p. 3626-3632.
142. Wohland, T., R. Rigler, and H. Vogel, *The standard deviation in fluorescence correlation spectroscopy*. Biophysical Journal, 2001. **80**(6): p. 2987-99.
143. Richards, B. and E. Wolf, *Electromagnetic diffraction in optical systems. II. Structure of the image field in an aplanatic system*. Proceedings of the Royal Physical Society A (London), 1959. **253**: p. 358-379.
144. Wolf, E., *Electromagnetic diffraction in optical systems. I. An integral representation of the image field*. Proceedings of the Royal Physical Society A (London), 1959. **253**: p. 349-357.
145. Rigler, R., et al., *Fluorescence Correlation Spectroscopy With High Count Rate and Low Background - Analysis of Translational Diffusion*. European Biophysics Journal, 1993. **22**(3): p. 169-175.
146. Kubo, R.o., M. Toda, and N. Hashitsume, *Statistical physics II : nonequilibrium statistical mechanics*. 2nd ed. Springer series in solid-state sciences ; 31. 1991, Berlin ; New York: Springer. 279.
147. Marquardt, D.W., *An algorithm for least-squares estimation of nonlinear parameters*. J. Soc. Indust. Appl. Math., 1963. **11**(2): p. 431-441.
148. Sambrook, J. and D.W. Russell, *Molecular cloning : a laboratory manual*. 3rd ed. 2001, Cold Spring Harbor, N.Y.: Cold Spring Harbor Laboratory Press. 3 v.
149. Ross, S.M., *Introduction to Probability and Statistics for Engineers and Scientists*. 1987, New York: John Wiley & Sons. xv,492.
150. Lide, D.R., *CRC handbook of chemistry and physics*. 3rd electronic ed ed. 2001, Boca Raton, FL: CRC Press.
151. Efron, B. and R. Tibshirani, *An introduction to the bootstrap*. Monographs on statistics and applied probability ; 57. 1993, New York: Chapman & Hall. xvi, 436.
152. Schatzel, K., *New concepts in correlator design*. Inst. Phys. Conf. Ser. No. 77: session 4, 1985. **No. 77: session 4**: p. 175-185.
153. Schatzel, K. and R. Peters, *Noise on Multiple-Tau Photon Correlation Data*. SPIE vol. 1430 Photon Correlation Spectroscopy: Multicomponent Systems, 1991. **1430**: p. 109-115.
154. Press, W.H., S. A. Teukolsky, W. T. Vetterling, and B. P. Flannery, *Numerical recipes in C : the art of scientific computing*. 2nd ed. 1992, Cambridge, U.K.: Cambridge University Press. xxvi, 994.
155. Enderlein, J., *Path Integral Approach to Fluorescence Correlation Experiments*. Physics Letters A, 1996. **V221(N6)**: p. 427-433.
156. Gardiner, C.W., *Handbook of stochastic methods for physics, chemistry, and the natural sciences*. 2nd ed. 1985, Berlin ; New York: Springer-Verlag. xix, 442.
157. Mandel, L., *Fluctuations of Photon Beams and their Correlation*. Proc. Phys. Soc., 1958. **72**: p. 1037-1048.
158. Mandel, L., *Fluctuations of Photon Beams: The Distribution of the Photo-Electrons*. Proc. Phys. Soc., 1959. **74**(3): p. 233-243.